UNIVERSITAT DE BARCELONA

# Advancing cancer precision medicine through cell-based functional assays and microfluidics

## Finding the needle in a haystack to improve pediatric leukemia treatment

Albert Manzano Muñoz

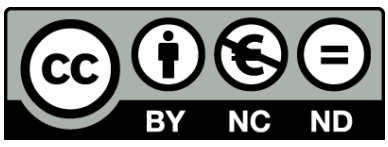

Tesi doctoral

# Advancing cancer precision medicine through cell-based functional assays and microfluidics

## Finding the needle in a haystack to improve pediatric leukemia treatment

Albert Manzano Muñoz

Dirigit per Joan Montero Boronat


UNIVERSITAT DE BARCELONA

# Advancing cancer precision medicine through cell-based functional assays and microfluidics

Finding the needle in a haystack to improve pediatric leukemia treatment

Programa de doctorat en Biomedicina

Universitat de Barcelona

Tesis realitzada a l'Institut de Bioenginyeria de Catalunya (IBEC)


| Autor | Director | Tutor |
| --- | --- | --- |
| **Albert Manzano Muñoz** | **Joan Montero Boronat** | **Josep Samitier Martí** |


UNIVERSITAT DE BARCELONA

## Summary

Personalized medicine has emerged to improve cancer treatment beyond classical approaches. The identification of genetic mutations by molecular analyses dominate personalized medicine initiatives promoting clinical benefit, but they often present limited predictive capacity for treatments. An alternative to these are functional assays, which expose cancer cells to different therapeutic options to identify which will be the most effectives in eliminating the tumor. Although these techniques are less widespread than those based on genetic studies, the first clinical trials using functional assays obtained good results. Even so, there are important limitations to the application of these techniques, including the obtention of sufficient biological material to perform these assays or the deterioration of the primary samples under *ex vivo* conditions. Dynamic BH3 Profiling (DBP) is a functional assay that allows a rapid prediction of treatment efficacy, thus avoiding sample decline. In this thesis, we focus on finding new effective treatments for pediatric B-cell Precursor Acute Lymphoblastic Leukemia (BCP-ALL), especially in the small percentage of patients who relapse after being treated with standard-of-care therapy. Using DBP in *in vitro* models, we identified cytotoxic chemotherapeutics and targeted therapies after short incubations. In addition, we also detected adaptations conferring resistance to the applied drug mediated by antiapoptotic proteins of the BCL-2 family. These observations pointed to the potential use of BH3 mimetics, specific inhibitors of antiapoptotic proteins already utilized in the clinic, in combination with other anticancer treatments. In our BCP-ALL models we identified antiapoptotic adaptations after treatment using DBP, which helped us to rationally design new combinations of chemotherapeutics or targeted therapies with a specific BH3 mimetic to block the observed adaptation. These new combinations boosted treatment efficacy or allowed a reduction of its concentration while maintaining cytotoxicity. DBP also predicted the efficacy of anticancer treatments and treatment-related antiapoptotic adaptations in pediatric BCP-ALL PDX models. Finally, we performed this functional assay directly on different pediatric patient samples presenting limited therapeutic options. Following clinicians' suggestions, we tested several compassionate drug use candidates. Some of the treatments identified by DBP were added to the patients' treatment, achieving complete remission in some cases.

Another limitation of DBP is the number of cells required to perform the assay, especially in solid tumors, where biopsies provide a limited number of viable cells are usually obtained. Microfluidic platforms allow to perform typical laboratory assays by automatizing and miniaturizing the process, thus reducing cell requirement. Therefore,

we developed a microfluidic chip that automatically generates a BIM peptide gradient needed to perform the DBP assay on a small number of treated cancer cells in different microwells. In addition, we also adapted the detection method to be performed *in situ* in the same chip by fluorescence microscopy. To validate our microfluidic prototype, we used gastrointestinal stromal tumor (GIST) models to compare the results obtained in this microfluidic platform with the standard FACS-based DBP assay, achieving similar results. Finally, we performed these assays with a GIST patient sample, where we could identify a cytotoxic treatment combination, predicted by both the FACS-based DBP and the new microfluidic version, the latter with a 10-fold reduction in the required number cells.

# Table of contents

# Summary of figures

# Summary of tables

## Abbreviations

ALL – Acute lymphoblastic leukemia

AML – Acute myeloid leukemia

BCP-ALL – B-cell precursor acute lymphoblastic leukemia

BH – BCL-2 homology

CI – Combination index

CLL – Chronic lymphoblastic leukemia

CML – Chronic myeloid leukemia

CNS – Central nervous system

CTC – Circulating tumor cells

ctDNA – Circulating DNA

DBP – Dynamic BH3 profiling

DMSO - Dimethylsulfoxide

EMT – Epithelial to mesenchymal transition

FBS – Fetal bovine serum

FPM – Functional precision medicine

GIST – Gastrointestinal stromal tumor

HSCT – Hematopoietic stem cell transplantation

HT-DBP – High-throughput dynamic BH3 profiling

IP - Immunoprecipitations

LOC – Lab-on-a-chip

μDBP – Microfluidic-based dynamic BH3 profiling

MOMP - Mitochondrial outer membrane polarization

MRD – Minimal residual disease

NK – Natural killer

OMM – Outer mitochondrial membrane

PBMC – Peripheral blood mononuclear cells

PDMS – Polydimethylsiloxane

PDX – Patient-derived xenografts

Ph+ - Philadelphia chromosome positive

PS – Phosphatidylserine

ROC – Receiver operating characteristic

ROS – Reactive oxygen species

R/R – Relapsed and refractory

TMRE - Tetramethylrhodamine

## List of proteins

ABL1 – Abelson tyrosine-protein kinase 1

AIF – Apoptosis-inducing factor

APAF1 – Apoptosis protease-activating factor 1

AP-2α – Activating enhancer-binding protein 2-alpha

ATP11A and ATP11C – ATPase phospholipid transporting 11A and 11C

BAD – BCL-2-associated agonist of cell death

BAK – BCL-2 antagonist/killer

BAX – BCL-2-associated X protein

BCL-2 – B-cell lymphoma 2

BCL-W – B-cell lymphoma W

BCL-XL – B-cell lymphoma extra large

BCR – B-cell receptor

BFL-1 – BCL-2-related isolated from fetal liver 1

BID – BH3 interacting-domain death agonist

BIK – BCL-2-interacting killer

BIM – BCL-2-interacting mediator of cell death

BMF – BCL-2 modifying factor

BOK – BCL-2-related ovarian killer

BSA – Bovine serum albumin

CAD – Caspase-activated DNAase

CDK9 – Cyclin dependent kinase 9

c-FLIP – Cellular FLICE-like inhibitory protein

DISC - Death-inducing signaling complex

DR3 – Death receptor 3

DRP1 – Dynamin 1 like protein

EGFR – Epidermal growth factor receptor

EpCAM – Epithelial cell adhesion molecule

ERK – Extracellular signal-regulated kinase

FADD - Fas-associating protein with death domain

FLT3 – Fms related receptor tyrosine kinase 3

HER – Human estrogen receptor

HRK – Activator of apoptosis harakiri

HtrA2/Omi - High-temperature requirement protein A2

iCAD – Inhibitor of the caspase-activated DNAase

IFN - Interferon

JAK – Janus kinase

MCL-1 – Myeloid cell leukemia 1

MEK – Mitogen-activated protein kinase kinase

mTOR – Mammalian target of rapamycin

NM23-H1 – Non-metastatic protein 23 H1

OMA1 – OMA1 zinc metallopeptidase

OPA1 - Dynamin-related GTPase optic atrophy 1

PAK2 - p-21 activated kinase 2

PI3K – Phosphoinositide 3-kinase

PPARγ – Peroxisome proliferator-activated receptor gamma

PUMA – p53-upregulated modulator of apoptosis

RAS – Rat sarcoma virus

RIP1 - receptor-interacting protein 1

ROCK - Rho-associated kinase

SATB1 – Special AT-rich sequence-binding protein-1

SMAC - Second mitochondria-derived activator of caspase

STAT – Signal transducer and activator of transcription

TGF-β – Transforming growth factor β

TL1A – TNF-like ligand 1A

TNF – Tumor necrosis factor

TRAIL – TNF-related apoptosis-inducing ligand

TRADD - TNFR1-associated death domain protein

TREX1 – Three prime repair exonuclease 1

XIAP - X-linked inhibitor of apoptosis protein

Xkr8 – XK related protein 8

# Chapter I

Introduction

## 1.1. Pediatric cancer and leukemia

In ancient Greece, the physician Hippocrates started to name *karkinos* to his patients' tumors, Greek for crab. Many years later, cancer (the Latin equivalent for crab) is used to define the group of diseases sharing an abnormal growth of cells with the ability to invade other tissues[1]. In 2020, almost 20 million new cases of cancer were diagnosed and 10 million deaths[2], remaining one of the main causes of death worldwide and representing an important health problem.

### 1.1.1. Pediatric cancer

Cancer in children and young adults is uncommon compared to the whole population. However, more than 200.000 people under 19 years old were diagnosed with cancer worldwide in 2020[2]. In high-income countries, around 80% of cases are cured[3], but the survival rates in the low-income ones are worse[4]; being pediatric cancer the first cause of death in children.

Pediatric cancers present important differences compared to adult since they are not usually caused by environmental factors. Furthermore, only a small subset of cancers present hereditary factors, and the cause for genetic alterations that lead to cancer remain mostly unknown. Another difference with adult cancers is tumor location. While overall highest incidence cancers are breast, prostate, lung and colorectal, in children between 0 and 19 years old the most prevalent cancers are leukemias, brain tumors and lymphomas[2] (Figure 1).

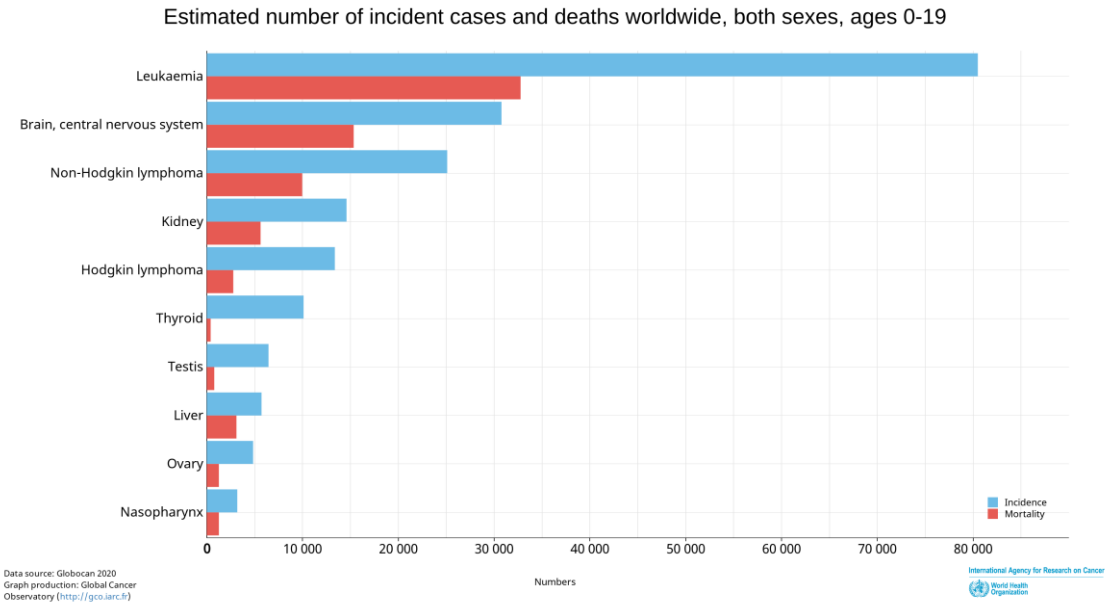

**Figure 1. Crude incidence (in blue) and mortality (in red) of different types of cancer in childs and young adults from 0 to 19 years old in the year 2020**. Data from Ferlay J, Ervik M, Lam F, Colombet M, Mery L, Piñeros M, Znaor A, Soerjomataram I, Bray F (2020). Global Cancer Observatory: Cancer Today. Lyon, France: International Agency for Research on Cancer. Available from: https://gco.iarc.fr/today

In general, pediatric cancers have better outcomes than adult cancers. Children tolerate better high doses of treatment, which may explain their higher survival compared to adults. Nevertheless, chemotherapeutic treatments cause deleterious side effects that include nausea, fatigue, allergic reactions, or the immune system weakening that leads to infections. Moreover, children are highly affected by chemotherapies that target proliferating cells as they are treated during development. Despite pediatric patients are often cured, anticancer treatments can cause health complications such as cardiomyopathy, stroke, pulmonary fibrosis, osteopenia, or intellectual and cognitive impairments, among others. Moreover, pediatric cancer patients have 19 times more probabilities to develop secondary tumors in their lives[5]. Altogether, treatment for pediatric cancer patients is effective but induces devastating side effects, highlighting the urgent need for new therapies that are equally efficient but without undesired toxicities.

### 1.1.2. Pediatric leukemia

Leukemias account for approximately one-third of all pediatric cancers. These tumors arise from an uncontrolled growth of hematopoietic cells. They typically origin in the bone marrow, where these cells are produced, and due to their accelerated growth they rapidly displace healthy immune cells. Over time, cancer cells move into the bloodstream from where they can invade other organs such as the spleen, the lymph nodes, the liver or the central nervous system. Depending on the origin of these tumoral cells, pediatric leukemias can be classified as acute lymphoblastic leukemia (ALL) arising from lymphocytes, acute myeloid leukemia (AML) from myeloid cells and mixed lineage leukemias from cells that present characteristics from both lineages (Figure 2). In some cases where the growth of cancer cells is not accelerated, they are defined as chronic lymphoblastic leukemia (CLL) or chronic myeloid leukemia (CML). Chronic leukemias are more prevalent in adults, but they can also be found in children. Similarly as for other pediatric cancers, the underlying causes for pediatric leukemias seem to be multifactorial and not completely understood. There are several genetic risk factors, such as Down's syndrome which increases 20-fold the chance of developing leukemia[6], but these factors only explain a fraction of all the cases. Some evidence

suggest a two-step process, where at first genetic changes occur *in utero* but are not sufficient to develop leukemia, and secondary genetic changes caused by exposure to different agents (for example an infection) causing the malignant proliferation of hematopoietic cells[7].

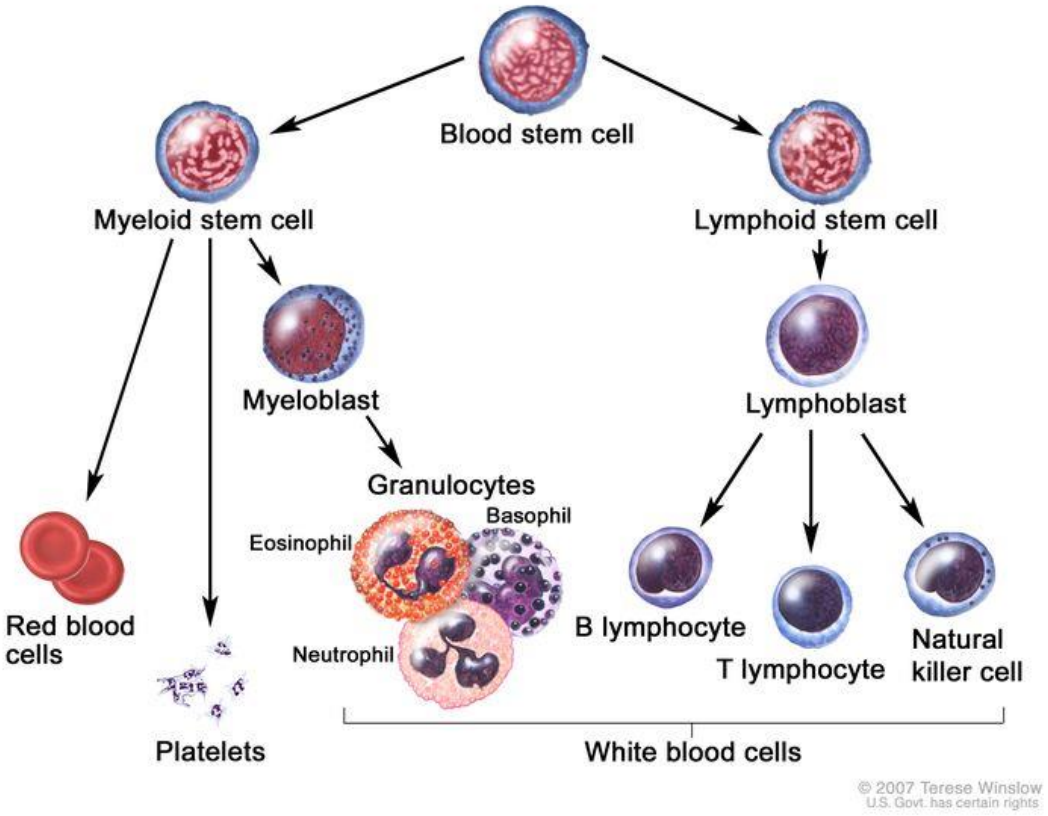


**Figure 2. Hematopoietic system development in the bone marrow.** All cell types arise from a stem cell that differentiates in the two distinct subtypes, myeloid precursors and lymphoid precursors. From cancer.gov.

Patients with pediatric leukemia can suffer anemia, thrombocytopenia or neutropenia caused mainly by the bone marrow occupation by cancer cells, where healthy cells are compromised. The most usual symptoms include fever, bruising and bone pain, while infiltration to other organs can produce other symptoms depending on the site of invasion[8]. Blood counts are the initial line of diagnosis to identify pediatric leukemias since hematopoietic cells are first affected by this disease. However, the final diagnosis is performed using bone marrow aspirates (and sometimes also peripheral blood). Cells from the bone marrow are morphologically studied to identify abnormalities and immunophenotypically characterized by flow cytometry using specific markers to determine the type of leukemia. Lastly, lumbar puncture is usually performed to discard central nervous system infiltration of the tumor. Clinicians use bone marrow aspirates

to identify the number of leukemic cells compared to normal cells and monitor the disease progression, or minimal residual disease (MRD). Classically, this determination was performed using light microscopy and applying a cutoff of 1 blast per 20 healthy cells to determine remission, but new techniques like flow cytometry or tumor-specific amplification with PCR allow the identification of up to 1 blast in 100,000 healthy cells, increasing sensibility in the detection of leukemic cells[9,10].

Depending on the subtype and different risk factors, treatment of pediatric leukemias may vary to achieve a complete remission. Chemotherapy combinations which include vincristine, anthracyclines, L-asparaginase and corticosteroids, among others are normally used to treat pediatric leukemias. Depending on the subtype, targeted drugs can also be used to inhibit specific genetic alterations such as imatinib or derived treatments for cells presenting the *BCR-ABL1* fusion gene[11], or gemtuzumab ozogamicin[12] and venetoclax[13] for AML. In some cases, bone marrow transplantation is necessary to maintain a complete remission and avoid relapse. Finally, in recent years the use of immunotherapy has greatly improved the efficacy of pediatric leukemia treatment[14]. With the inclusion of new therapeutic strategies, the prognosis has improved over the years, achieving 5-year survival rates of 90% for ALL and 70% for AML. Even with these good survival rates, there are subgroups of childhood leukemia with worse prognosis that require more aggressive treatments.

### 1.1.3. B-cell precursor acute lymphoblastic leukemia

Three out of four pediatric leukemias are ALL. Depending on the cell type precursor, these can be classified as T-cell ALL or B-cell precursor ALL (BCP-ALL). Our research is focused on the BCP-ALL subtype since it accounts for 85% of all pediatric ALL cases[15].

#### *1.1.3.1. Genetic classification*

BCP-ALL patients can be classified in several subgroups based on different recurrent genetic alterations. These subgroups are normally used as a risk stratification tool since there is a good correlation with the malignancy of the tumor. These genetic alterations include aneuploidies and chromosomal translocations, generating oncogenic fusion proteins (Figure 3). The World Health Organization established an official classification in 2016[16], but during the past years new studies have increased the subgroups used to classify BCP-ALL patients. Further genetic changes are present in the cancer cell, as every subtype has secondary alterations in different pathways

that promote tumor progression[17]. For example, variations in the RAS pathway are normally observed in the hyperploid subtype or JAK mutations in the *BCR-ABL1*-like subtype. These heterogeneous secondary alterations can partially explain the different clinical responses observed in patients from the same subgroup[18]. Moreover, the characterization of these genetic variants allowed the inclusion of different targeted therapies that improved treatment efficacy. Despite these advances in newly diagnosed patients, relapsed patients often present resistant cells with different adaptations[19], which are not completely understood and hamper risk stratification.

Alterations in chromosome number lead to different subtypes of BCP-ALL. The most common, accounting for 20-25% of all cases, is hyperdiploidy in leukemic cells that gained at least 5 chromosomes and it is associated with a good disease prognosis. Amplification of chromosome 21, also known as iAMP21, represents around 3% of the pediatric cases and with actual treatment regimens it is also considered a good prognosis subtype. Finally, chromosome loss, or hypodiploidy with less than 44 chromosomes, has been detected; with cases of near-haploidy (24 to 29 chromosomes), low-hypodiploidy (ranging between 33 and 39 chromosomes), high-hypodiploid (40 to 43 chromosomes) and near-diploid with 44 chromosomes. All these subtypes represent a minority, only 1-2% of the total cases, but with worse prognosis[17].

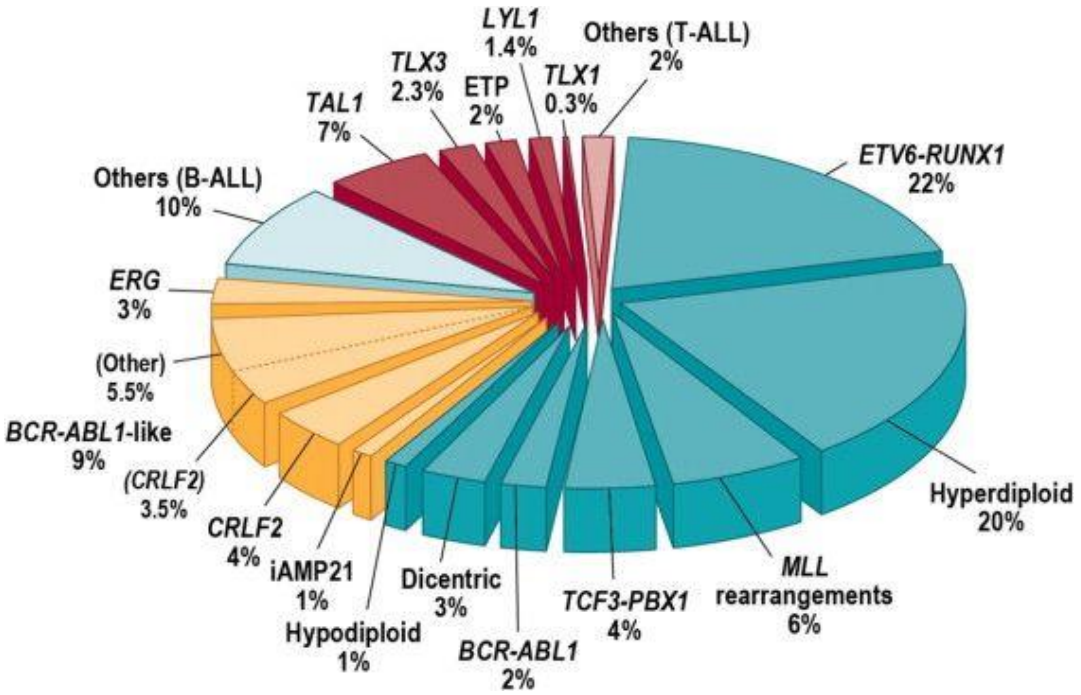


**Figure 3. Subclassification of childhood ALL.** Blue wedges refer to B-cell precursor ALL, yellow to recently identified subtypes of B-ALL, and red wedges to T-lineage ALL. From Mullighan CG. Genomic characterization of childhood acute lymphoblastic leukemia. Semin Hematol. 2013 Oct;50(4):314-24. doi: 10.1053/j.seminhematol.2013.10.001. Epub 2013 Oct 4. PMID: 24246699; PMCID: PMC3848419.

Other genetic alterations include chromosome translocations that generate fusion proteins. Around 25% of patients present the favorable translocation t(12;21) (p13;q22), which encodes for the fusion gene *ETV6-RUNX1. KMT2A* (*MLL*) rearrangements that affect approximately 5% of patients and are associated with a poor prognosis. Other translocations that account for around 5% of cases include the *TCF3-PBX1* and the *BCR-ABL1* gene fusion (Philadelphia chromosome-positive or Ph+). Interestingly, the treatment of patients that belong to these subgroups has clearly improved with the use of tyrosine kinase inhibitors such as imatinib for Ph+ cases[11]. Rearrangements on *DUX4*, *MEF2D* and *ZNF384* genes lead to other subgroups with an incidence of around 5% with different prognoses. Lastly, the fusion gene *TCF3-HLF* accounts for a minority of the cases but presents the worse prognosis of all the chromosomal rearrangement subgroups[17].

When none of the genetic changes mentioned above are detected, patients are classified as "other BCP-ALL". However, new insights have identified molecular signatures that help to further stratify these patients. The most important groups are the *BCR-ABL1*-like (or Ph-like) and the *ETV6-RUNX1*-like subgroups, accounting for 15% and 3% of the cases, respectively. They do not present the fusion gene, but they have similar transcriptional profiles as the observed in tumors with these rearrangements. Furthermore, *PAX5* translocations, mutations in *IKZF1* and rearrangements on *IGH* or *NUTM1* have been identified in a minority of pediatric BCP-ALL patients, extending the knowledge of the genetic background of this disease.

#### *1.1.3.2. Treatment for BCP-ALL patients*

Over the years, the development of new treatments and risk stratification based on different factors have significantly improved pediatric ALL patients' response, achieving a 5-year survival rate of almost 95% (Figure 4). However, current strategies have reached an efficacy plateau and new therapies are needed to further improve ALL treatment[20]. Risk-based treatments allow the use of milder chemotherapy with fewer side effects in cases with good prognosis and more aggressive combinations to increase the elimination of high-risk subtypes tumors. Several factors have shown prognostic value for risk stratification[21] such as the age, white blood cells count at diagnosis or leukemia infiltration in the central nervous system or the testes, among others. As mentioned above, genetic abnormalities are also used to assign treatments. Lastly, throughout the treatment process, MRD is used to determine treatment efficacy and to adapt the therapy to make it more aggressive or to reduce side effects.

Moreover, MRD also predicts future relapses and allows clinicians to adapt consolidation treatment decisions[22].

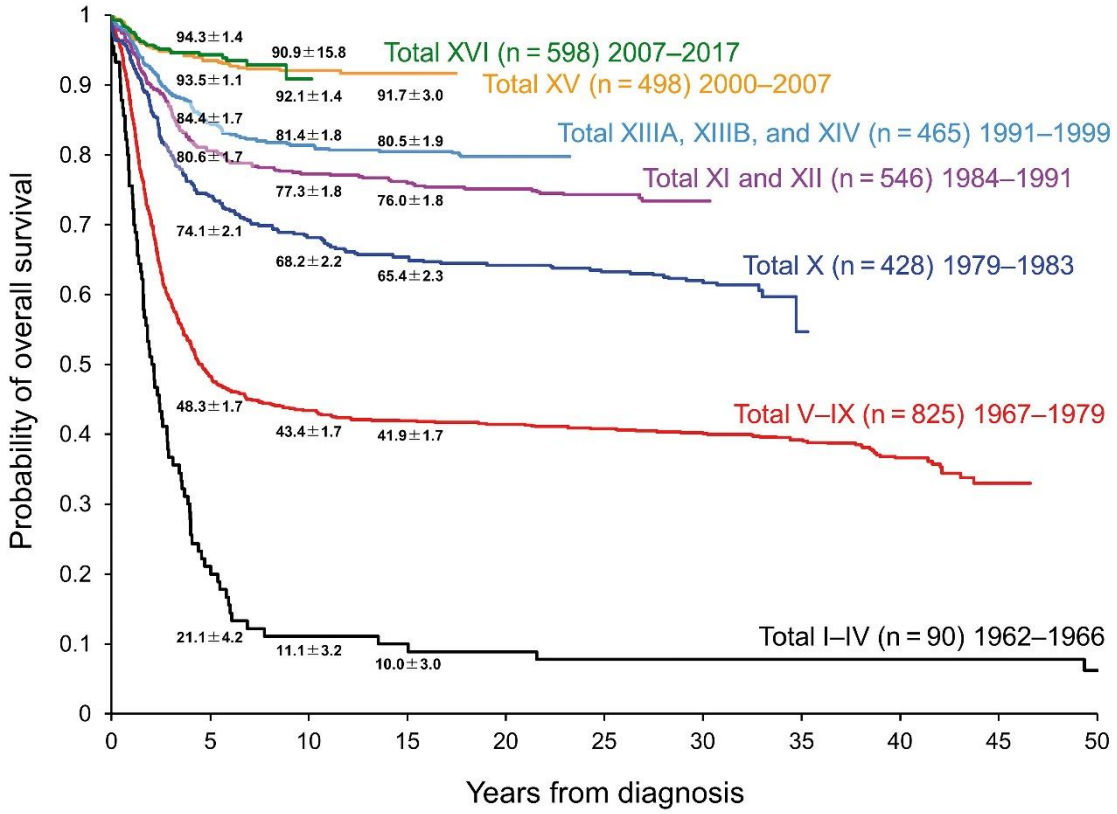


**Figure 4. Change in overall survival of pediatric patients treated on the historical St. Jude Total Therapy studies.** From Inaba H, Mullighan CG. Pediatric acute lymphoblastic leukemia. Haematologica 2020;105(11):2524-2539; https://doi.org/10.3324/haematol.2020.247031. Licensed under CC BY-NC 4.0.

The first phase of treatment after diagnosis is the remission induction part. The objective of this 4 week-regime is to achieve a complete remission eliminating all cancer cells using chemotherapy. In fact, 98% of the patients are successfully treated with this strategy. Of the remaining 2%, half of them die because of treatment-related toxicities and the other half present disease progression[23]. The induction phase has three main drug components; 1) vincristine, a vinca alkaloid that interacts with tubulin and impairs mitosis, 2) a corticosteroid such as dexamethasone or prednisone and 3) L-asparaginase (including PEG-asparaginase, *E. coli* L-asparaginase or *Erwinia* L-asparaginase), an enzyme that depletes plasma levels of asparagine and affects leukemic cells' metabolism. In high-risk patients, an anthracycline (either doxorubicin or daunorubicin) is added to the treatment regime, which intercalates into the DNA and blocks DNA and RNA synthesis in replicating cells.

When a complete remission is achieved, patients enter a long process with different phases to ensure that the cancer is fully eliminated. Most protocols are based on the Berlin-Frankfurt-Münster strategy[24], including those from the National Cancer Institute in the United States and the Sociedad Española de Hematología y Oncología Pediátrica in Spain. This protocol includes 4 main phases:

1) Consolidation: Treatment with cyclophosphamide (DNA crosslinker), mercaptopurine (inhibitor of purine synthesis) and low-dose cytarabine (antimetabolic agent).
2) Interim maintenance: Four administrations of high-dose methotrexate (inhibitor of DHFR).
3) Reinduction: With the same drugs used in the remission induction and the consolidation phases.
4) Maintenance: Daily mercaptopurine and weekly low-dose methotrexate. In difficult cases, vincristine and corticosteroid are also included. Generally, this phase is extended for up to 2-3 years after complete remission.

All the drugs included in the treatment regime are cytotoxic and cause side effects. Risk stratification, as explained above, helps to adapt therapy to reduce dosing and avoid short and long-term secondary effects. In high-risk patients, aggressive treatments are used to achieve complete elimination of the tumor, but they also reduce patients' quality of life.

Along with this complex regime, other interventions are applied to solve different problems caused by BCP-ALL. During treatment, several drugs are included to avoid Central Nervous System (CNS) infiltration of blasts, even if they do not present CNS compromise at diagnosis. Some agents used in the standard protocol, such as dexamethasone, L-asparaginase and methotrexate already affect infiltrated leukemic cells at the CNS. However, to further eliminate blasts, intrathecal chemotherapy is added during treatment. Depending on the risk factor, methotrexate alone or in combination with cytarabine and hydrocortisone may be injected into the spinal cord[25]. In very high-risk or refractory to the induction phase patients, hematopoietic stem cell transplantation (HSCT) might be used to improve treatment efficacy, but it is normally employed in relapsed patients[26].

Thanks to the increased knowledge on genetic BCP-ALL profiles, different therapies are being added to the treatment regime to improve efficacy. The most successful example are ABL1 inhibitors for *BCR-ABL1*-positive patients, which include imatinib

and the second-generation agent dasatinib. The addition of both inhibitors to chemotherapy regimens have increased the 5-year free survival rate[11,27]. Other options explored in clinical trials include the monoclonal antibodies blinatunomab (against CD19) and inotuzumab ozogamicin (against CD22), that have demonstrated therapeutic efficacy in relapsed and refractory (R/R) BCP-ALL patients[28,29]. Engineered CAR T cells against CD19 and CD22 have also been evaluated to treat R/R BCP-ALL patients with encouraging results[30,31]. However, leukemic cells often adapt and now a bivalent CAR T platform to target both CD19 and CD22 is under study[32]. Other preclinical studies suggested different targeted agents to enhance chemotherapy. For example, some cases of the *BCR-ABL1*-like subtype responded to dasatinib. Furthermore, more than 50% of them present JAK-STAT signaling activation that could be inhibited by ruxolitinib[33]. Finally, the BCL-2 inhibitor venetoclax (which will be extensively reviewed in further sections) has shown therapeutic efficacy in multiple hematological malignancies. In fact, several BCP-ALL subtypes, including *KMT2A*-rearranged, *Ph+* and *TCF-HLF*, have shown to be dependent on BCL-2 and sensitive to its inhibition with venetoclax in preclinical models[34–36].

In relapsed cases, patients are still risk-stratified based on the different factors commented above. These patients enter a reinduction phase like the first induction on high-risk BCP-ALL, or an alternative regime that includes high-dose methotrexate and cytarabine. After this reinduction, almost 85% of patients achieve a complete remission again[37]. Then, patients follow a chemotherapy regime or a HSCT, but the overall survival of relapsed patients is less than 50%. Posterior relapses are usually more aggressive and complete remissions are more difficult to obtain, emphasizing the need for new therapeutic strategies for R/R BCP-ALL patients.

## 1.2. Apoptosis

### 1.2.1. Morphological discovery of apoptosis

Apoptosis is a physiological process that removes old or damaged cells[38]. It is activated by different stimuli such as immune reactions, tissue damage and a wide variety of agents[39]. Kerr and colleagues first described apoptosis in 1972 when they characterized a programmed process of cell deletion with nuclear and cytoplasmic condensation forming the so-called apoptotic bodies, that are later phagocytized and degraded by other cells[40]. The process was described in 1972, but individual characteristics of this mechanism were previously found, such as the formation of small cytoplasmatic vesicles with condensed chromatin[41,42] and its characterization by electron microscopy[43,44]. These findings led to the identification of shrinkage necrosis (the first term used to refer to the apoptotic cell death process) in multiple processes such as embryonic development, cellular turnover in adult tissue and in response to treatment in tumor cells, which led to the description of the structural characteristics of this type of programmed cell death[40].

Morphologically, the apoptotic process starts with cell shrinkage and pyknosis (irreversible condensation of chromatin). Later, the “budding” stage appears, characterized by plasma membrane blebbing (membrane protrusions typically found in the apoptotic process), the separation of cell fragments and the formation of apoptotic bodies (cytoplasm pieces with tightly packed organelles and in some cases nuclear fragments enclosed in the plasma membrane). The elimination of these apoptotic bodies is achieved by phagocytic cells and degraded in phagolysosomes[45]. In general, this regulated process avoids intracellular material release to not trigger an inflammatory response upon cell death[46]. Typically apoptotic cells inhibit the inflammatory response, for example with the release of TGF-β or the activation of PPARγ that blocks the production of inflammatory cytokines[47]. This process differs from necrosis, which is characterized by cellular swelling and plasma membrane breaking which leads to an inflammatory response[48]. However, apoptosis is not always immunologically silent[49] and recent studies showed that the liberation of mitochondrial DNA in response to apoptotic activation induces the production of IFN and subsequent immunogenic cell death[50].

### 1.2.2. Molecular mechanism of apoptosis

First insights on the molecular mechanism involved in apoptosis were observed in the development of *Caenorhabditis elegans*[51]. Apoptosis is an energy-dependent cellular program controlled by caspases, a group of cysteine-aspartic proteases that initiate and execute this pathway. This process is activated autonomously as a cellular suicide program or triggered by the interaction between an immune cell with a damaged cell[52]. Three distinct pathways that initiate apoptotic cell death and converge in the same execution mechanism have been described.

#### *1.2.2.1. Caspases*

A dozen different caspases have been identified in humans, and more than half of them are implicated in the apoptotic process (including the initiator caspases 8, 9 and 10 and the executioner caspases 3, 6 and 7). Caspases recognize specific four-residue sequences of other proteins and cleaves a cysteine-histidine dyad in the target protein[53]. All caspases are produced as inert proenzymes with a prodomain, containing a p20 and a p10 domains that remain inactive until there is a cleavage between them[54], which exposes the substrate specificity pocket. The active form always presents two p20/p10 heterodimers and two active sites[55]. Executioner caspases are activated by upstream caspases forming a cascade that amplifies the apoptotic signaling. However, most initiator caspases become active by other means, including caspase-8 (explained in the extrinsic pathway section) and caspase-9 (explained in the intrinsic pathway section).

Once initiated, apart from activating downstream caspases, these proteins cleave other substrates, activating or inactivating target proteins. Most proteins altered by caspases are involved in apoptosis, such as endonucleases (for DNA fragmentation), nuclear laminins (that cause nuclear shrinking and budding), cytoskeletal proteins (that compromise the cellular structure) and proteins that regulate apoptotic blebbing[56]. The function and regulation of all these proteins will be further discussed in the execution pathway section.

#### *1.2.2.2. Extrinsic pathway*

The orchestrators of the extrinsic activation of apoptosis are the death receptors which are trimeric transmembrane receptors from the TNF receptor superfamily[57]. These receptors present an extracellular region rich in cysteine and a death domain in the

intracellular region[58]. Each receptor has its corresponding death ligand, also trimeric transmembrane proteins from the TNF family produced by different cell types that typically promote cell death. Both receptor and ligands organize themselves in a trimeric way[59], which is indispensable for the activation of the apoptotic cascade[60] (Table 1).

| Death receptor | Death ligand |
|---|---|
| TNFR1 (also p55)[61] | TNF and lymphotoxin a[58] |
| FASR (also CD95 or Apo1)[62] | FASL (also CD95 ligand)[63] |
| DR3 (also TRAMP, WSL-1, Apo3 or LARD)[64] | TL1A[65] |
| TRAIL-R1 (also DR4)[66] | TRAIL (also Apo2 ligand)[67] |
| TRAIL-R2 (also DR5, Apo2 or KILLER)[67] | TRAIL (also Apo2 ligand)[67] |

**Table 1.** Known death receptors and their corresponding ligands.

Death receptors are crucial for the transmission of the death signal from outside the target cell to the cytoplasm. FAS and TRAIL receptors, when they are activated by their death ligands, recruit FADD[68] to form the death-inducing signaling complex or DISC[69]. Regarding TNFR1 and DR3, once activated by the corresponding ligand, recruit TRADD[70]. Both the receptor and TRADD assemble with RIP1 and a series of ubiquitin ligases that define the function of the complex. When there is a compromised ubiquitination of RIP1, TRADD and RIP1 they detach from TNFR1 and recruit cytosolic FADD[71], forming a complex that works similarly to DISC. FADD in the DISC interacts with procaspase-8 monomers and brings two of them to close proximity, exposing their active sites and triggering its activation. This autocatalytic activity causes the activation of caspase-8 and the stabilization of the complex avoiding inactivation by spontaneous changes in their structure. Active caspase-8 engage other executioner caspases and cleaves BID that activates the intrinsic pathway (explained below), multiplying the apoptotic cascade[72]. Intracellular regulation of the extrinsic pathway can prevent apoptotic cell death after the interaction between the death receptor and its ligand, being the most important proteins c-FLIP that blocks FADD and caspase-8[73] and Toso that inhibits caspase-8 cleavege[74].

#### *1.2.2.3. Perforin/granzyme pathway*

Cytotoxic T-cell lymphocytes and natural killer (NK) cells can induce apoptosis using their death ligands. However, they can also induce apoptotic cell death in virus-infected cells or transformed cells independently of the death receptor pathway. When these cells recognize a specific target (peptide-MHC complexes for T-cell lymphocytes and positive stimulatory signals in NK cells[75]) there is an increase in cytosolic $Ca^{2+}$ that causes the movement of the microtubule-organizing center towards the malignant cell that has to be eliminated. Cytotoxic granules use the microtubules to migrate and fuse with the membrane releasing their cargo to the extracellular space[76]. Perforin is one of the proteins present in these cytotoxic granules and assembles itself to insert in the target cell plasma membrane and form pores[77]. This allows the entry of other proteins present in the cytotoxic granules such as granzyme proteins. Granzyme B provokes a fast induction of apoptosis by cleaving different key proteins involved in the apoptotic pathway; 1) activation of executioner caspases 3 and 7 that directly induce apoptosis[78] and 2) BID cleavage and further activation of executioner caspases via the intrinsic pathway[79]. On the other hand, granzyme A induces apoptotic cell death in a caspase-independent manner acting in different key processes, for example impairing ATP generation and producing reactive oxygen species (ROS)[80], cleaving SET and impairing its function of preserving chromatin structure and promoting DNA repair and liberating endonucleases that cause DNA degradation[81]. Interestingly, cytotoxic T-cell lymphocytes and NK cells are resistant to the cytotoxic granules that they excrete[82], enabling the elimination of multiple malignant cells.

#### *1.2.2.4. Intrinsic pathway*

The intrinsic pathway of apoptosis involves a series of intracellular signaling independently of receptors. The central part of this process is the mitochondrial outer membrane permeabilization (MOMP) that marks cell's commitment to apoptotic cell death[83]. Intrinsic apoptosis can be initiated by 1) the absence of growth factors, hormones or cytokines, 2) the presence of damaging agents such as radiation, toxins, hypoxia, hyperthermia, viral infections, cytotoxic agents or free radicals[45] or 3) cellular alterations such as DNA damage, endoplasmic reticulum stress, microtubular alteration or mitotic defects[84]. These proapoptotic stimuli affect the mitochondrial membrane integrity and finally induce MOMP[85], which liberates different proteins from the intermembrane space of the mitochondria to the cytosol[86]. The BCL-2 family of proteins, which will be extensively reviewed in the following section, tightly regulates MOMP.

After MOMP, cytochrome c is released to the cytosol, where it binds to Apaf-1 and procaspase-9 to form the apoptosome[87]. This complex is formed by the oligomerization of seven APAF1-cytochrome-c units in an ATP-dependent process, which produces conformational changes that expose the WD region of APAF1 and favors the binding of procaspase-9 to the center of the apoptosome, engaging its auto-proteolytic activation[88]. Active caspase-9 can then activate downstream caspases when is bound to the apoptosome, but procaspase-9 has a higher binding affinity to the activation complex. This causes the formation of a "molecular timer" characterized by the continuous binding/activation/processing/release of caspase-9 dependent on the concentration of free procaspase-9, which tightly controls the duration of the executioner caspases activation[89]. SMAC (or DIABLO) and OMI are also released when MOMP is engaged and block the activity of XIAP, preventing its antiapoptotic activity (inhibition and marking for degradation of caspase-9, caspase-3 and caspase-7)[90]. In a second phase, several proapoptotic proteins including AIF and endonuclease G (that do not need caspase activation) and CAD (that has to be activated by caspase-3) also escape from the mitochondria and translocate to the nucleus where they produce DNA fragmentation and chromatin condensation[91–93].

MOMP is the critical step for apoptotic cell death[94]. Inhibition of caspases does not avoid cell death, since MOMP impairs essential metabolic processes of the cell. Partial MOMP, where only some mitochondria are depolarized can avoid caspase activation[95], but this process causes genomic stability and promotes that cells become tumorigenic[96].

#### *1.2.2.5. BCL-2 family of proteins*

The balance between proapoptotic and antiapoptotic proteins from the BCL-2 family determines MOMP engagement. All the members of this family contain from one up to four BCL-2 homology (BH) domain, from BH1 to BH4[97].

Pore-forming proteins, also known as effector BCL-2 proteins, include BAX, BAK and BOK. These proteins contain BH1-BH3 domains and are the effectors of MOMP. BAX and BAK, that share the same sequences in their BH domains, are found in different parts of the cell. BAX is soluble and present in the cytosol in its inactive form and translocates to the mitochondria once activated, while BAK is anchored in the outer mitochondrial membrane (OMM). Both proteins are monomers in their inactive form and once activated they expose their BH3 domain that inserts in the hydrophobic groove of another effector protein to form an homodimer[98], that later oligomerize with

other effectors to form pores in the OMM[99]. Several studies have proposed how these homodimers assemble to form a toroidal pore[100], but the exact mechanism is still unclear. Once pores are formed, cytochrome c and other proteins involved in the intrinsic pathway are released to the cytosol[101]. BOK presents a similar structure as BAX and BAK, but its function has not been fully characterized. Studies with double knock-out (BAX and BAK) and triple knock-out (BAX, BAK and BOK) demonstrate that BOK also acts as an effector protein and can be redundant with BAX and BAK[102]. However, BOK is not affected by BH3-only proteins, and seems to be constitutively active and controlled by proteosomal degradation. Thus, if proteasomal activity is compromised, BOK is stabilized to induce MOMP and cell death[103].

BH3-only activator proteins BIM and BID, that only present a unique BH3 domain, directly activate BAX and BAK[104]. Regarding BID, the active truncated form is generated by caspase-cleavage (known as tBID). Interestingly, both activators interact with BAX and BAK, but BIM has a higher affinity to BAX and tBID to BAK[105]. Activator proteins engage BAX and BAK to expose their BH3 domain inducing the dimerization with another activated effector protein. This is a “hit and run” process that allows the activator to perform its function again. PUMA and NOXA which are normally classified as sensitizer proteins (see below), can marginally activate BAX and BAK, yet with a lower extent compared to BIM and tBID[106,107]. Because all these activator proteins present a BH3 domain, they can also block antiapoptotic proteins (explained below) and neutralize their pro-survival activity. BIM and PUMA are controlled transcriptionally while BID is cleaved post-translationally as a regulation mechanism.

Antiapoptotic BCL-2 proteins protect cells from apoptosis by inhibiting both the effector and activator proteins. This group of proteins includes BCL-2, BCL-xL, MCL-1, BCL-W and BFL-1, and all of them contain four BH domains. The BH1-BH3 domains from these proteins form a hydrophobic groove that binds to the BH3 domain from the proapoptotic proteins[108], which is exposed in active effector proteins and in the activators. All antiapoptotic proteins have a high affinity for the activator proteins (BIM and tBID), yet they have different affinities to effector proteins. BAX is recognized by all antiapoptotic proteins, being BCL-xL the one that has less affinity. However, only BCL-xL, BFL-1 and MCL-1 bind and block BAK[97]. Apart from direct inhibition of effector proteins, BCL-xL can retrotranslocate BAX and BAK to the cytosol diminishing the cell’s ability to form mitochondrial pores and protecting them from apoptosis[109].

A fourth group of proteins called sensitizers, presenting only a BH3 domain, favor apoptosis by inhibiting the antiapoptotic proteins, thus displacing activators and

effectors. BAD, BIK, BMF, HRK, NOXA and PUMA present different affinities for the antiapoptotic proteins, which are summarized in Figure 5[110].

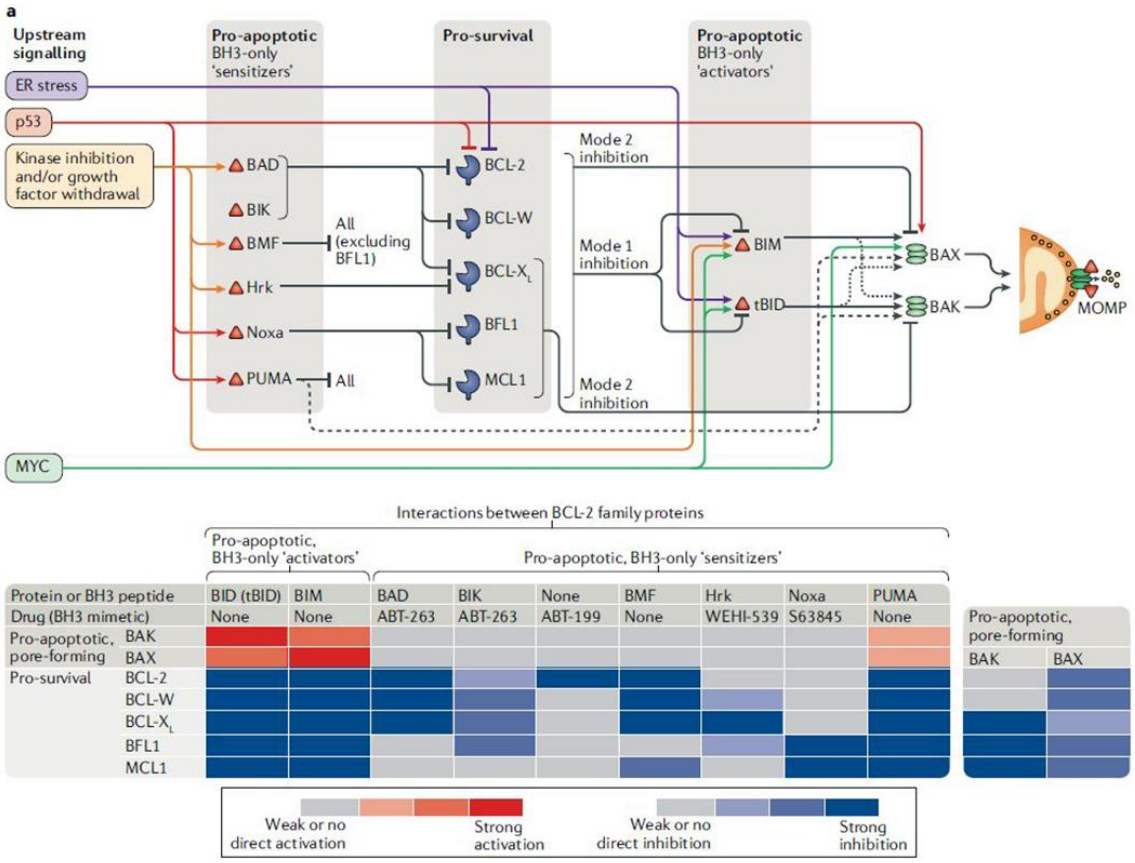


**Figure 5. BCL-2 familiy of proteins and their interactions.** Top: scheme of the interactions between the BCL-2 family of proteins and the effect of different proapoptotic stimuli. Bottom: chart with the specific interactions between activator and sensitizer BCL-2 proteins and the effector and antiapoptotic proteins. Reprinted by permission from Nature Springer from Singh, R., Letai, A. & Sarosiek, K. Regulation of apoptosis in health and disease: the balancing act of BCL-2 family proteins. Nat Rev Mol Cell Biol 20, 175–193 (2019). https://doi.org/10.1038/s41580-018-0089-8.

This interconnected network of proteins represent a complex interactome, where the balance between proapoptotic and antiapoptotic proteins determines BAX/BAK activation, MOMP and apoptotic engagement[97]. Several models have been historically proposed to explain the interplay of the BCL-2 family of proteins that decide cell fate. The displacement model postulated that BH3-only proteins disrupt the blocking interaction between antiapoptotic proteins and active BAX and BAK. While the direct activation model proposed that antiapoptotic proteins blocked BH3-only activators, and other BH3-only proteins were required to liberate the activators and promote the activation of BAX and BAK. Over the years with the increasing knowledge on the BCL-2 family of proteins, there is a consensus in a unified model, where antiapoptotic

proteins block both BH3-only activators and active effector proteins, thus requiring their displacement to promote MOMP and apoptosis[111].

Every cell type expresses different levels of BCL-2 proteins that determines their predisposition for apoptosis. For instance, some cells do not express BAX and BAK, being completely refractory to apoptosis. Other cells present a high expression of antiapoptotic proteins compared to proapoptotics, which makes them poorly primed for apoptosis. Finally, when the balance between antiapoptotic and proapoptotic proteins is more even, a small change in this equilibrium can produce MOMP, a state defined as "primed for apoptosis"[112]. These differences in apoptotic priming determine cells' predisposition to undergo apoptosis and are crucial for a myriad of processes in healthy tissues. While during development tissues constantly renew, the apoptotic machinery is highly regulated which make cells "primed" for apoptosis, most adult tissues (with some exceptions such as the hematopoietic system) are refractory to apoptosis[113]. When a cell is exposed to apoptotic stimuli, the BCL-2 family balance changes. For example, DNA damaging chemotherapy upregulates BAX, PUMA and NOXA and represses BCL-2 activation through p53[114,115]. Similarly, the inhibition of different kinases cause activation of other proapoptotic proteins such as BIM or BAD that promote apoptosis[116,117]. Apoptotic priming and the role of different BCL-2 proteins in cancer cells will be extensively reviewed below.

#### *1.2.2.6. Execution pathway*

All apoptotic pathways converge in caspase-3 activation, which is the most important protein in the execution of apoptotic cell death. Normally, inactive caspase-3 (like other executioner caspases, -6 and -7) are expressed as dimers and when activated conformational changes expose two active sites. Caspase-3 cleaves multiple substrates that lead to apoptosis. In fact, around 1000 proteins have been identified as substrates for executioner caspases[118]. Caspase-3 activates the execution of apoptotic cell death and targets proteins in the nucleus, the plasma membrane, and the mitochondria, among others. Experimental studies have demonstrated that a single activation of one of the caspase-3 targets is not sufficient to induce apoptotic cell death, which shows the complex cascade that this protease triggers. That is why different authors have defined apoptosis as "death by a thousand cuts"[119].

In the nucleus, caspase-3 recognizes and cleaves proteins such as CAD, lamins and acinus, which produce DNA fragmentation[93], nuclear matrix degradation[120] and chromatin condensation[121], respectively. In the cytosol, cleavage of pp125$^{FAK}$ and α-

actinin impairs cells' ability to form peripheral adhesions and attach to the extracellular matrix[122,123] or ROCKI and PAK2 that block the correct polymerization of actin and cause the formation of blebs[124–126]. Other processes activated by caspase-3 involve changes in the cells' physiological processes, being one of the most studied p75 cleavage, a subunit of the complex I from the electron transport chain, that disrupts ATP production[127]. All these well-controlled processes end up with the clearance of the apoptotic bodies by phagocytes (including macrophages, dendritic cells and neutrophils). Executioner caspases are also involved in the clearance process inducing the production of lysophospatidylcholine which is a signal to recruit macrophages[128]. Then, exposure of phosphatidylserine (PS) at the outer leaflet of the plasma membrane functions as an "eat me" signal for phagocytes recognition and elimination. Flipases are responsible for translocating PS from the outer to the inner plasma membrane, but they become inactive during apoptosis because of the action of caspase-3[129,130]. Caspase-3 also cleaves XKR8 which promotes the formation of a scramblase complex that exposes PS to the outer plasma membrane[131].

Caspase-7 and caspase-3 show high redundancy on substrate recognition, yet studies with knockouts demonstrate that some processes during apoptosis are specific to each caspase[132]. Caspase-6 is activated by caspase-3 and -7 and exerts several unique functions. One of the substrates of caspase-6 is caspase-8, which in turn cleaves BID to induce MOMP. As active caspase-6 requires activation of caspase-3 and -7, this acts as a positive feedback loop that further amplifies cytochrome c release and caspase activation[133]. Active caspase-6 also translocates to the nucleus where it cleaves specific substrates. One of them is laminin A[134] which once activated favors nuclear disassembly and chromatin separation from the lamina[135]. SATB1 is also cleaved by caspase-6, causing its separation to loop domains that promote DNA fragmentation[136]. Other substrates specific for caspase-6 include cytokeratin 18, focal adhesion kinases, nuclear mitotic apparatus protein, β-amyloid precursor protein, topoisomerase I, transcription factor AP-2α, vimentin and hungtingtin[137].

### 1.2.3. BCL-2 family of proteins in cancer

The evasion of cell death is one of the hallmarks of cancer[138] and the BCL-2 family of proteins play a key role on this[97]. In fact, the *BCL-2* gene was discovered as an oncogene responsible for some types of B-cell lymphomas with t(14;18) translocations[139]. Almost 50% of malignant tumors present inactivation or mutations in p53, a protein that activates several genes related to apoptosis, including the proapoptotic *Bax*, *Noxa*, *PUMA* and *Bid* from the BCL-2 family of proteins[140]. MYC is

another protein that is generally overexpressed in cancer, impairing the antiapoptotic activity of BCL-2 and BCL-xL[141]. These and other examples demonstrate that cancer cells often present alterations that change the apoptotic pathway, particularly affecting the BCL-2 family of proteins.

Beyond recognizable alterations in oncogenes, changes in the BCL-2 family of proteins are usually found in cancer cells. Increased expression of antiapoptotic BCL-2 proteins are a common marker of tumors with poor prognosis and can be caused by chromosomal translocation, gene amplification, gene transcription or posttranslational processing[142]. BCL-2 overexpression is found in several B-cell malignancies and correlates with treatment resistance[143]; also causing multidrug resistance in lung cancer[144] and protection against paclitaxel in ER-positive breast cancer[145], among others. Similarly, MCL-1 increased expression correlates with treatment resistance in non-small cell lung cancer or ovarian cancer[146], while BCL-xL overexpression causes treatment failure in ovarian cancer[147]. Apart from these, genetic alterations affecting the BCL-2 family are also common in different cancers. For example, around 50% of the microsatellite subtype of colon cancer present mutations in the *BAX* gene[148], different cancers present somatic amplifications of *MCL-1* and *BCL2L1* (encoding BCL-xL) and deletions of *BOK* and *BBC3* (encoding PUMA)[149]; also loss of *BIM* has been detected in mantle cell lymphoma[150]. Just to name a few examples.

But the BCL-2 family of proteins can also dynamically change upon anticancer treatment. Most chemotherapies and targeted therapies used to treat cancer produce cell death via the intrinsic pathway of apoptosis. This causes changes in the balance between pro and antiapoptotic proteins that finally leads to apoptotic cell death. For example, MEK inhibition inactivates BIM phosphorylation which causes its accumulation therefore favoring the initiation of apoptosis[151], the increase in BAD when mutant JAK is pharmacologically inhibited[152], or the MCL-1 downregulation after mTOR inhibition in colorectal cancer[153] or CDK9 inhibition in B-cell lymphoma[154]. However, cancer cells often adapt to treatment using the antiapoptotic members of the BCL-2 family of proteins. Increased dependence on antiapoptotic proteins after treatment to avoid apoptosis is a fast process, which normally precedes other resistance mechanisms that need more time to occur such as mutations. For example, HER2-positive breast cancer becomes resistant to chemotherapy by overexpressing BCL-2[155]. Antiapoptotic adaptations after treatment are heterogeneous and vary depending on the drug and the type of cancer[156].

Altogether, the BCL-2 family of proteins play a central role in cancer cell survival and the tumorigenic process, but they also control cell death in response to anticancer treatment. Therefore, the pharmacological intervention of this family of proteins has been proposed as an important target to improve cancer therapy.

### 1.2.4. BH3 mimetics

Several strategies have emerged to pharmacologically intervene the intrinsic pathway of apoptosis. However, the most explored one is the development of compounds that mimic BCL-2 sensitizer proteins, inhibiting their antiapoptotic counterparts, thus promoting apoptosis by freeing activator and effector proteins. As mentioned, adult cancer cells are more primed for apoptotic cell death than healthy cells, and anticancer treatments change the balance between pro and antiapoptotic BCL-2 proteins. This evidence suggests that pharmacological inhibition of antiapoptotic proteins could selectively affect cancer and help to improve the elimination of malignant cells. The first examples of antiapoptotic protein inhibitors were peptides derived from the BH3 domain of sensitizer BCL-2 proteins that had specificity for the hydrophobic grove of the different antiapoptotic proteins[157]. Nevertheless, this strategy was not successful due to toxicity, low cell permeability and short lifetime of the peptide[158].

Over the last two decades, great efforts have been devoted to the development of small molecules that interact with the hydrophobic groove of the BCL-2 antiapoptotic proteins, the so-called BH3 mimetics. The first BH3 mimetics included several pan-BCL-2 inhibitors such as HA14-1, gossypol and obatoclax, which showed some activity in different cancer models but were discarded because of their low affinity and off-target effects. The first truly successful BH3 mimetic was ABT-737, and after that Abbvie developed its orally available analog navitoclax (also known as ABT-263). Both molecules target with nanomolar affinity the antiapoptotic proteins BCL-2, BCL-xL and BCL-w; and both showed *in vitro* efficacy in a plethora of cancer types, including hematological malignances and solid tumors[159]. Despite its promising efficacy *in vitro*, only a few clinical trials evaluated ABT-737 and navitoclax (clinicaltrials.gov). In most completed trials, the use of navitoclax alone or in combination with other chemotherapeutic agents clearly showed anticancer activity. However, despite the promising results, patients suffered severe side effects including thrombocytopenia caused by platelets high dependence on BCL-xL[160]. Recently, a new compound called AZD0466 with a similar affinity for BCL-2 and BCL-xL as navitoclax but not causing thrombocytopenia has been developed and is currently explored in clinical trials

(clinicaltrials.gov)[161]. However, most efforts have been focused on developing compounds targeting only one antiapoptotic protein to avoid toxicity.

#### *1.2.4.1. Inhibition of BCL-2*

Promising results with navitoclax led to the development of venetoclax (also known as ABT-199), a specific BCL-2 inhibitor that does not interact with BCL-xL, hence avoiding platelet undesired elimination. First *in vitro* results showed exceptional efficacy in cancers dependent on BCL-2, both as a single agent or in combination with other anticancer drugs[159]. When tested in clinical trials, venetoclax showed an exceptional efficacy as a single agent in relapsed CLL with a response rate of around 80% with minimal side effects[162], which ultimately led to its approval, becoming the first BH3 mimetic approved in the United States and Europe to treat relapsed and refractory CLL patients. Venetoclax has also shown efficacy in AML patients, a subtype of leukemia with low prognosis using the actual chemotherapeutic regime. Following *in vitro* studies and several clinical trials, the inclusion of venetoclax with azacytidine to treat AML patients ineligible for aggressive chemotherapy increased overall survival and complete remission status while minimally increasing side effects[163]. This clinical trial also led to the approval in mid-2021 of venetoclax to treat certain AML patients in combination with hypomethylating agents. Besides these two successful trials that positioned venetoclax as the most promising BH3 mimetic, hundreds of clinical trials started to evaluate venetoclax efficacy (clinicaltrials.gov), most of them in hematological malignancies.

Despite the single-agent efficacy of venetoclax in CLL, monotherapy efficacy is scarce. Cancer cells often adapt to BH3 mimetics through several strategies, including genomic mutations or increased activity of other antiapoptotic proteins as a compensatory mechanism. Thus, most clinical trials explore venetoclax in combination with standard-of-care treatment regimens.

#### *1.2.4.2. Inhibition of MCL-1*

MCL-1 is another antiapoptotic protein often used by cancer cells to adapt to therapy, both chemotherapy or targeted agents. In fact, after treatment with navitoclax or venetoclax, MCL-1 can sequester the free activators displaced from BCL-2 and BCL-xL to prevent apoptosis. One of the first selective BH3 mimetics against MCL-1 was A-1210477, followed by several compounds, including S63845 (and the analog compound S64315), AMG-176, AMG-397, AZD-5991, AM8621, PRT1419 and

VU661013 (all with high affinity for MCL-1 in the low nanomolar range). Unlike BCL-2, which is preferentially expressed in hematological cancers, MCL-1 has been found upregulated in several cancers, both solid and liquid tumors. Dependencies on MCL-1 have been exploited using these specific inhibitors (both as single agents or in combination with other anticancer drugs) with good *in vitro* results on diverse cancer types such as AML, breast cancer, glioblastoma or melanoma, among others[159].

Altogether, multiple clinical trials started using MCL-1 inhibitors (clinicaltrials.gov), most of them, similarly as venetoclax, to exploit their combinations with other anticancer drugs. In fact, the double inhibition of antiapoptotic proteins using navitoclax or venetoclax and an MCL-1 inhibitor has been extensively used in preclinical models of solid and liquid tumors showing highly synergistic cytotoxic effects[164,165]. By the end of 2022, two clinical trials started in hematological malignances using the combination of venetoclax and an MCL-1 inhibitor (NCT03797261 and NCT03218683), but both of them have been suspended or terminated due to safety reasons. This has become the main concern in the clinical development of MCL-1 inhibitors. Preclinical studies and early clinical trials did not show important side effects, but in the most recent trials, cardiac toxicity related to MCL-1 inhibition has been observed, causing the termination of several clinical trials and putting on hold the development of these BH3 mimetics.

#### *1.2.4.3. Inhibition of BCL-xL*

As mentioned above, inhibition of BCL-xL induces important side effects due to the platelets´ elimination. Nevertheless, several specific inhibitors against BCL-xL have been developed including WEHI-539, A-1155463 and A-1331852. Particularly, preclinical studies using the latter have shown cytotoxic activity as single-agent or in combination with other treatments in different cancers, for example rhabdomyosarcoma and lymphoma[166,167]. However, these limitations due to side effects caused a lack of clinical trials exploring BCL-xL inhibitors. Recently, new compounds using the PROTAC technology have been proposed as an alternative to reduce platelet toxicity while eliminating BCL-xL dependent cancer cells. This molecule remains inactive until it enters the cancer cell, where it binds to BCL-xL and promotes its ubiquitination and posterior degradation by the proteasome[168].

#### *1.2.4.4. Other BH3 mimetics*

A different alternative explored regarding the BCL-2 family is directly activating effector proteins to induce apoptosis. For instance, the development of BTSA1, acts as an

analog of BIM or BID, binding to BAX and triggering its activation to start the apoptotic process. Preclinical studies using this BH3 mimetic have demonstrated cytotoxicity in AML cell lines and patient samples without affecting healthy cells; and increased survival in AML xenograft models[169]. More recently, the new orally bioavailable version BTSA1.2 has demonstrated synergistic effects with navitoclax in colorectal cancer PDXs[170].

In summary, BH3 mimetics have gained importance in cancer treatment in the last decades due to the outstanding venetoclax activity in CLL as a single agent. However, treatment with BH3 mimetics a single agents are effective only in a few types of cancer. Thus, current investigations focus on combining these molecules to current treatments, with the objective to exploit antiapoptotic addictions both intrinsic to the tumor or caused by drugs. This strategy requires the development of biomarkers to effectively guide the use of these BH3 mimetics, hence there is an important need for techniques that accurately predict their efficacy and guide their use in the clinic.

## 1.3. Precision medicine for cancer

### 1.3.1. Precision medicine

The National Cancer Institute defines precision medicine, or personalized medicine, as "the form of medicine that uses information about a person's own genes or proteins to prevent, diagnose, or treat disease. In cancer, precision medicine uses specific information about a person's tumor to help make a diagnosis, plan treatment, find out how well treatment is working, or make a prognosis"[171]. Classically, cancer patients are stratified based on different factors (such as the type of cancer, age, gender among many others) to assign the most suitable treatment regime to maximize tumor elimination while minimizing side effects. Over the years, precision medicine has improved cancer treatment and the quality of life of patients. However, risk stratification is mostly based on tumor type and patients' molecular characteristics, while tumor dynamic biology is understudied.

The first example of treatment assignment based on tumor characteristics was the inclusion of tamoxifen to the normal chemotherapeutic regime in estrogen receptor-positive breast cancers, which reduced treatment failure and increased disease-free survival[172]. With the improvement of genomic technologies and the elucidation of the Human Genome Atlas, different targetable genomic alterations have been identified in different cancers. One of the most successful examples is the use of imatinib in patients with chronic myeloid leukemia presenting the fusion protein BCR-ABL, that showed superior efficacy compared to the standard-of-care treatment, and was rapidly approved to treat R/R cases and newly diagnosed patients[173]. Other examples using targeted therapies based on genetic alterations include HER2 amplification in breast cancer, *BRAF* mutations in melanoma or *KIT* alterations in gastrointestinal stromal tumors, where their pharmacological inhibition has improved the clinical outcome. Non-small cell lung cancer is a type of cancer with well-characterized driver mutations and several subgroups. Half of the patients with these tumors present a characteristic EGFR mutation that can be targeted with a kinase inhibitor, showing good results compared to normal chemotherapeutic regimes[174].

New technological advances, such as next-generation sequencing, allows the study of genetic alterations in cancer patients. However, precision medicine based on genetic information presents several limitations. One of the most important is the heterogeneous response observed in patients with the same genetic background treated with the same drug. Non-genetic mechanisms of therapy resistance in cancer

cells widely vary even in similar tumors, and epigenetic changes play an important role[175]. In fact, apart from the successful examples mentioned above, several genetic precision medicine initiatives have failed in providing a therapeutic advantage over classical treatment assignment[176,177]. To obtain a deeper understanding of every tumor, other molecular determinations should be applied to complement genetic analyses, such as metabolomics, transcriptomics, epigenetics and proteomics. These requirements make almost impossible to routinely profile every tumor. Despite the great technical improvements developed in the last decade and the extensive repertoire of available drugs, overall only 10% of patients can be treated with an approved inhibitor[178]. Results obtained in different trials that applied genetic-based precision medicine highlight the limitations of this approach. For example, in the NCI-MATCH trial only 38% of patients presented a targetable genetic alteration and only 18% were finally treated with the suggested inhibitor, and most developed resistance to therapy. Moreover, from the treated cohort the maximum overall response rate obtained was 38%[179].

Even with a complete molecular characterization of the tumor, we would only obtain a static time-point information of the sample. Tumors are dynamic and continuously adapt to perturbations, for example, to anticancer treatments. Static molecular information can guide treatment if a vulnerability is identified, but changes in response to treatment conferring resistance are frequent and may include clonal selection, new mutations or activation of secondary pathways, among others. If the selected targeted therapy fails to eliminate the tumor, a new characterization of the tumor should be performed to identify a new therapeutic strategy.

### 1.3.2. Functional precision medicine

As an alternative to analyze the molecular components of dead cancer cells, functional precision medicine (FPM) directly interrogates alive cells with different perturbations (treatments) to identify the best drug candidate. Similarly as antibiograms applied to bacterial infections, that grow and expose them to a library of antimicrobial drugs to identify the most effective one[180], FPM approaches directly test therapies on patient-isolated cells. However, despite promising results, FPM has not been introduced yet in normal clinical practice, mostly because of some technical limitations that are now slowly beginning to change.

#### *1.3.2.1. Cancer models for FPM*

To perform functional assays on patient biopsies, the critical step is to obtain alive primary cancer cells. In hematological malignancies it is relatively easy to obtain enough cells and expose them to a panel of different drugs *ex vivo*. In solid tumors, however, obtaining enough viable cells is more challenging. Patients must undergo through invasive surgery to get enough tumor tissue, and normally the number of viable cells obtained is low, limiting the number of treatments that can be explored. Moreover, primary cancer cells in *ex vivo* conditions rapidly decay, which limits the time window to perform functional assays[181].

Several strategies have been proposed to expand the number of cells obtained from a biopsy. The establishment of cell lines from patient samples has been extensively used, but the process is inefficient, time-consuming and normally the resulting cell line does not fully recapitulate the characteristics from the parental tumor[182]. A more sophisticated technology to grow primary cancer cells is conditional reprogramming, where primary tumor cells are seeded in a fibroblast feeder layer with ROCK inhibitors and enriched media. This combination induces a proliferative state on cancer cells, that has been successfully used, for example, to expand cells from non-small cell lung cancer patients and identify an effective combination using *ex vivo* assays[183]. Although this method is more reliable than the establishment of cell lines, it is necessary to perform long incubations in 2D layers to acquire the necessary number of cells to perform the assay, which increases the chance of inducing alterations.

To avoid these phenotypic changes, some researchers use advanced techniques to grow primary cells in conditions that resemble the native environment. This is the case of organoids, which are generated after inducing a pluripotent stem cell phenotype in cancer cells to grow them in a soft material mimicking the extracellular matrix. This allows expanding cells in a three-dimensional manner maintaining the tumor architecture, which helps to maintain the phenotypic characteristics of the original tumor[184]. In the last years, organoid technologies have greatly advanced, and several biobanks have been established, paving the way to apply this technology for cancer treatment. In fact, several preclinical studies have shown a good correlation between drug candidates' effectiveness in organoids and clinical efficacy in solid tumors[185], and, for example, the FORESEE clinical trial (NCT04450706) aims to use breast cancer patient-derived organoids to perform a drug screening and guide treatment in a clinical setting. Another strategy extensively used is the generation of patient-derived xenografts (PDX). In these models, material from a patient's biopsy is implanted into

immunodeficient mice, that allows the growth of the tumor in a similar environment minimizing clonal selection and phenotypic changes. PDXs are extensively used in research as a validation tool for drug discovery, especially in cancer[186]. However, the use of PDXs to guide cancer treatment and identify the best option, however, is not fully implemented. Some studies have found a good correlation between drug response in PDXs and patients[187], but only in a small subset studies, and there is a limited clinical application for PDX models in FPM[188]. Both approaches, organoids and PDXs, share similar limitations. At present, both are expensive and, more importantly, they require an extensive time to obtain sufficient material to perform any assay (sometimes several months), which limits the clinical utility to guide therapy for cancer patients that cannot wait to receive treatment. Recently, to avoid the delay caused by the time needed to generate these models, PDX and organoids from breast cancer patients were generated at the time of diagnosis and used to perform a drug screening. One of the patients that recurred, was treated with an effective drug identified by these models with excellent results[189]. But this successful example does not change the fact that most patients will not benefit from this approach.

Lastly, other studies directly use the whole tumor to test potential treatments and identify the best option. Using the material obtained from biopsies, some studies explore the use of slices or fragments of the tumor cultured with commercial media and treated with different drugs for viability studies to identify effective treatments. With this strategy, for example, an *ex vivo* platform was able to exquisitely predict treatment efficacy using samples from 55 patients[190]. Alternatively, other researchers have developed devices to apply different treatments directly at the tumor to measure efficacy after short drug exposure. One technology exploiting this idea is the CIVO platform, that performs several microinjections with different drugs directly on tumors to study their efficacy[191]. Recently, this platform was validated in 13 patients with soft tissue sarcoma without showing any important adverse effects[192]. An additional option is a microdevice designed to be implanted inside the tumor with several drug reservoirs that are released in distinct regions of the tumor[193]. The utility of this microdevice is now being studied in a clinical trial for breast cancer patients, but no results have been published yet (NCT02521363). Both techniques have the advantage of maintaining the tumor architecture and microenvironment, but the main limitation is that they must be performed in accessible tumors, limiting their application in a wide range of cancers.

#### *1.3.2.2. Assays to measure drug response*

The endpoint of functional assays used for FPM is measuring drug efficacy. Typically, they use methods that identify changes in cell activity or viability. These include a plethora of techniques, such as cell counting, metabolic activity with MTT or intracellular ATP concentration, different markers to identify proliferation, apoptosis engagement or cell death, among others. All of them aim to determine if the selected treatments induce cytotoxicity on cancer cells, thus they need long incubations with these agents to observe any effect, which can cause an *ex vivo* decay of the sample. Nevertheless, since it is relatively simple to obtain a large number of viable cells from leukemia patients, some functional initiatives using these approaches in liquid tumors achieved very promising results. One example is the use of colorimetric measurements for viability in primary leukemic cells exposed to different kinase inhibitors for 3 days, which accurately correlated with the patients genetic information[194]. These results promoted several phase II clinical trials to guide targeted therapy treatment for AML, ALL and CLL patients, but none of them have presented results supporting the clinical advantage of this technique over classical risk stratification (NCT02779283, NCT01620216, and NCT01441882). Also in AML, another group used a drug sensitivity and resistance testing platform to screen almost 200 drugs, classifying different subgroups of patients based on their drug response profile, and they identified resistance mechanisms with the study of consecutive samples[195]. In a pilot study recently published using this drug sensitivity and resistance testing, 37 relapsed and refractory AML patients were treated based on the results of the assay, obtaining a 59% response rate[196]. Other preclinical studies have assigned treatments based on FPM results, even in solid tumors[197,198], but at the moment they have not progressed to the clinic.

Other initiatives apply different readouts than direct indicators of cytotoxicity. Several studies tracked the activation of specific pathways after exposure to anticancer drugs as indicators of efficacy. Using single-cell network profiling, a technique that uses flow cytometry to study the activation of several intracellular pathways after treatment in less than 24 hours on AML primary samples, the authors found a good correlation with clinical response[199]. Another initiative called pharmacoscopy exposes primary cells to a collection of candidate drugs for 18 hours and, after immunostaining, nuclear morphology is assessed by automated microscopy as a readout for treatment efficacy. The clinical pilot study used on hematological malignancies samples and EXALT successfully showed an increase in overall response and progression-free survival

when treated with the pharmacoscopy-guided drugs, twelve of them being exceptional responders with an increase of progression-free survival three times longer than previous treatments[200,201]. These exceptional results caused the initiation of a follow-up trial to further validate the utility of this functional technique (NCT04470947 or EXALT-2).

A successful functional assay should be performed directly on extracted primary cancer cells to maintain tumor characteristics and with a fast turnover time to avoid cell deterioration. Dynamic BH3 Profiling (DBP) is a functional assay that complies with these requirements and will be further explained in the next section.

### 1.3.3. Dynamic BH3 profiling

BH3 profiling is an assay developed to study apoptotic priming in cells. As already explained in previous sections, the balance between the proapoptotic and antiapoptotic BCL-2 family of proteins determines if a cell is “primed” or “unprimed” for apoptosis. The assay uses synthetic peptides that mimic the BH3 domain of different proapoptotic proteins. Using BIM, BID and PUMA BH3 peptides the overall apoptotic predisposition is evaluated since these peptides block all antiapoptotic proteins and directly activate BAX and BAK (PUMA with lower efficacy). Using peptides mimicking the sensitizer proteins (BAD, NOXA, MS1 or HRK) we can identify addictions to specific antiapoptotic proteins.

In this assay, permeabilized cancer cells are exposed to the different BH3 peptides and induction of MOMP is assessed to determine apoptotic priming (different techniques have been used, such as fluorimetry with JC-1 or flow cytometry using antibodies against cytochrome c). Induction of MOMP at lower concentrations of BIM, BID or PUMA peptides indicates that cells are already primed for apoptosis, while in the case of MOMP induction with sensitizer peptides demonstrate cells dependence on specific antiapoptotic proteins (BCL-2, BCL-xL and BCL-w for BAD peptide, MCL-1 for NOXA and MS1 peptides and BCL-xL for HRK peptide). Importantly, patient cancer cells that present a higher apoptotic priming respond better to chemotherapy in the clinic[202]. The correlation between apoptotic priming and treatment efficacy has been validated in AML[203], CLL[204] and neuroblastoma[205]. Moreover, using sensitizer peptides dependencies on specific antiapoptotic proteins were described in leukemia[206] and lymphoma[207].

DBP emerged as a functional predictive assay for therapy response that was based on BH3 profiling. Most anticancer therapies induce apoptotic cell death, therefore cells

treated with an effective drug will proapoptotic changes in the BCL-2 family of proteins and become “primed for apoptosis”. In DBP, treated cells are permeabilized and exposed to different concentrations of the BIM peptide to induce MOMP, and cytochrome c release is then detected using a specific labelled antibody. While BH3 profiling measures the apoptotic predisposition or priming of a given sample, in DBP cancer cells are treated with different anticancer drugs (normally around 16 and 40 hours) to detect dynamic changes in priming. By comparing untreated with treated cells, we can determine if an increase in apoptotic priming occurs (less concentration of BIM peptide needed to induce MOMP), indicating later cytotoxicity induced by the treatment (Figure 6)[208]. Moreover, by comparing the increase in priming in control and treated cells after incubation with sensitizer peptides (BAD, HRK or MS1), DBP can identify antiapoptotic adaptations caused by the treatment. This assay presents some critical advantages for FPM compared to other approaches:

1) DBP can be performed in less than 24 hours. This allows the direct interrogation of primary patient samples and avoids *ex vivo* cellular deterioration caused by long culture periods. In addition, results are rapidly obtained which allows a fast adaptation of the treatment and a continuous follow-up to maximize treatment efficacy in patients.

2) This assay is very versatile. It can be used to prospectively identify treatments in the clinic, but also to screen drugs and find new treatments in multiple models (cell lines, PDXs or primary samples).

3) The identification of antiapoptotic adaptations using sensitizer peptides is a powerful asset to guide the use of BH3 mimetics to pharmacologically exploit antiapoptotic adaptations caused by a chemotherapeutic or targeted agents. In fact, it has been demonstrated in several types of cancer, that specific combinations with BH3 mimetics synergistically kill cells by enhancing cytotoxicity.

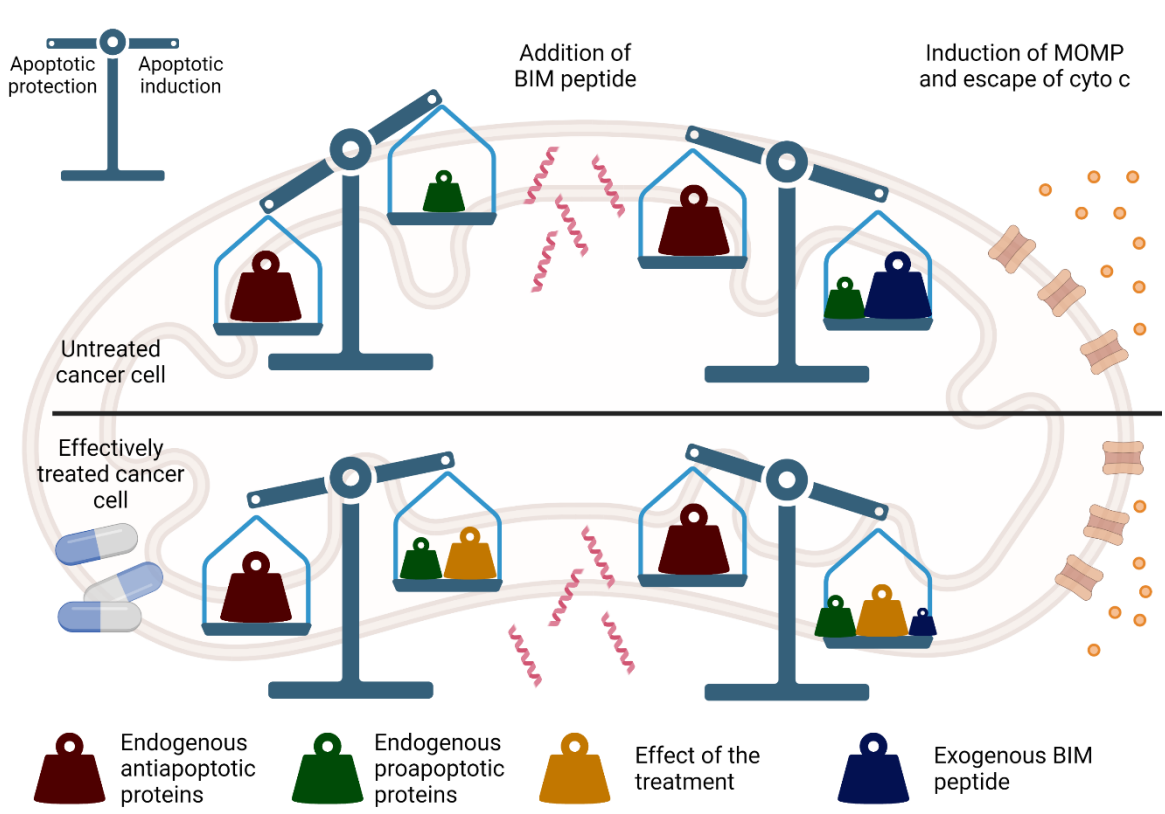


**Figure 6. Graphical explanation of the rationale behind dynamic BH3 profiling.** In untreated cancer cells, exposure of BIM peptide induce the start of the apoptotic process marked by the escape of cytohrome c from inside the mitochondria. If cells have been effectively treated, the drug will induce a change in the apoptotic priming and less BIM peptide will be necessary to start the apoptotic process. Created with BioRender.

DBP has been extensively performed in a plethora of cancer types, which are summarized in Table 2. Most studies that apply DBP are focused on the identification of effective treatments using cell lines, PDXs or patient samples. Yet, several studies also explore the identification of antiapoptotic adaptations that can be overcome with BH3 mimetics.

| Type of tumor | Type of samples | Synergy with BH3 mimetics? | Reference |
|---|---|---|---|
| Several | Cell lines, mouse model and patient samples | No | Montero et al. Cell 2015[208] |
| Breast cancer | Cell lines and PDX | No | Brasó-Maristany et al. Nature Medicine 2016[209] |

| | | | |
|---|---|---|---|
| AML | Cell lines and patient samples | Yes | Pallis et al. Oncotarget 2017[210] |
| Blastic plasmacytoid dendritic cell neoplasm | Cell lines, PDXs and patient samples | Yes | Montero et al. Cancer Discovery 2017[211] |
| CLL | Patient samples | Yes | Deng et al. Leukemia 2017[212] |
| Biphenotypic B-myelomonocytic leukemia | Cell lines | Yes | Grundy et al. PLOS ONE 2018[213] |
| AML | Cell lines | No | Grundy et al. PLOS ONE 2018[214] |
| Different blood cancers | Cell lines and patient samples | Yes | Lee et al. Science Translational Medicine 2018[215] |
| AML | Patient samples | No | Garcia et al. Blood 2018[216] |
| Diffuse large B-cell lymphoma | Cell lines and patient samples | Yes | de Jong et al. International Journal of Molecular Sciences 2019[217] |
| Breast cancer | Patient samples | Yes | Walsh et al. Clinical Cancer Research 2019[218] |
| Melanoma | Cell lines, PDX and patient samples | No | Montero et al. Nature Communications 2019[219] |
| AML | PDX and patient samples | Yes | Bhatt et al. Cancer Cell 2020[220] |

| | | | |
|---|---|---|---|
| Rhabdomyosarcoma | Cell lines and PDX | Yes | Alcon et al. Cell Death & Disease 2020[221] |
| AML | Patient samples | No | Garcia et al. American Journal of Hematology[222] |
| Breast cancer | PDX | Yes | Zoeller et al. Breast Cancer Research 2020[223] |
| Esophageal adenocarcinoma and malignant pleural mesotherlioma | Cell lines and patient samples | Yes | Surman et al. Molecular Cancer Therapeutics 2021[224] |
| Thymoma and thymic carcinoma | Cell lines and patient samples | Yes | Müller et al. BMC Medicine 2021[225] |
| Breast cancer | Cell lines | Yes | Alcon et al. Cells 2021[226] |
| Breast cancer | Cell lines | No | Karakas et al. Cell Death Discovery 2021[227] |
| Diffuse large B-cell lymphoma | Cell line and PDX | No | Rys et al. Cancers (Basel) 2021[228] |
| Several | Cell lines | No | Montinaro et al. Cell Death & Differentation 2021[229] |
| BCP-ALL | Cell lines and PDX | Yes | Seyfried et al. Leukemia 2022[165] |

**Table 2.** Table with the published studies that use dynamic BH3 profiling to identify effective treatments against different types of cancer.

Recently, a new version of DBP has been developed, called high-throughput DBP (HT-DBP). Using the same rationale, this new technology exploits 384 well plates and automatic platers to treat a small number of cells with hundreds of different compounds. MOMP Induction is assessed using high-throughput microscopy tracking of cytochrome c retained inside the mitochondria. By screening different drug libraries HT-DBP has demonstrated an predictive capacity for effective anticancer drugs in cell lines, PDX and primary samples from colon cancer[230], non-small cell lung cancer[231] and breast cancer[232].

Despite the promising results obtained with the different DBP platforms, this technique has not been implemented for FPM. Some of these studies use DBP on patient samples to identify effective treatments, and in certain cases obtaining good clinical results based on its predictions. The most advanced studies use hematological patient samples to assess the increase in apoptotic priming after *ex vivo* treatment to evaluate overall response retrospectively, obtaining a good correlation between DBP predictions and clinical efficacy[222]. The inclusion of DBP as a prospective routine technique for clinical decisions encounters the same problems as other FPM initiatives. First, biopsies are not normally performed prior to treatment and when they are clinicians prioritize fixation or freezing the samples to perform molecular analyses. Moreover, to use any FPM assay prospectively, first they will have to get validated in clinical trials and then approved by regulatory agencies. At the date of this thesis deposition, there are no clinical trials evaluating the utility of DBP to prospectively guide cancer treatment, despite its excellent predictive capacity in preclinical studies.

### 1.3.4. Microfluidics in cancer

Microfluidic technologies use small volumes of fluids for different objectives. In recent years, this concept has been extensively developed and applied to different areas such as physical science, chemistry, biology or medicine. One of the main uses for microfluidics is lab-on-a-chip (LOC) approaches, devices that perform laboratory techniques using small chips with microchannels that control fluidics (techniques that include dilution, the addition of different reagents, separation, reaction and detection). LOC present several advantages compared to standard laboratory analyses, such as automatization or reduction of reagent requirements.

When designing LOCs, different microfluidic components can be used to obtain a device that accomplishes the desired characteristics. These include microchannels, microneedles, reactors, separators, filters, mixers, micropumps, microvalves, wells or

3D structures[233]. Since all these structures are miniaturized inside a chip, LOC development exploits microfabrication techniques such as photolithography, wet etching, soft lithography, hot embossing, laser ablation or 3D printing to directly generate the LOC (or generate a master to produce the final LOC by replica molding). Different materials have been used to develop LOC, including glass, quartz and organic plastic silicon. Polydimethylsiloxane (PDMS) has been extensively used as the main material to develop LOC, especially for its biological characteristics. PDMS allows a fast and cheap prototype development of LOC devices, by replicating a molding on a master with the desired microfluidic design. Moreover, PDMS is transparent which allows microscopy analyses, it is bio-compatible, it is gas-permeable and, using plasma, it can be activated to perform irreversible bounds between different PDMS layers or on glass[234].

A full review on microfluidics, including the physics behind the manipulation of small volumes of fluids and the different applications where it has been used, is beyond the scope of this introduction. However, we will introduce how LOC has improved basic cancer research, with a special focus on devices for drug screening and FPM applications.

#### *1.3.4.1. LOC in basic cancer research*

As previously discussed, there is a growing interest in developing patient-derived cancer models replicating the original tumor. Microfluidics and LOCs have been recently used to solve different limitations observed in the generation of these models, including 3D cultures with hydrogels, or the formation of tumor spheroids or organoids. Several microfluidic devices have been designed to automatize and increase the throughput of these cancer models, making the overall process easier, cheaper, and versatile. This includes devices that retain spheroids in wells to perform different assays, microfluidic chips to seed cancer cells in hydrogels or the development of LOCs to generate patient-derived organoids[235,236]. One of the advantages of microfluidic devices is the ability to co-culture different cell types. This allows the generation of models that more accurately represent the original tumor, for example with the addition of different cells to mimic the tumor microenvironment, the microvasculature[237] or certain aspects of the immune system[238] with cellular cross-talk.

Other biological applications where microfluidics have been extremely useful is organ-on-a-chip devices. These models that mimic the physiological characteristics of a specific organ are useful to study many biological processes and diseases, but they

have been also applied to study key processes involved in cancer. Microfluidic devices that study cancer growth use co-culture systems to study the effect of different types of cells that are normally present in the tumor and can induce an increased growth rate; for example fibroblasts in breast cancer[239], or epithelial and endothelial cells in non-small cell lung cancer[240]. LOCs that recreate blood vessels have been also used in cancer research to study angiogenesis, the formation of new vessels that irrigate tumors, showing that the presence of renal cell carcinoma induces the outgrowth of endothelial cells[241]. Another process extensively studied in cancer is cell migration and invasion, related to the epithelial to mesenchymal transition (EMT). Microfluidic devices have assisted on bringing new insights into this process, for example, by inducing EMT with fibroblasts or continuous flow conditions[242,243], or the increase in migration when cancer cells are exposed to fibroblasts or macrophages[244,245]. Invasive cells can reach the blood system to extravasate and generate metastasis in a new organ. For instance, chips that recreate blood vessels were used to study intravasation and extravasation, and describe the key role of β1 integrin in this process[246,247]. These are just a few examples on how microfluidic devices have helped to better understand critical processes in cancer progression.

LOCs are also being used in cancer as diagnostic tools. Circulating tumor cells (CTC), cancer-derived exosomes, circulating tumor DNA and non-coding RNA can be found in the bloodstream of cancer patients and have been explored as prognostic factors. However, their isolation is challenging due to several factors, such as size and abundance in the blood. In this sense, microfluidics have been used to improve the isolation of tumor-related material, especially for CTCs. There are some available commercial kits to isolate CTCs based on EpCAM expression and microfluidics, for example using microposts or the herringbone-chip[248,249]. Other strategies have been implemented beyond antigen-based separation exploiting particular cancer cells characteristics; for example, separation by size, shape, electrical impedance or even pH[250–253]. Some LOCs have been also developed to isolate exosomes derived from tumors using immunoaffinity, filters or lateral displacement[254]; and circulating DNA (ctDNA) and RNA[255,256]. One of the main advantages of these microfluidic devices is that most of them allow sample recovery after separation. This expands the utility of these techniques from detection of cancer material in blood to diagnostic tool to using this material for several other purposes, such as functional assays with CTCs or genetic screenings based on isolated ctDNA.

#### *1.3.4.2. Drug screening and FPM with microfluidics*

The development of organ-on-a-chip devices that include tumor cells has not only been used to study fundamental cancer processes but also to test the effect of different drugs in cancer progression and invasiveness. Studies with multiple microfluidic devices helped to understand the effect stromal cells on cancer cells' resistance to treatment[257,258], the blood-brain barrier[259], extravasation[260] or to guide the use of immunotherapy[261]. The multiple advantages of microfluidics allow their use to study new processes that were previously impossible to tackle with traditional culture conditions.

The ability of LOCs to perform assays with small volumes of reagents and their high-throughput capacities align with FPM initiatives, which include the necessity to perform drug screening assays with a low number of primary cells and a rapid turnover to avoid *ex vivo* deterioration. Several studies have used microfluidic chips to automatically generate a large number of spheroids, immobilize them in fixed positions inside a chip and apply different treatments to study cytotoxicity. This has the advantage to directly test drugs in 3D cancer cell cultures which better resembles the native organization compared to 2D, as demonstrated in breast[262] and colon[263] cancer cell lines. However, only some preliminary studies have been published using similar technologies with primary patient spheroids[264–266], which emphasizes the need for further FPM development.

Nevertheless, different laboratories have directly used whole tumors to perform drug screenings using two main strategies. The first one consists in performing microdissections of the tumor to obtain slices, that are then trapped in a microfluidic chip with different wells to protect them from shear stress. Using this strategy, tumors from different PDXs and even patient biopsies have been used to try the efficacy of different anticancer drugs as a proof-of-concept[267,268]. The other approach consists of devices that permit the culture of tumor slices and the application of anticancer treatments to different regions of the slice to study cytotoxicity. Several studies showed a good identification of cytotoxic agents, in PDXs and patient tumors[269–271]. However, the number of drugs screened has been very limited and results are still preliminary.

Droplet microfluidics allow encapsulation of different components between immiscible oil phases, where every droplet works as a small reactor for the desired assay. With this technology, a very small number of cells can be retained in a droplet and treated with different drugs, increasing the number of treatments that can be tested in a solid

tumor biopsy. In fact, different studies used droplet microfluidics for cytotoxicity screenings on primary cells from brain[272], nasopharyngeal[273] and CLL[274] cancer patients. More recently, thanks to the use of a sophisticated piezoelectric Braille valve system, a new microfluidic system generated droplets with around 100 primary cancer cells testing 56 different combinations of treatments. Importantly, every droplet condition was successfully identified using a fluorescent droplet barcode. Furthermore, the readout was cleaved caspase-3, which allowed to perform the assay in less than 24 hours[275]. This last example shows the potential of using microfluidics in FPM assays, to generate new platforms and screen a large number of treatments with a limited number of cells from a biopsy, by shortening incubation times to avoid *ex vivo* deterioration.

Using a completely different approach, the Manalis' lab developed a microfluidic device with a resonator to precisely weight cellular masses with high sensitivity to small differences[276] and perform high-throughput measurements of changes over time on cell growth[277]. This led to the identification of mass changes when cancer cells were effectively treated after short incubations with drugs[278]. With this platform that combines high-throughput analyses, short incubations with anticancer drugs and a readout that identifies treatment-related cytotoxicity, they could detect treatment efficacy directly on primary cells from multiple myeloma and glioblastoma patients with a good correlation with the clinical data, demonstrating the predictive power of this assay[279,280].

As discussed, microfluidic devices can improve and simplify FPM initiatives and present different advantages, like the ability to perform high-throughput assays or the automatization of complicated analyses to be extensively applied in the clinic. However, none of the devices explained above have been yet validated in a clinical trial setting to demonstrate their utility on improving patients' treatment for FPM implementation.

# Chapter II

## Aims of the thesis

This thesis has two distinct main objectives to identify effective treatments in different types of cancer.

In the first section, DBP is used to guide treatment for pediatric patients with BCP-ALL, especially in R/R cases. To achieve that, different subobjectives have been established:

I. Validation of DBP in pediatric BCP-ALL cell lines and murine models to identify effective chemotherapy and targeted therapies.
II. Identification of antiapoptotic adaptations after anticancer treatment to guide the use of BH3 mimetics to overcome resistance mechanisms.
III. Guide treatment for R/R pediatric leukemia patients using DBP in primary samples.

In the second section, we use microfluidics to improve some limiting aspects of the DBP assay:

IV. Development of a microfluidic platform to perform the DBP assay reducing the cell number requirement.
V. Compare results obtained with the microfluidic-based DBP with the standard DBP in cell lines and primary samples to validate this new platform.

# Chapter III

## Materials and methods

## 3.1. Cell lines

BCP-ALL cell lines (NALM-6 and SEM) were provided by Prof. Pablo Menéndez from the Josep Carreras Leukaemia Research Institute. These cells were maintained in RMPI 1640 medium (31870, Thermo Fisher) with 10% of heat-inactivated fetal bovine serum (FBS) (10270, Thermo Fisher), 1% of L-glutamine (25030, Thermo Fisher) and 1% of penicillin/streptomycin (15140, Thermo Fisher). In the case of gastrointestinal stromal tumors (GIST) cell lines (GIST-T1 and GIST-T1/670), cells were provided by Dr. César Serrano from the Vall d'Hebron Institute of Oncology and maintained in IMDM medium (12440, Thermo Fisher) supplemented with 15% of heat-inactivated FBS, 1% of L-glutamine and 1% of penicillin/streptomycin. In the case of the GIST-T1/670, cells were cultured in the presence of 200 nM of imatinib for selective pressure. All cells were maintained inside a humidified Galaxy 170 S incubator (New Brunswick) at 37ºC and 5% of $CO_2$.

## 3.2. Drugs and treatments

All drugs used are summarized alphabetically in Table 3. L-asparaginase was resuspended in sterile MiliQ water, all the other drugs were resuspended in dimethyl sulfoxide (DMSO) (D8418, Sigma Aldrich) to a stock concentration. Working solutions were obtained by further dilution with the appropriate solvent.

| Drug | Target | Supplier |
|---|---|---|
| A-1331852 (or A133) | BCL-xL inhibitor | MedChemExpress |
| ABT-199/Venetoclax | BCL-2 inhibitor | MedChemExpress |
| Bortezomib | 20S proteasome inhibitor | MedChemExpress |
| Clofarabine | DNA polymerase inhibitor | SellekChem |
| Cyclophosphamide | DNA cross linker | MedChemExpress |
| Cytarabine | DNA synthesis inhibitor | SellekChem |
| Dactolisib | PI3K and mTOR inhibitor | LC Laboratories |

| | | |
|---|---|---|
| Dasatinib | Multitargeted inhibitor | SellekChem |
| Daunorubicin | Topoisomerase II inhibitor | SellekChem |
| Decitabine | DNA methyltransferase inhibitor | SellekChem |
| Dexamethasone | Glucocorticoid | SellekChem |
| Doxorubicin | Topoisomerase II inhibitor | LC Laboratories |
| Etoposide | Topoisomerase II inhibitor | MedChemExpress |
| Fludarabine | STAT1 inhibitor | SellekChem |
| Gefitinib | EGFR inhibitor | LC Laboratories |
| Hydrocortisone | Glucocorticoid | SellekChem |
| Ibrutinib | BTK inhibitor | SellekChem |
| Idarubicin | Topoisomerase II inhibitor | MedChemExpress |
| Imatinib | Multitargeted inhibitor | LC Laboratories |
| L-asparaginase | Enzyme | BioVision |
| Methotrexate | DHFR inhibitor | SellekChem |
| Mitoxantrone | Topoisomerase II inhibitor | SellekChem |
| Ponatinib | Multi-targeted inhibitor | MedChemExpress |
| Prednisone | Glucocorticoid | SellekChem |
| Quizartinib | FLT3 inhibitor | SellekChem |

| | | |
|---|---|---|
| Ripretinib | c-Kit and PDGFRα inhibitor | SellekChem |
| Ruxolitinib | JAK1/2 inhibitor | SellekChem |
| S63845 | MCL-1 inhibitor | MedChemExpress |
| Sorafenib | Multi-targeted inhibitor | MedChemExpress |
| Sunitinib | Multi-targeted inhibitor | SellekChem |
| Thioguanine | DNMT1 inhibitor | SellekChem |
| Topotecan | DNA topoisomerases inhibitor | SellekChem |
| Trametinib | MEK1/2 inhibitor | SellekChem |
| Vincristine | Microtubule formation inhibitor | LC Laboratories |
| Vorinostat | HDAC inhibitor | SellekChem |

**Table 3**. Summary table of the drugs used in this thesis, indicating their main target and the supplier.

## 3.3. FACS-based dynamic BH3 profiling

DBP protocol was previously described by Ryan and collegues[281] at the Letai laboratory at Dana-Farber Cancer Institute. Between 300,000 and 500,000 cells per condition were seeded in 12-well plates and then treated with the desired anticancer drugs for a given time (normally between 16 and 40 hours). After incubation with the drugs, cells were collected in different tubes, in the case of non-adherent cells by directly pipetting; while in the case of adherent cells by first collecting the media and then trypsinizing them, then adding the cells in trypsin to the same tube of the media. Since the complete media is rich in proteins, the trypsin added gets inactivated. After

spinning down, cells were stained using the viability marker Zombie Violet (423113, BioLegend) for 10 minutes at room temperature, washed with PBS and then resuspended in 330 µL of MEB buffer (150 nM mannitol, 10 mM HEPES-KOH pH 7.5, 150 mM KCl, 1 mM EGTA, 1 mM EDTA, 0.1% BSA and 5 mM succinate).

In parallel, different peptide solutions were prepared using MEB buffer with 0.002% of digitonin (D141, Sigma-Aldrich). These solutions were prepared at a 2X of the final concentration as specified below, since the same volume of the cell solution and the peptide solution were mixed:

- BIM BH3 peptide (AC-MRPEIWIAQELRRIGDEFNA-NH2): 10, 3, 1, 0.3, 0.1, 0.03 and 0.01 µM.
- BAD BH3 peptide (AC-LWAAQRYGRELRRMSDEFEGSFKGL-NH2): 10, 1 and 0.1 µM.
- HRK BH3 peptide (AC-SSAAQLTAARLKALGDELHQY-NH2): 100 µM.
- MS1 BH3 peptide (AC-RPEIWMTQGLRRLGDEINAYYAR-NH2): 10 µM.
- Positive control of alamethicin (BML-A150-0005, Enzo Life Sciences): 25 µM.
- Negative control of DMSO: Maximum volume of DMSO used in the previous conditions.

In a 96-well plate (3795, Corning), 25 µL of each peptide solution was added to all the wells in the same column of the plate. Then, 25 µL of each cell solution was added to every well of a row in the plate, exposing every anticancer treatment condition (plus the untreated cells) to every peptide condition. Plates were incubated for 1 hour at room temperature, followed by fixation for 15 minutes with 25 µL of an 8% formaldehyde solution, then neutralized for 10 minutes with 50 µL of N2 buffer (1.7 M tris base, 1.25 M glycine at pH 9.1) and stained overnight at 4 ºC with 25 µL of 1:1,000 of anti-cytochrome c antibody (Alexa Fluor® 647 anti-Cytochrome c—6H2.B4, 612310, BioLegend) in intracellular staining buffer (1% Tween20, 5% BSA in PBS). The following day, results were analyzed using a Sony SA3800 flow cytometer (SONY) or a BD LSRII flow cytometer (BD Biosciences) and processed with FlowJo software to quantify cytochrome c release (%priming). Δ%priming stands for the difference of %priming (or % of cytochrome c released) between non-treated cells and treated cells for every peptide.

For PDX or primary patient samples, cells were also stained with fluorescent antibodies to label the desired cancer cell population. For ALL samples, 1:2,000 of Alexa Fluor® 488 anti-human CD45 antibody (368536, BioLegend) and PE anti-human CD19

antibody (392506, BioLegend) were used. In GIST samples, 1:100 of anti-cKIT Alexa Fluor 647 antibody (sc13508, Santa Cruz Biotechnology) was used to identify cancer cells. All antibodies were diluted in HBSS buffer with 2% of FBS and incubated for 30 minutes in ice.

## 3.4. Cell death assay

50,000 cells were seeded in a 12-well plate and treated with different anticancer treatments for the specified time. In experiments where a BH3 mimetic was used in combination, the appropriate concentration of the drug was added at the time point detailed in every experiment. After treatment, cells were collected in different tubes, either by directly pipetting for non-adherent cells or after trypsinization for adherent cells, as described in 3.3. After spinning down, cells were resuspended in 250 µL of staining buffer (100 mM HEPES free acid, 40 mM KCl, 1.4 M NaCl, 7.5 mM MgCl2 and 25 mM CaCl2 at pH 7.4) with 1:2,000 of Alexa Fluor 647® conjugated Annexin V (640912, BioLegend) and 1:2,000 of DAPI (62248, Thermo Fisher). Finally, cells were analyzed using a Gallios flow cytometer (Beckman Coulter) and FlowJo software to quantify viable cells (Annexin V and DAPI negative events). Results were represented as the mean of %cell death (100-%viable cells).

## 3.5. Protein extraction

For liquid tumors, 2 million cells were seeded in 6-well plates and treated with the corresponding drugs for the established time of each experiment. After incubation, cells were spinned down and washed with PBS, followed by resuspension in 300 µL of RIPA buffer (150 mM NaCl, 5 mM EDTA, 50 mM Tris–HCl pH = 8, 1% Triton X-100, 0.1% SDS and EDTA-free Protease Inhibitor Cocktail (4693159001, Roche)). After an incubation of 30 minutes on ice and constant agitation, tubes were centrifuged at 4 ºC for 10 minutes at 16,000 g. The supernatant was collected in a new tube and the amount of extracted protein quantified with the PierceTM BCA Protein Assay Kit (23227, Thermo Fisher) and stored at −20°C.

## 3.6. Immunoprecipitations

To obtain protein for the immunoprecipitations (IP) the same protocol for protein extraction was used but changing the RIPA buffer for IP lysis buffer (150 mM NaCl, 10 mM HEPES, 2 mM EDTA, 1% Triton X-100, 1.5 mM MgCl2, 10% glycerol and EDTA-free Protease Inhibitor Cocktail (4693159001, Roche)). To immunoprecipitate the

desired protein, 5 µg of antibody against that protein was conjugated to magnetic beads (161-4021, Bio-Rad), that were previously cleaned with PBS-T (PBS with 0.1% of Tween 20), followed by incubating the beads and the antibody for 2 hours at room temperature with constant rotation. Control with 5 µg of rabbit-IgG antibody (CST2729, Cell Signaling) was also performed to ensure proper precipitation of the desired protein. After washing with PBS-T, an equivalent amount of protein extracts were added to the conjugated beads and were incubated overnight at 4 ºC with constant rotation. The following day, the unbound fraction was separated and stored at -20 ºC and the beads were washed again with PBS-T and resuspended in 40 µL of 4X Laemmli buffer. To separate proteins from the conjugated beads, tubes were incubated at 70 ºC for 10 minutes and the eluent was transferred to a new tube that was stored at -20 ºC.

## 3.7. Immunoblotting

Protein samples were prepared to have a final volume of 20 µL by mixing an equal amount of protein extract diluted with MiliQ water and 6,67 µL of 3X Laemmli buffer (6% SDS, 15% 2-mercaptoethanol, 30% glycerol, 0.006% bromophenol blue and 0.125 M tris-HCl). Tubes were then heated at 96 ºC for 10 minutes to denaturalize the proteins. Then, samples were loaded in an SDS-PAGE gel (456-1025, Bio-Rad) submerged in running buffer (tris base 25 mM, glycine 250 mM and SDS 0.8%) and electrically separated for 2 hours (first at 50 V until exiting the stacking gel, where was increased to 80 V). The sandwich was constructed by intercalating a sponge, filter paper, a PVDF membrane (10600023, Amersham Hybond) activated in methanol, the SDS-PAGE gel, filter paper and another sponge, submerged in cold transfer buffer (tris base 25 mM, glycine 250mM and 20% methanol) and placed in a cold chamber for 3 hours at 50-60V. To ensure that protein was properly transferred to the membrane, Ponceau S staining (1% acetic acid and 0.1% Ponceau S) was performed.

The membrane was sequentially washed twice with constant agitation for 5 minutes with TBS (tris base 0.1M and 150 nM of NaCl) and twice with TBS-T (TBS with 0.1% of Tween 20). Next, the membrane was blocked for 1 hour in 50 mL of TBS-T with 2.5 g of fat-free powdered milk and washed three times with TBS-T. This was followed by overnight incubation in a cold chamber with the desired primary antibody (Table 4) diluted 1:1,000 in TBS-T, washed three times with TBS-T and then incubated for 1 hour at RT with 1:3,000 dilution of the anti-rabbit IgG HRP-linked secondary antibody (CST7074, Cell Signaling). Three more washes were performed with TBS-T before developing the membrane using Clarity ECL Western substrate (1705060, Bio-Rad) in

a LAS4000 imager (GE Healthcare Bio-Sciences AB). Bands were quantified using ImageJ software to measure the integrated optical density and normalized to the actin levels as a control protein.

| Antibody | Reference |
|---|---|
| Rabbit anti-BCL-2 | CST4223, Cell Signaling |
| Rabbit anti-BCL-xL | CST2764, Cell Signaling |
| Rabbit anti-MCL-1 | CST5453, Cell Signaling |
| Rabbit anti-BIM | CST2933, Cell Signaling |
| Rabbit anti-BAX | CST2772, Cell signaling |
| Rabbit anti-BAK | CST12105, Cell signaling |
| Rabbit anti-phospho ERK1/2 | CST4370, Cell signaling |
| Rabbit anti-phospho BIM | CST4585, Cell signaling |
| Rabbit anti-actin | CST4970, Cell Signaling |

**Table 4**. Table with the antibodies used in the immunoblotting and immunoprecipitations.

## 3.8. BCP-ALL PDX model generation

BCP-ALL PDXs were generated at the University of Ülm by Dr. Felix Seyfried, Prof. Klaus-Michael Debatin and Prof. Lüder H. Meyer laboratory following previously described protocols[282]. Briefly, primary BCP-ALL cells were obtained from a blood sample of a patient, and xenografts were established by intravenous injection of the patient's cells into female NOD/SCID mice (NOD.CB17-Prkdcscid, Charles River). All extractions were done after informed written consent from the legal guardians and following the institution's ethical review board. Animal experiments were approved by the appropriate authority (Tierversuch Nr. 1260, Regierungspräsidium Tübingen).

## 3.9. Peripheral blood mononuclear cells isolation

Peripheral blood mononuclear cells (PBMC) containing the leukemic cells was isolated from the other components of the blood. The patient sample was first diluted by adding the same volume of PBS + FBS 2%. In a new 50 mL tube, we placed 5 to 10 mL of Ficoll followed by 10 to 20 mL of the diluted sample added drop by drop on top of the Ficoll. The tube was then spinned down at 400-500 g for 30 minutes without acceleration or break in the centrifuge. After this centrifugation, PBMCs that accumulated in the interphase were carefully aspirated and transferred to a new tube. The PBMC fraction was then washed twice with 10 to 30 mL of PBS with 2% FBS and spinned down at 400-500 g for 10 minutes. Cells were then counted and seeded to perform the assay, or resuspended in FBS with 10% of DMSO and cryopreserved.

## 3.10. Microfluidic chip design and computational simulation

The microfluidic chip was designed in collaboration with the Biosensors for Bioengineering group at the IBEC with Dr. Jose Yeste, Dr. María Alejandra Ortega and Prof. Javier Ramón. The microfluidic chip is based on a previously published three-shape network to generate a gradient of dilutions[283]. Microfluidic channels of 100 µm x 100 µm form three stages that generate new solutions by combining two from the previous stage. Finally, the five different microfluidic channels (transporting 5 different concentrations) end in a 3 x 5 array of independently connected to cell chambers (4 mm diameter, 3 mm height and 37 µL volume each) with an outlet for every chamber (Figure 7).

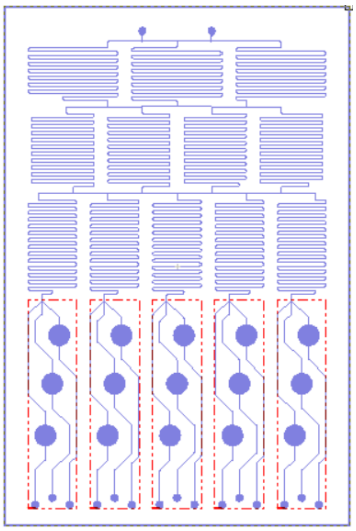

**Figure 7**. AutoCAD design of the microfluidic chip.

Using COMSOL Multiphysics software (version 5.4) we tracked the molecular concentration and flow inside the cell chambers. Using a mesh of $5.8x10^6$ elements a three-dimensional model of the microfluidic chip was simulated by combining laminar flow and transport of diluted species models in a stationary study. The following parameters were selected in order to represent the experimental conditions: i) inlet pressure of 200 mbar; ii) outlet pressure of 0 mbar; iii) diffusion coefficient of 2.93x10-10 $m^2/s$—numerically calculated using the molecular weight of the BIM peptide, MW = 2,486 g/mol; vi) concentration of 1 µM in one of the inlet ports; and v) fluid media with physical properties of water at room temperature. To analyze the fluid performance inside the cell chambers a time-dependent 3D simulation was done considering only the geometry of the cell chamber and a flow rate of 9 µL/min. Pressure and flow rate were experimentally determined to be related by the following equation: $Q=0.045 \times P$, where P is the pressure at the inlets in units of mbar, and Q is the flow rate at every outlet in units of µL/min.

## 3.11. SU8 mold fabrication

To fabricate the microfluidic chip master, standard one-layer soft lithography was used, which was able to generate motifs of at least 100 µm (Figure 8). In a clean room, a silicon wafer (4'' n-type <100>, MicroChemicals GmbH) was cleaned in a PCD-002-CE Plasma Cleaner (Harrick Plasma) for 20 minutes at 6.8 W and heated in a hot plate at 95ºC for 5 minutes. To generate the motifs over the wafer, a negative SU-8 photoresist (2100, MicroChem Lab) was spin-coated over the wafer (first at 500 rpm for 5 seconds with an acceleration of 100 rpm/s followed by 3,000 rpm for 30 seconds with an acceleration of 300 rpm/s) obtaining a 100 µm thick layer. The wafer was softly heated at 65 ºC for 5 minutes and then at 95 ºC for 20 minutes to achieve solvent evaporation. The patterning with the microfluidic chip design was obtained by energy radiation of 240 mJ/cm2 using a negative photoresist mask printed in high-quality acetate film. This was followed by cross-linking of the irradiated parts by exposing the wafer to 65 ºC for 5 minutes and 95 ºC for 10 minutes on a hot plate. Then, the labile SU-8 photoresist was removed by immersion in SU-8 developer (Y020100, MicroChem Lab) for 10 minutes and washed with 2-propanol to stop the process. Finally, the wafer was placed on a hot plate at 150 ºC for 60 minutes with a final decrease until reaching room temperature, when they were silanized to obtain a hydrophobic surface to generate PDMS replicas.

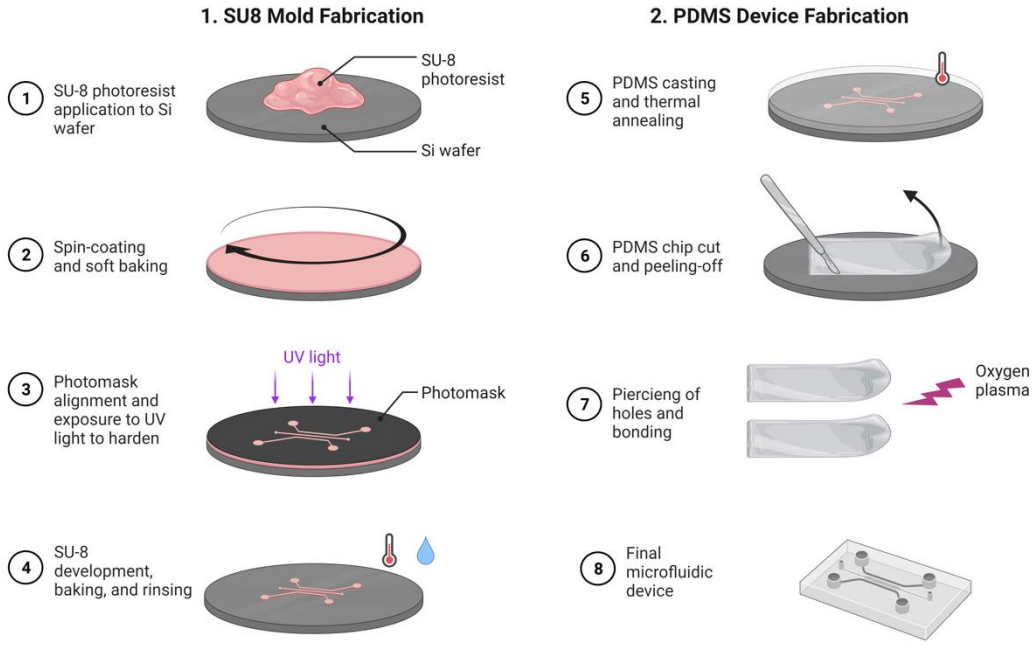


**Figure 8**. Graphical protocol of the fabrication of a silicon mold with SU8 resin and the replica molding process to generate a PDMS microfluidic chip. Adapted from "PDMS Microfluidic Chip Fabrication", by BioRender.com (2022). Retrieved from https://app.biorender.com/biorender-templates

## 3.12. Fabrication of the microfluidic chip

The microfluidic chip was composed of three distinct layers made by mixing Sylgard 184 PDMS (Dow corning) prepolymer with curing agent in a ratio 1:10 followed by degasification for 1 hour:

1) A thin layer of PDMS on top of a clean 75 x 50 mm glass slide (CLS294775X50, Sigma-Aldrich) was obtained by pressing the glass slide against the uncured polymer mix.
2) A 1 mm thick layer without any motifs was obtained by dispensing the prepolymer directly into an empty Petri dish.
3) A 2 mm with the microfluidic chip design was obtained by pouring the prepolymer over the SU8 master mold fixed inside a Petri dish.

All PDMS layers were cured overnight at room temperature on a flat surface and then heated at 85 ºC for 4 hours. Once cured, layers were carefully peeled off and holes for the inlets and the outlets were made into the 2 mm layer using a 0,5 mm multi-purpose sampling tool puncher (Harris Uni-Core). In a clean room, the 1 mm and 2 mm layers were cleaned using water with soap, water and ethanol before being irreversibly bound

by plasma activation in the plasma cleaner at a constant oxygen pressure of 25 bar and power of 10,5 watts for 30 seconds. To stabilize the covalent bonds between the two layers, they were heated at 85 ºC for 4 hours before punching the cell chambers using a 4 mm multi-purpose sampling tool puncher (Harris Uni-Core). Again, the new 3 mm PDMS layer and the glass slide with a thin PDMS layer were cleaned and activated in the plasma cleaner to be irreversible bound, followed by 4 hours at 85 ºC to finally obtain the microfluidic chip.

## 3.13. Microfluidic-generated gradient characterization

To experimentally demonstrate that the gradient generator worked as intended, a gradient characterization was performed by measuring both color absorbance and protein concentration. A solution containing 10 mg/mL of BSA (A3059, Sigma-Aldrich) and 10 µL/mL of blue food dye (Vahine) in MiliQ water was perfused through one inlet, while through the other inlet only water was perfused, both at a pressure of 200 mbar using a Precision Pressure Control System P2CS pump (Biophysical tools). The liquid coming from the outlets was used to measure the concentration of BSA with a PierceTM BCA Protein Assay Kit and the concentration of blue dye by identifying the absorbance in the 640 nm wavelength with a Benchmark Plus Microplate Reader (4100172C, Bio-Rad). To study the gradient *in situ*, 25 µg/mL of fluorescein (F2456, Sigma-Aldrich) in a solution of 10 mM of NaOH was perfused through one of the inlets and the solution without fluorescein through the other at a constant pressure of 200 mbar. Fluorescent images were taken using a ZEISS Axio Observer Z1/7 microscope and treated with FIJI software to obtain a large image.

## 3.14. TMRE readout optimization

To ensure that tetramethylrhodamine (TMRE) could be used as a readout for apoptotic induction identification, 100,000 cells were resuspended in 1 mL of complete media and treated with the desired drugs. 100 µL of the cell solution was plated in 8 different wells of a 96-well plate for every condition and incubated with the different treatments for 16 hours at 37 ºC. After the incubation, media was extracted from the wells and 100 µL of new complete media with 400 nM of TMRE (ab275547, Abcam) and 2 mM of Calcein AM (C1430, ThermoFisher) were added and incubated for 30 minutes at 37 ºC. Next, all wells were carefully cleaned with PBS and 50 µL of MEB with 0.001% of digitonin and the different conditions of BIM BH3 peptides were added to each well of each condition (control with DMSO and BIM concentrations of 10, 3, 1, 0.3, 0.1, 0.03 and 0.01 µM), followed by incubation for 2 hours at room temperature. Several images

of every well were taken using a Nikon TI2 fluorescence microscope (Nikon Instruments).

## 3.15. Image processing

Using FIJI software macros, images obtained from the different experiments were separated in fluorescent fields applying the same image processing for an individual experiment. The complete set was uploaded to CellProfiler and individual cells were identified using the calcein AM (alive cells) field. For each identified cell, the intensity of the TMRE (apoptotic identification dye) field was quantified and a threshold to separate apoptotic (TMRE negative) from non-apoptotic (TMRE positive) cells were selected using the 10 percentile intensity in the condition of untreated cells without BIM peptide. To generate the apoptotic response curve necessary for DBP, the percentage of positive TMRE cells for each condition was used. In the case of GIST primary cells, only cells with a positive signal on the cKIT field were used for the quantification.

## 3.16. Microfluidic-based dynamic BH3 profiling

Before starting the cell seeding, microfluidic chips were placed in an oven at 85 ºC for 1 hour. After that, 10 µL of sterile MiliQ water with 15 µg/mL of poly-L-lysine (0413, Quimigen) was added to each well and incubated at 37 ºC for 40 minutes to coat the well surface, followed by cleaning with more sterile MiliQ water. After well functionalization, 100,000 cells were resuspended in 600 µL of complete media, separated into 3 different tubes and treated with the desired concentration of the anticancer drug. 35 µL of the cell suspension was seeded in each 5 wells per row of the chip, having one row for every condition. Microfluidic chips were then incubated for 16 hours at 37 ºC. After the incubation, cell chambers were refilled with complete media to avoid bubbles and sealed with a glass slide secured with plastic alligator clips. The same steps that were used in the optimization of the readout were repeated inside the microfluidic chip using the P2SC pump:

1) Perfusion of complete media with 400 nM of TMRE and 2 µM of calcein AM at 300 mbar for 15 minutes. Incubation at 37 ºC for 30 minutes.
2) Perfusion of PBS at 300 mbar for 10 minutes.
3) Perfusion of MEB with 0.001% of digitonin through one inlet, while through the other one the same buffer was perfused with BIM peptide (2 µM in the case of GIST-T1 cell line, 0.2 µM in the case of GIST-T1/670 and 3 µM for the primary sample). The pump was set at 200 mbar for 20 minutes.

After the DBP protocol inside the microfluidic chip, the device was incubated for 2 hours at room temperature and several images of each cell chamber were taken using a Nikon TI2 fluorescence microscope and treated as previously described.

## 3.17. Solid tumor disaggregation

For solid tumor biopsies, the sample was exposed to 5 mL of DMEM/F12 (11320033, ThermoFisher Scientific) with 100 units of hyaluronidase (H3506, Sigma-Aldrich), 300 units of collagenase IV (17104-019, Thermo Fisher Scientific) and 125 units of DNAse I (DN25, Sigma-Aldrich). Using a GentleMACS dissagregator (Miltenyl Biotec), the tumor was processed two times with the hTumor1 program and incubated for 30 minutes at 37 ºC. If after the first round there were still big pieces of the tumor, the suspension was processed again in the disaggregator and incubated for 15-30 more minutes. After dissociation, the resulting suspension was filtered with a 70 µm filter and cells were pulled down at 500 g for 5 minutes. If required, erythrocytes were lysed by exposing the sample to ice-cold sterile MiliQ water for 15 seconds and adding PBS to stop the process. Cells were then pulled down again, resuspended in complete RPMI medium, counted and seeded to perform DBP or cryopreservation in liquid nitrogen.

## 3.18. Statistical analysis

All results are expressed as the mean ± S.E.M. of at least three biologically independent replicates, except in the case of primary or PDXs samples where it was impossible to perform three different experiments. Every condition was compared to its related control condition using two-tailed unpaired t-test and marked statistically significant when p-value < 0.05 (*) or p-value < 0.01 (**). GraphPad Prism 9 was used to perform statistical analyses and represent the results.

# Chapter IV

## Personalization of pediatric B-cell precursor acute lymphoblastic leukemia treatment

## 4.1. Combining standard-of-care therapies with BH3 mimetics improves pediatric BCP-ALL treatment

### 4.1.1. DBP identifies effective chemotherapies in BCP-ALL cell lines

Pediatric BCP-ALL patients are normally treated with chemotherapeutic agents in the clinic, achieving very good responses. However, the side effects that patients suffer can greatly affect their quality of life during and after therapy. We hypothesized that the functional assay DBP can predict the efficacy of different therapies and adapt patients' treatment to decrease dosing and side effects. We used two BCP-ALL cell lines, NALM-6 (from a 19-year-old man patient with near diploid karyotype and *ETV6-PDGFRβ* translocation) and SEM (from a 5-year-old girl with a *KMT2A-AFF1* translocation), and a library of chemotherapeutic drugs used in the different steps of these patients' treatment. This collection included vincristine, L-asparaginase, two corticosteroids (prednisone and dexamethasone), two anthracyclines (doxorubicin and daunorubicin) and the three drugs used for the intrathecal chemotherapy (methotrexate, cytarabine and hydrocortisone).

First, we incubated the two BCP-ALL cell lines with the different treatments and performed the DBP assay (Figure 9). Most chemotherapeutic agents affect the cell cycle and produce apoptotic cell death when they cannot enter mitosis. Therefore, the incubation time with these drugs is important: if the cell cycle is not blocked, no change in apoptotic priming will be observed. In the NALM-6 cell line, 16 hours of incubation is sufficient to identify an increase in apoptotic priming with vincristine, dexamethasone, doxorubicin, daunorubicin, methotrexate and cytarabine (Figure 10A). But 16 hours of incubation in the SEM cell line produces no changes in apoptosis induction (data not shown). Thus, we hypothesized that this cell line requires longer incubation timepoints with chemotherapeutic treatments to observe the initiation of apoptosis. In this case, we expanded the incubation to 40 hours and observed an increase in Δ%priming with L-asparaginase, dexamethasone, doxorubicin, daunorubicin, methotrexate, cytarabine and hydrocortisone (Figure 10A). To test whether these changes in apoptotic priming correlate with later cytotoxicity, we performed a cell death assay with annexin V and DAPI at 72 h. We observed that vincristine, L-asparaginase, dexamethasone, doxorubicin, daunorubicin, methotrexate, cytarabine and hydrocortisone caused a statistically significant increase in cell death compared to the control in both cell lines (Figure 10B).

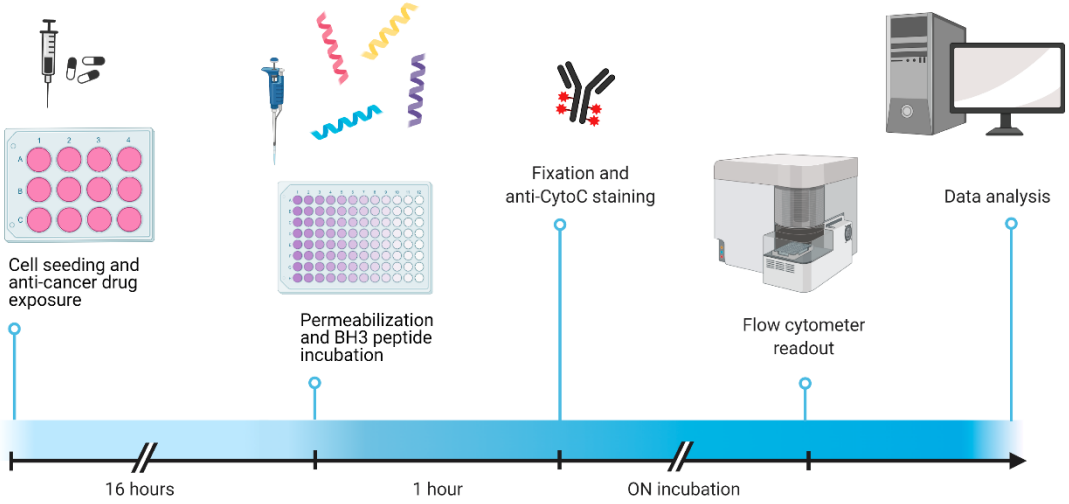


**Figure 9. Graphical scheme of the DBP technique**. After drug exposure for ~16 h, cells were plated in 96-well plates and exposed to the different BH3 peptides. After 1 h, cells were fixed and stained with an anti-Cytochrome C antibody overnight. Finally, analyses were performed using a flow cytometer for drug-response curves. Designed with BioRender.com.

To test the predictive capacity of DBP in BCP-ALL we used the Receiver Operating Characteristic (ROC) curve analysis. This statistical method measures the predictive ability of a diagnostic system by representing the true positive rate versus the false positive rate. The area under the curve represents the predictive power between 0.5 and 1, being a perfect predictor a test with an area under the ROC curve of 1. Most clinically approved tests have an area under the ROC curve of around 0.8. In our case, we obtained an area of ~0.8 (Figure 10C), indicating and acceptable identification of chemotherapeutic treatments in BCP-ALL cell lines with DBP. Although the magnitude of priming obtained in DBP depends on the incubation time with each drug, as they present different dynamics, we obtained a statistically significant correlation between priming and cell death (Figure 10D). These results demonstrate that DBP can be used to predict the efficacy of chemotherapy in BCP-ALL cell lines, as has already been demonstrated in other types of cancer.

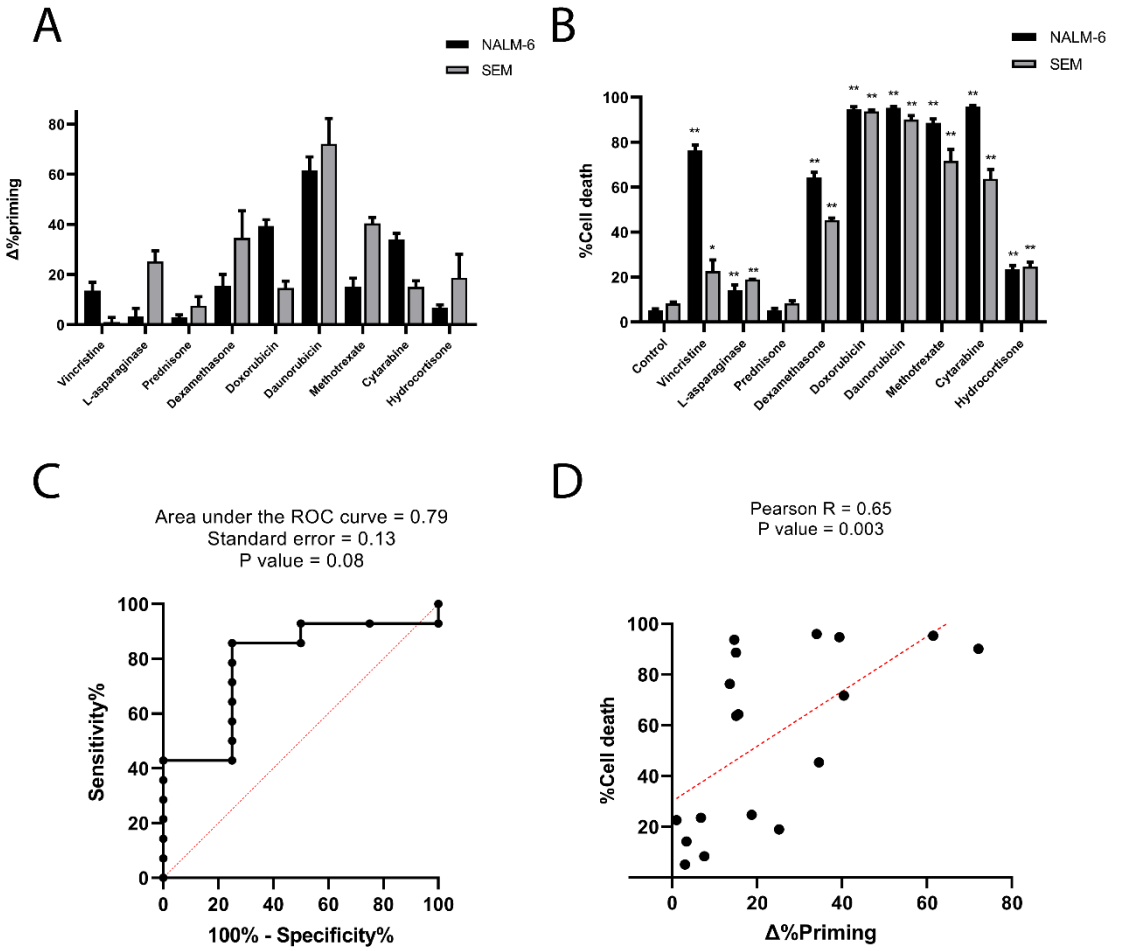


**Figure 10. Chemotherapy effectiveness prediction using DBP in BCP-ALL cell lines. A)** DBP with BIM BH3 peptide after 16 h incubation in NALM-6 and 40 h in SEM cell lines with vincristine 1 nM, L-asparaginase 0.5 IU/mL, prednisone 100 nM, dexamethasone 100 nM, doxorubicin 100 nM, daunorubicin 100 nM, methotrexate 100 nM, cytarabine 100 nM and hydrocortisone 1000 nM. Δ%priming stands for the difference in %priming between treatment and control conditions. **B)** Cytotoxicity expressed as percentage of dead cells after 72 h of treatment with the same therapies assessed by Annexin V/DAPI staining. **C)** ROC curve analysis using the values of Δ%priming in NALM-6 and SEM cell lines establishing 20% as the cell death threshold for responders and non-responders. **D)** Correlation between Δ%priming and %cell death analyses. All results are expressed as the mean ± standard error of the mean (SEM) of at least three biologically independent replicates. Statistical significance was calculated using Student's t-test comparing to control condition and considering *$p < 0.05$ and **$p < 0.01$.

### 4.1.2. Chemotherapy induces antiapoptotic adaptations that can be targeted with BH3 mimetics

Secondary effects resulting from anticancer therapy are particularly threatening for the pediatric population[113]. As a result, there is a trend to substitute high-dose single agent treatment for low-dose combinations to maximize efficacy and reduce undesired toxicity[284]. To overcome this decrease in efficacy, observed when reducing the dose of

standard treatment, we hypothesized that we could exploit antiapoptotic adaptations induced by chemotherapy, with the aim to treat patients with a first round of low-dose chemotherapy followed by the specific BH3 mimetic. To do this, we must first identify which antiapoptotic protein cells use to acquire resistance to chemotherapeutics. In this regard, the DBP utilizes synthetic BH3 peptides with specific affinity for the different antiapoptotic proteins to precisely identify these adaptations. In brief, an increase in apoptotic priming after incubating with the BAD BH3 peptide would mean that BCL-2, BCL-xL and/or BCL-w are involved in cell's resistance. Similarly, a gain in apoptotic priming with HRK BH3 would indicate an enhanced BCL-xL contribution, while an MS1 BH3 signal increase would point to MCL-1. In the NALM-6 cell line, after the incubation for 16 hours with dexamethasone, we tested the cells with the BAD, HRK and MS1 peptides. For all these assays, we used a low BAD BH3 peptide concentration, due to the exceptional sensitivity of both BCP-ALL cell lines to this peptide. We could observe that the preincubation with dexamethasone induced an increase in apoptotic priming with all three peptides compared to untreated cells (Figure 11A), suggesting that all three antiapoptotic proteins play a certain role in the acquired resistance in response to dexamethasone. To demonstrate that the combination of dexamethasone with a BH3 mimetic could improve treatment efficacy, we incubated NALM-6 cells with different treatments for 96 hours and studied cytotoxicity. In these cells, a 10-fold reduction of the concentration of dexamethasone was not very cytotoxic, achieving only about 20% of cell death (Figure 11B). Similarly, BH3 mimetics (ABT-199 against BCL-2, A133 against BCL-xL and S63845 against MCL1) as single agents did not produce a significant increase in cytotoxicity in these cells neither (Figure 11B). However, when these cells were treated with dexamethasone and one of the BH3 mimetics was added after 16 hours of incubation (when antiapoptotic adaptations are observed with DBP), we noticed an increase in cytotoxicity with the combination compared to the two treatments alone when added together. To quantify the effect of the combination we calculated the Combination Index (CI)[285], which indicates whether a combination is synergistic (CI<1), additive (CI=1) or antagonistic (CI>1). The combination of dexamethasone with any BH3 mimetics was clearly synergistic (Figure 11B), confirming that the antiapoptotic adaptations observed with DBP can be exploited with the use of BCL-2, BCL-xL or MCL-1 inhibitors.

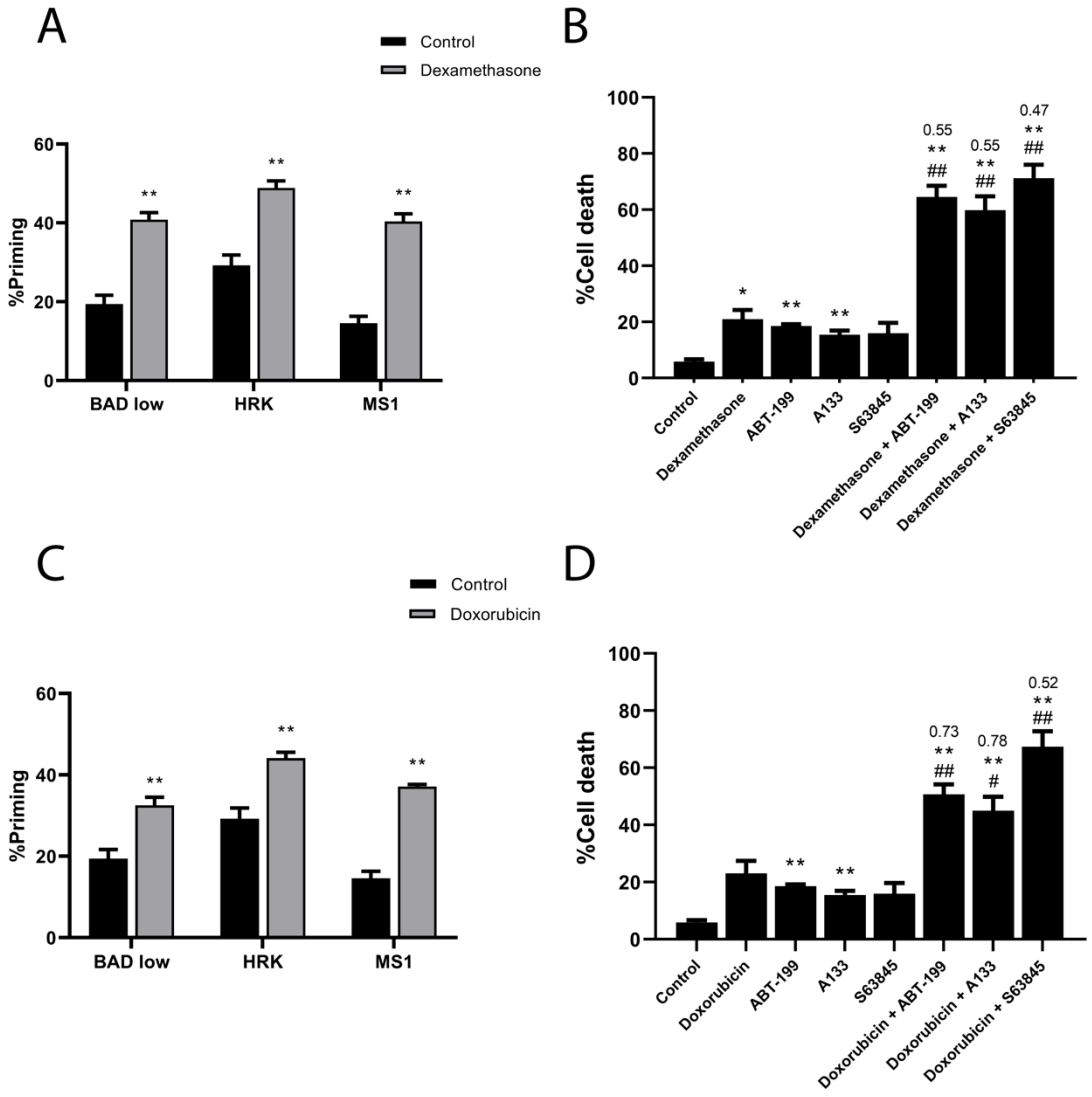


**Figure 11**. **Dexamethasone and doxorubicin induce adaptations using the three antiapoptotic proteins in NALM-6 cell line. A)** DBP results using sensitizer peptides to study antiapoptotic dependencies of BCL-2 and BCL-xL with BAD 0.1 μM, BCL-xL with HRK 100 μM and MCL-1 with MS1 10 μM after 16 h of incubation with dexamethasone 100 nM in the NALM-6 cell line. **B)** Cytotoxicity was assessed by Annexin V/DAPI staining after 96 h incubation with dexamethasone 10 nM, ABT-199 100 nM, A133 100 nM and S63845 1,000 nM in the NALM-6 cell line. BH3 mimetics were added 16 h after treatment initiation. **C)** DBP results using sensitizer peptides to study antiapoptotic dependences of BCL-2 and BCL-xL with BAD 0.1 μM, BCL-xL with HRK 100 μM and MCL-1 with MS1 10 μM after 16 h of incubation with doxorubicin 100 nM in the NALM-6 cell line. **D)** Cytotoxicity was assessed by Annexin V/DAPI staining after 96 h incubation with doxorubicin 10 nM, ABT-199 100 nM, A133 100 nM and S63845 1,000 nM in the NALM-6 cell line. BH3 mimetics were added 16 h after treatment initiation. All results are expressed as the mean ± standard error of the mean (SEM) of at least three biologically independent replicates. Statistical significance was calculated using Student's t-test compared to control condition and considering *p < 0.05 and **p < 0.01. Significance was also calculated comparing combination conditions with both single agents and considering #p < 0.05 and ##p < 0.01. CI value is indicated on top of every combination where CI < 1 indicates synergy.

When analyzing doxorubicin, we also identified an increase in apoptotic priming with all three peptides. The difference in priming between control and doxorubicin-treated cells was lower with BAD and HRK than with MS1, suggesting that in this case there is a stronger contribution of MCL-1 (Figure 11C). Doxorubicin at a concentration of 100 nM was effective in NALM-6 cells (Figure 10B), but with a 10-fold reduction in concentration it loses its cytotoxic effect (Figure 11D). To enhance the effect of doxorubicin at low doses, we combined it with different BH3 mimetics to exploit the antiapoptotic adaptations induced by this treatment. We found that the combination of doxorubicin with the MCL-1 inhibitor S63845 produced a synergistic effect with a CI of 0.52 (Figure 11D). Moreover, combinations with ABT-199 and A133 were not as effective, showing higher CI and validating the DBP results that indicated a higher MCL-1 dependence caused by doxorubicin (Figure 11D).

Nonetheless, short treatments with L-asparaginase in NALM-6 cells produced a different response. Upon this agent, only BAD showed an increase in apoptotic priming compared with control cells (Figure 12A). These results indicate that the adaptation is mostly mediated by BCL-2 (and maybe BCL-w), since we have no signal after the incubation with HRK that would point to a contribution of BCL-xL. We then combined dexamethasone, that as single agent is not very cytotoxic in these cells, with BH3 mimetics. Correlating with DBP predictions, the combination of dexamethasone with the BCL-2 inhibitor ABT-199 was highly synergistic (Figure 12B). Surprisingly, the combination with A133 also caused a synergistic effect, which was not previously identified with the HRK peptide in DBP (Figure 12B). Finally, the MCL-1 inhibitor, as expected, did not produce any cell death enhancement, confirming the results obtained by DBP (Figure 12B).

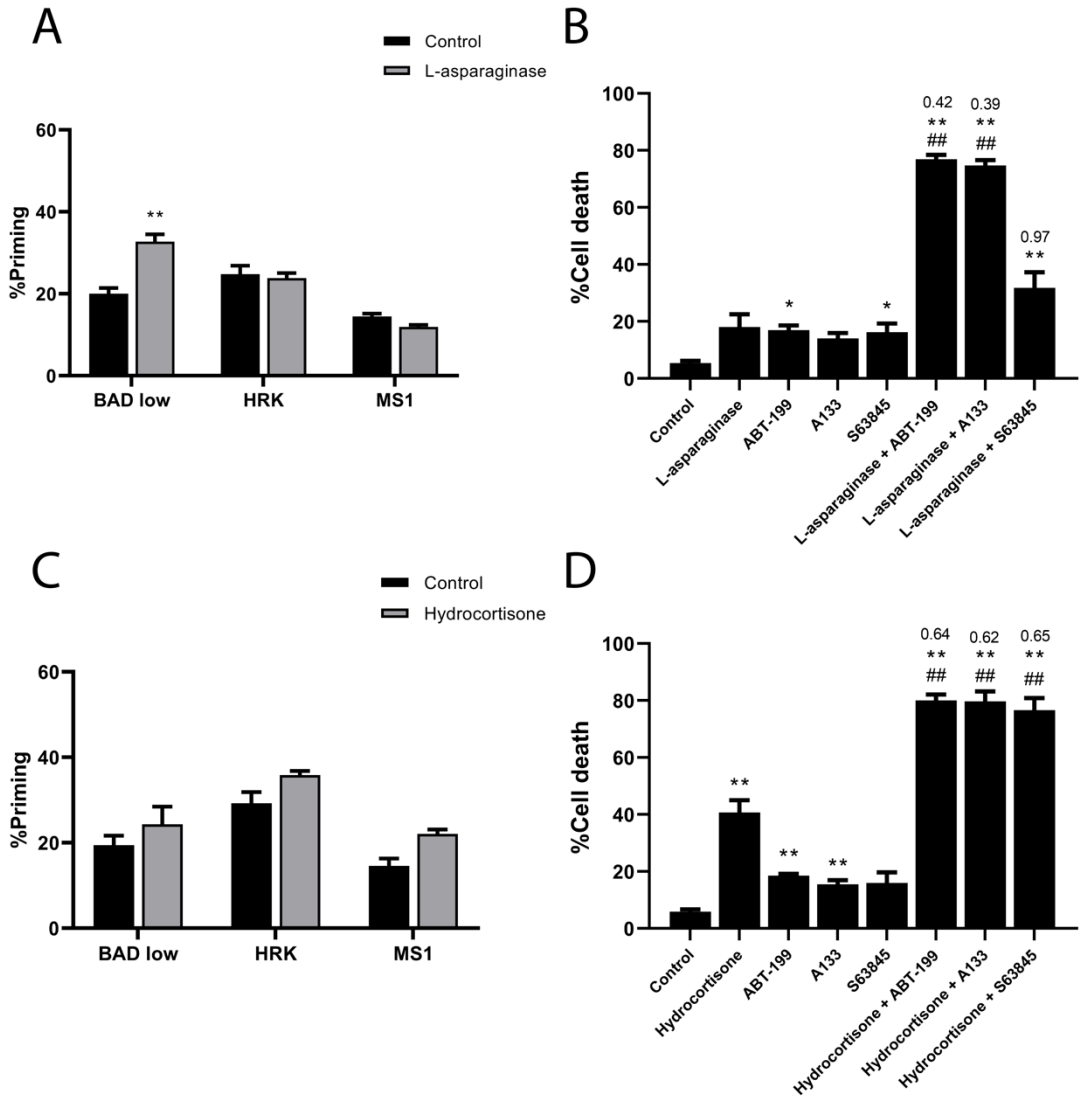


**Figure 12**. **Adaptations produced by L-asparaginase and hydrocortisone are partially identified with DBP. A)** DBP results using sensitizer peptides to study antiapoptotic dependencies of BCL-2 and BCL-xL with BAD 0.1 μM, BCL-xL with HRK 100 μM and MCL-1 with MS1 10 μM after 16 h of incubation with L-asparaginase 0.5 IU/mL in the NALM-6 cell line. **B)** Cytotoxicity was assessed by Annexin V/DAPI staining after 96 h incubation with L-asparaginase 0.5 IU/mL, ABT-199 100 nM, A133 100 nM and S63845 1,000 nM in the NALM-6 cell line. BH3 mimetics were added 16 h after treatment initiation. **C)** DBP results using sensitizer peptides to study antiapoptotic dependencies of BCL-2 and BCL-xL with BAD 0.1 μM, BCL-xL with HRK 100 μM and MCL-1 with MS1 10 μM after 16 h of incubation with hydrocortisone 1,000 nM in the NALM-6 cell line. **D)** Cytotoxicity was assessed by Annexin V/DAPI staining after 96 h incubation with hydrocortisone 1,000 nM, ABT-199 100 nM, A133 100 nM and S63845 1,000 nM in the NALM-6 cell line. BH3 mimetics were added 16 h after treatment initiation. All results are expressed as the mean ± standard error of the mean (SEM) of at least three biologically independent replicates. Statistical significance was calculated using Student's t-test compared to control condition and considering *$p < 0.05$ and **$p < 0.01$. Significance was also calculated comparing combination conditions with both single agents and considering #$p < 0.05$ and ##$p < 0.01$. CI value is indicated on top of every combination where CI < 1 indicates synergy.

The last treatment where we studied antiapoptotic adaptations using specific peptides was hydrocortisone. In this case, after exposing the treated cells to the different peptides we saw a small increase in apoptotic priming, but it was not statistically significant (Figure 12C). When combining hydrocortisone with the different BH3 mimetics we saw a similar synergistic effect with the three inhibitors, improving the cytotoxic effect of the separate treatments (Figure 12D). In this case the antiapoptotic adaptations after hydrocortisone were not identified by DBP, probably caused by a non-optimal incubation time. These results with upon hydrocortisone treatment suggest that we should perform a time course to see how the apoptotic priming evolves over time. Overall, DBP can identify most antiapoptotic adaptations that occur after treating NALM-6 cells with chemotherapeutic drugs. This allows us to design rational combinations of chemotherapy with BH3 mimetics to avoid chemotherapy-associated side effects or boost the efficacy of ineffective drugs. Dexamethasone and doxorubicin as single agents could eliminate these cells quite effectively. Yet, by identifying antiapoptotic adaptations, the concentration can be reduced to avoid potential side effects, achieving the same cytotoxicity when a BH3 mimetic is added in combination to the chemotherapeutic agent. On the other hand, L-asparaginase and hydrocortisone are treatments that produce modest cytotoxicity on their own. But adding a BH3 mimetic in combination provides a synergistic effect that boosts overall cytotoxicity.

In the case of the SEM cell line, we also observed antiapoptotic adaptations with these same treatments. Similarly as before, it was necessary to incubate these cells for 40 hours with the different chemotherapeutic treatments, since 16 hours was not enough to detect apoptotic priming changes. The predictions obtained with the three sensitizer peptides showed a clear increase in apoptotic priming after treatment with dexamethasone, implying that the three antiapoptotic proteins were involved in the adaptation (Figure 13A). We then performed cell death assays combining dexamethasone with the different BH3 mimetics. Reducing the concentration of dexamethasone resulted in a loss of its cytotoxicity in these cells, but it could be restored by combining it with BH3 mimetics. Especially with the BCL-2 and MCL-1 inhibitors a marked synergistic effect was observed, but not with the BCL-xL inhibitor that showed an additive effect with a CI close to 1 (Figure 13B). Another treatment that induced changes in apoptotic priming after incubation with sensitizer peptides was L-asparaginase. DBP analyses showed an increase in priming with all three peptides (Figure 13C), a different response compared to NALM-6 (Figure 12A). By combining L-asparaginase with the three BH3 mimetics we were able to find a synergy in all combinations, as predicted by DBP (Figure 13D). In this case we observed a clear

differential response with the two cell lines to the same treatment, since in NALM-6 cells there was no adaptation by MCL-1. Finally, in the case of hydrocortisone treatment we did identify a statistically significant increase in priming with BAD, HRK and MS1 (Figure 13E). And we observed a synergy especially when combining it with ABT-199 and S63845 (Figure 13F).

Collectively, DBP can identify antiapoptotic adaptations in BCP-ALL cell lines treated with chemotherapies commonly used in the clinic. When exposing these cell lines to dexamethasone, L-asparaginase or hydrocortisone, and doxorubicin in NALM-6 cells, the sequential addition of BH3 mimetics produces a synergistic effect that enhanced cytotoxicity. Thus, using this combination strategy we could reduce the concentration of effective chemotherapeutics and potential secondary effects, or enhance cytotoxicity for non-effective drugs, aiming to improve treatment and the quality of life of the patients.

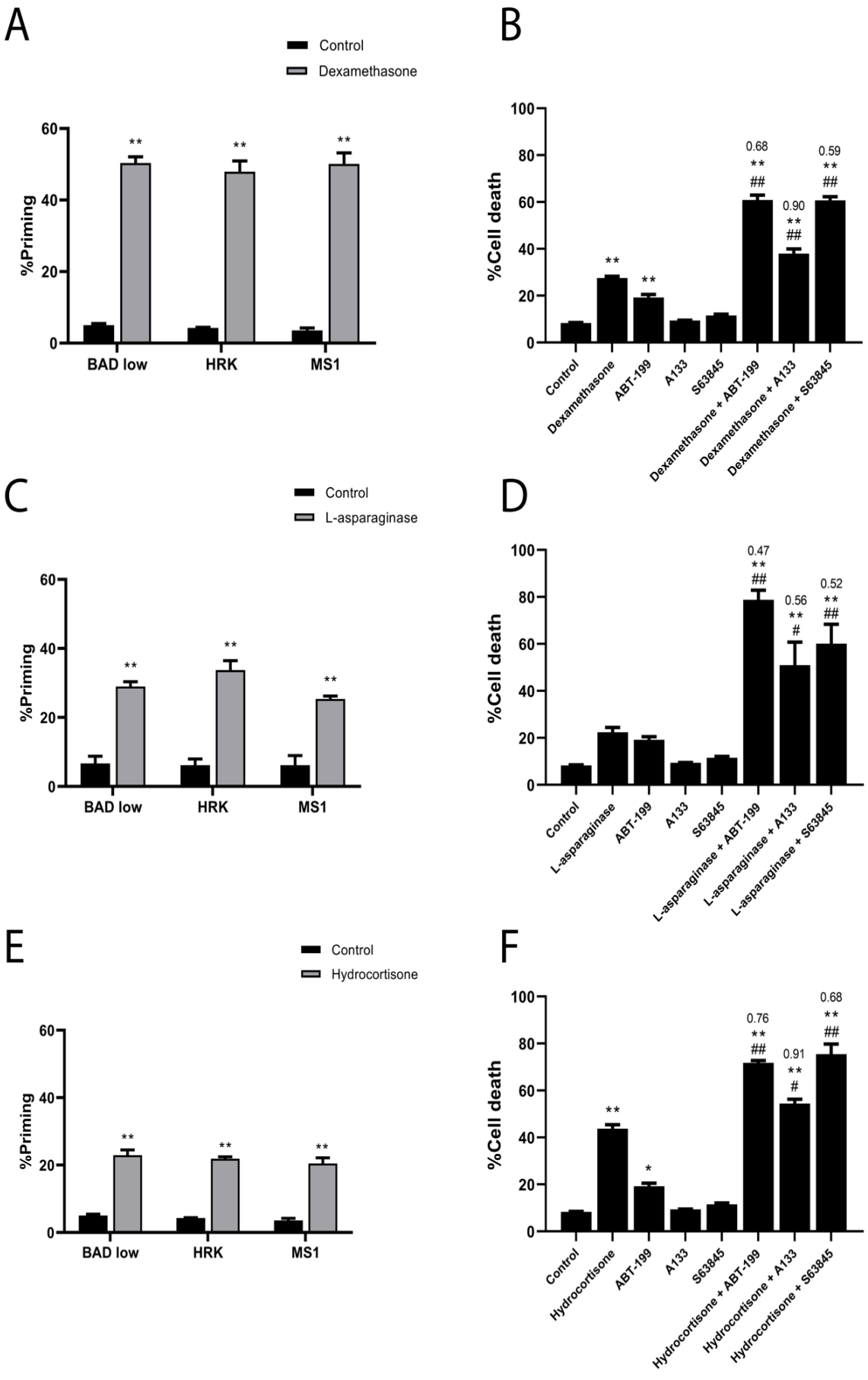
A
Control
Dexamethasone
%Priming
BAD low
HRK
MS1
B
%Cell death
Control
Dexamethasone
ABT-199
A133
S63845
Dexamethasone + ABT-199
Dexamethasone + A133
Dexamethasone + S63845
C
Control
L-asparaginase
%Priming
BAD low
HRK
MS1
D
%Cell death
Control
L-asparaginase
ABT-199
A133
S63845
L-asparaginase + ABT-199
L-asparaginase + A133
L-asparaginase + S63845
E
Control
Hydrocortisone
%Priming
BAD low
HRK
MS1
F
%Cell death
Control
Hydrocortisone
ABT-199
A133
S63845
Hydrocortisone + ABT-199
Hydrocortisone + A133
Hydrocortisone + S63845

**Figure 13. Similar adaptations are observed after treatment with dexamethasone, L-asparaginase and hydrocortisone in SEM cell line. A**) DBP results using sensitizer peptides to study antiapoptotic dependencies of BCL-2 and BCL-xL with BAD 0.1 μM, BCL-xL with HRK 100 μM and MCL-1 with MS1 10 μM after 40 h of incubation with dexamethasone 100 nM in the SEM cell line. **B**) Cytotoxicity was assessed by Annexin V/DAPI staining after 96 h incubation with dexamethasone 10 nM, ABT-199 10 nM, A133 100 nM and S63845 1,000 nM in the SEM cell line. BH3 mimetics were added 16 h after treatment initation. **C**) DBP results using sensitizer peptides to study antiapoptotic dependencies of BCL-2 and BCL-xL with BAD 0.1 μM, BCL-xL with HRK 100 μM and MCL-1 with MS1 10 μM after 40 h of incubation with L-asparaginase 0.5 IU/mL in the SEM cell line. **D**) Cytotoxicity was assessed by Annexin V/DAPI staining after 96 h incubation with L-asparaginase 0.5 IU/mL, ABT-199 10 nM, A133 100 nM and S63845 1,000 nM in the SEM cell line. BH3 mimetics were added 16 h after treatment initation. **E**) DBP results using sensitizer peptides to study antiapoptotic dependencies of BCL-2 and BCL-xL with BAD 0.1 μM, BCL-xL with HRK 100 μM and MCL-1 with MS1 10 μM after 40 h of incubation with hydrocortisone 1,000 nM in the SEM cell line. **F**) Cytotoxicity was assessed by Annexin V/DAPI staining after 96 h incubation with hydrocortisone 1,000 nM, ABT-199 10 nM, A133 100 nM and S63845 1,000 nM in the SEM cell line. BH3 mimetics were added 16 h after treatment initation. Statistical significance was calculated using Student's t-test compared to control condition and considering *$p < 0.05$ and **$p < 0.01$. Significance was also calculated comparing combination conditions with both single agents and considering #$p < 0.05$ and ##$p < 0.01$. CI value is indicated on top of every combination where CI < 1 indicates synergy.

### 4.1.3. Results in BCP-ALL cell lines are recapitulated in patient-derived xenografts

In collaboration with the University of Ulm and Dr. Seyfried, Prof. Debatin and Prof. Meyer we further studied four PDX models from BCP-ALL patients. We used the same chemotherapeutic treatments, incubated these PDX-isolated cells for 16 hours, and analyzed them by DBP. Unfortunately, as primary cells rapidly lose their viability it was not possible to do cell death assays at longer timepoints for these samples.

Using the BIM peptide, we observed that several treatments increased overall priming. For instance, we detected that daunorubicin caused an increase in priming in all PDX samples analyzed. In fact, after treatment most cells were already dead (Figure 14A). Comparing these results with cell lines, we detected in both cases high daunorubicin-induced cell death (Figure 10A,B). Dexamethasone was another treatment that caused an increase in apoptotic priming in almost all PDX samples, except for X068 which did not respond to this drug (Figure 14A). We also detected other treatments that were effective for one of the PDXs, highlighting the importance of predicting which therapies would work in each case. For example, sample PDX X142 appeared quite resistant to all treatments, showing a very low apoptotic priming change (except for dexamethasone and daunorubicin). But they were the only cells that showed a clear increase in priming with hydrocortisone compared to the other three PDXs analyzed (Figure 14A). Other treatments also appeared as positive hits. This is the case of PDX X133, which showed an increase in apoptotic priming with high concentrations of L-asparaginase, doxorubicin, methotrexate and cytarabine (Figure 14A). For PDX X068,

in addition to the aforementioned treatments, changes in priming were also observed with L-asparaginase, prednisone and doxorubicin (Figure 14A).

The different cytotoxic effects caused by chemotherapeutic treatments vary depending on the sample analyzed and was more evident when we checked antiapoptotic adaptations. With daunorubicin we saw an increase in priming in all samples and peptides (Figure 14B,C,D), caused by the rapid cytotoxicity produced by this treatment. Overall, all PDX samples presented different responses to peptides. In the case of the PDX X281 no clear antiapoptotic adaptation could be observed with any agent, the most remarkable being a small increase after BAD peptide with dexamethasone suggesting an important role of BCL-2 (Figure 14B). The PDX X068 did show a clear BCL-2-mediated adaptation after treatment with L-asparaginase and doxorubicin (Figure 14B,C). In contrast, in PDX X142 we identified an increase in priming with BAD and HRK peptides upon treatment with dexamethasone and hydrocortisone, suggesting BCL-2 and BCL-xL-mediated adaptation (Figure 14B,C). Finally, PDX X133 presented two clear adaptations: cytarabine induced an adaptation by BCL-2 (identified by a positive BAD and negative HRK signal), and doxorubicin through MCL-1 (positive signal with MS1) (Figure 14B,C,D). Other adaptations with a minor priming increase were also detected, especially with the BAD peptide, which suggests the potential use of the only BH3 mimetic approved yet for the clinic (venetoclax or ABT-199) to improve refractory cases' treatment.

These results demonstrate that patient-derived cells present different responses to chemotherapeutic agents and combinations with BH3 mimetics. This heterogeneity correlates with the differential response to treatments observed in the clinic and highlights the importance of using functional assays to guide therapy to maximize effectiveness and minimize side effects. With DBP we could quickly and accurately identify which treatments were effective and identify antiapoptotic adaptations that could be exploited with BH3 mimetics.

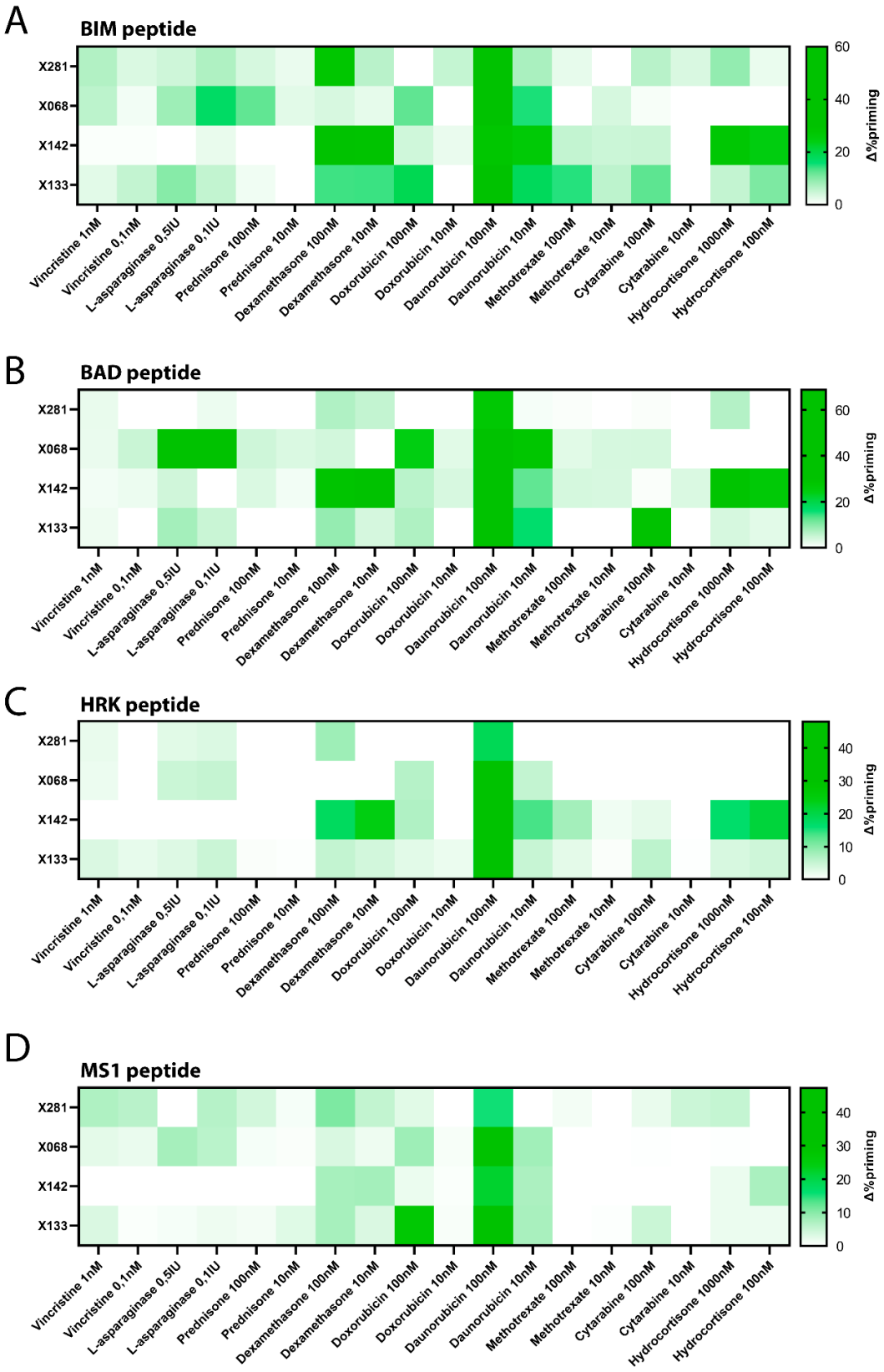


**Figure 14. DBP is effective on the identification of effective treatments and antiapoptotic adaptations in PDX samples**. DBP with **A)** BIM BH3, **B)** BAD BH3, **C)** HRK BH3 and **D)** MS1 BH3 peptides after 16 hours of incubation with the different chemotherapeutic drugs in four BCP-ALL PDX samples. Δ%priming stands for the difference in %priming between treatment and control condition.

## 4.2. Targeted treatments with BH3 mimetics could be used in relapsed patients

This part of the thesis is based on the published paper: “Manzano-Muñoz A, Alcon C, Menéndez P, Ramírez M, Seyfried F, Debatin KM, Meyer LH, Samitier J, Montero J. MCL-1 Inhibition Overcomes Antiapoptotic Adaptation to Targeted Therapies in B-Cell Precursor Acute Lymphoblastic Leukemia. Front Cell Dev Biol. 2021 Sep 9;9:695225. doi: 10.3389/fcell.2021.695225. PMID: 34568318; PMCID: PMC8458912.”

### 4.2.1. DBP predicts targeted drug efficacy in our two BCP-ALL cell line models

As previously discussed, some targeted therapies are currently explored for certain subtypes of BCP-ALL. These therapies could also be used to complement aggressive chemotherapy regimens for R/R patients, but it would be necessary to identify which targeted therapy will be effective for each case. In BCP-ALL several drugs have been proposed to be effective, including imatinib and dasatinib for Ph+ cases; trametinib in patients with mutated RAS[286]; sunitinib in cells with FLT3 mutated or overexpressed[287]; ruxolitinib for tumors with constitutive activation of the JAK/STAT signaling pathway[288] and ibrutinib when the receptor pre-BCR is active[289]. For this part of the project, we tested all these treatments in the two BCP-ALL models to identify using DBP which specific inhibitors would be cytotoxic for the NALM-6 and SEM cell lines.

In contrast to the results obtained with chemotherapeutic agents, we identified changes in apoptotic priming in both *in vitro* models after a short incubation for 16 hours. Sunitinib (a multi-target inhibitor) caused a clear increment in priming with the BIM peptide in the SEM cell line, while trametinib (a widely used MEK inhibitor) also caused an increase in both cell lines. The other tyrosine kinase inhibitors tested did not significantly promote apoptotic priming (Figure 15A). To verify these predictions by DBP, we used the same treatments with longer incubations for cell death analyses. The only treatments that increased cytotoxicity compared to control conditions were sunitinib in SEM cells and trametinib in both cell lines, the same treatments that were identified by DBP (Figure 15B). We used a ROC curve analysis to assess the predictive ability of DBP to identify targeted cytotoxic treatments in BCP-ALL, obtaining an area under the curve of 1; thus, revealing a perfect cytotoxicity prediction (Figure 15C). Furthermore, Δ% priming strongly correlated with cell death, validating that a

higher increase in apoptotic priming is an early predictor for cytotoxicity in these cells and targeted agents (Figure 15D).

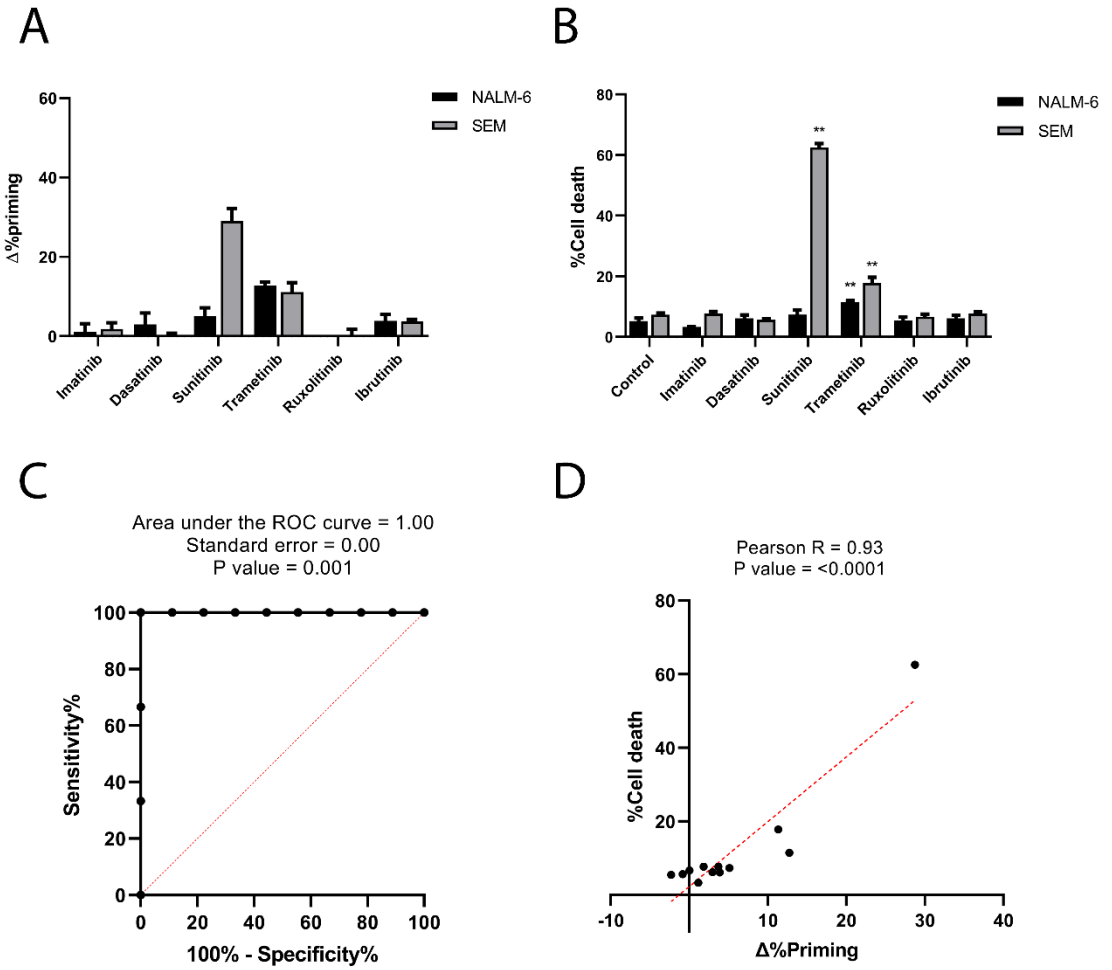


**Figure 15. DBP predicts cytotoxicity of targeted agents in BCP-ALL cell lines. A)** DBP with BIM BH3 peptide after 16 h of incubation with 1,000 nM imatinib, 100 nM dasatinib, 1,000 nM sunitinib, 100 nM trametinib, 100 nM ruxolitinib, and 1,000 nM ibrutinib in NALM-6 and SEM cell lines. Δ%priming stands for the difference in %priming between treatment and control conditions. **B)** Cytotoxicity expressed as percentage of dead cells after 72 h of treatment with the same therapies assessed by Annexin V/DAPI staining. **C)** ROC curve analysis using the values of Δ%priming in NALM-6 and SEM cell lines establishing 10% as the cell death threshold for responders and non-responders. **D)** Correlation between Δ%priming and %cell death analyses. All results are expressed as the mean ± standard error of the mean (SEM) of at least three biologically independent replicates. Statistical significance was calculated using Student's t-test comparing to control condition and considering *p < 0.05 and **p < 0.01.

### 4.2.2. Trametinib induces an MCL-1 adaptation in NALM-6 cell line

The only treatment that showed a certain effect on NALM-6 cells by DBP was trametinib, although after 72 hours of incubation it only caused 20% of cell death. To

improve its efficacy, as previously described for chemotherapy, we studied whether trametinib caused antiapoptotic adaptations using BH3 sensitizer peptides, that could be then potentially exploited with BH3 mimetics. Treatment with trametinib caused an increase in apoptotic priming when exposed to BAD, HRK and MS1 peptides, suggesting that multiple antiapoptotic proteins were involved in cells' adaptation to therapy (Figure 16A). To test whether antiapoptotic adaptations could be used to boost the effect of trametinib, we combined it with ABT-199, A133 and S63845. All three BH3 mimetics showed a synergistic effect with the MEK inhibitor when sequentially added 16 hours after treatment initiation. However, the dual inhibition of MEK and MCL-1 was significantly more effective and clearly synergistic (CI = 0.28), achieving almost a complete elimination of BCP-ALL cells (Figure 16B). To identify the biological mechanism underneath this synergy, we used western blot analyses to assess the BCL-2 family proteins expression. In different types of cancer, the inhibition of the MAPK pathway leads to an increase in BIM protein levels[290], which we also observed in the NALM-6 cell line after treatment with trametinib (Figure 16C). The increase in the expression of proapoptotic BIM should activate apoptosis, but several laboratories reported that antiapoptotic proteins could compensate and block the excess of BIM[291,292]. When we analyzed the antiapoptotic proteins expression, we found that the MEK inhibitor selectively promoted MCL-1 increase, while BCL-2 and BCL-xL levels remained mostly unchanged (Figure 16C). To explain the increase in BIM we studied its phosphorylation by the MAPK pathway. Trametinib caused a decrease in ERK1/2 phosphorylation, which in turn caused a decrease of BIM phosphorylation (Figure 17A). As previously described, dephosphorylation of BIM prevents its proteasomal degradation and causes its accumulation[293]. Finally, we also examined the expression of effector proteins to check if they were related to the mechanism of adaptation to trametinib treatment. In this cell line we could not detect the presence of BAX, but BAK underwent a non-significant increase when these cells were treated (Figure 17B). The changes in protein levels suggest that although trametinib had a proapoptotic action by increasing BIM levels, this activator protein was sequestered by antiapoptotic proteins, especially MCL-1.

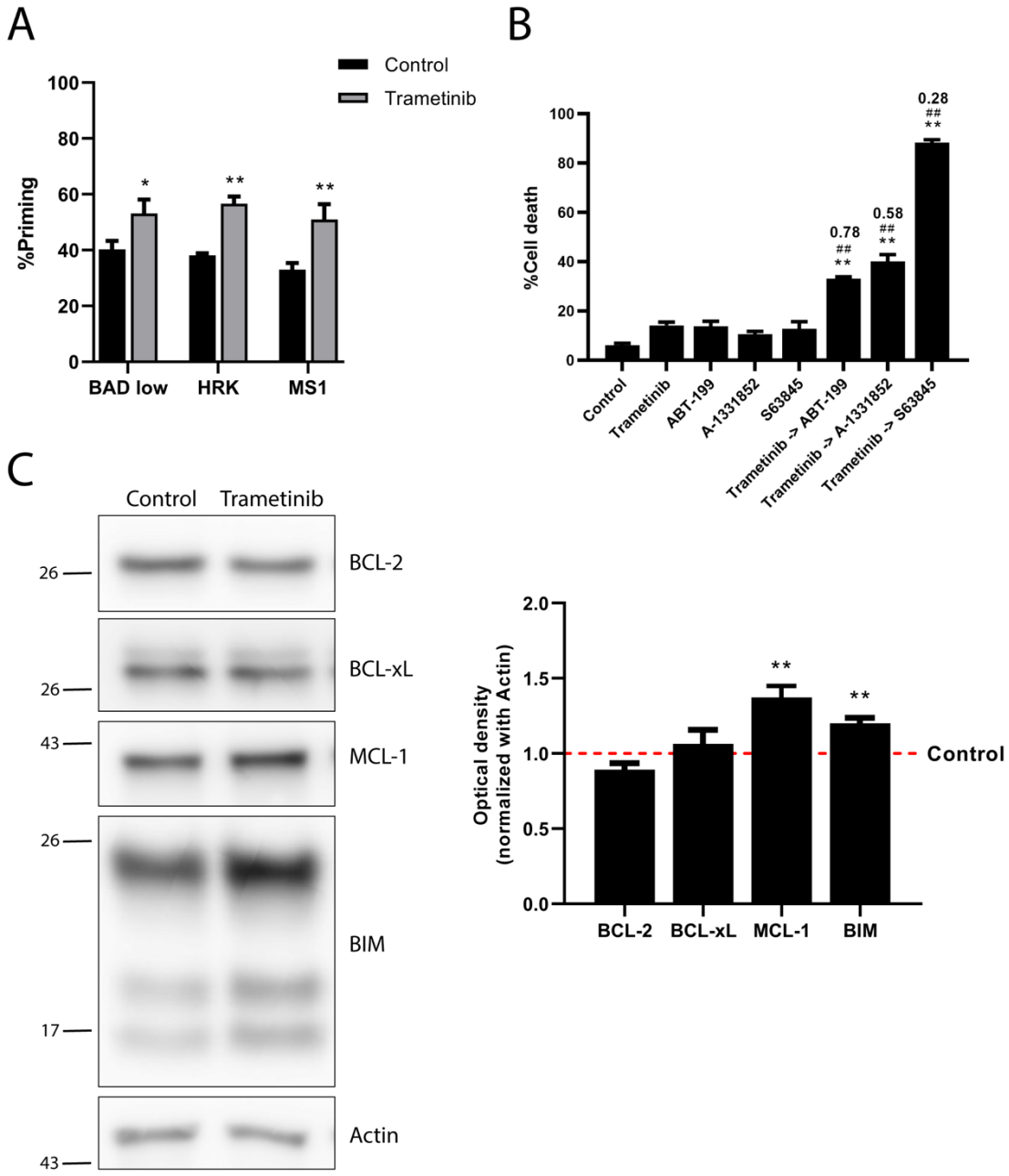


**Figure 16. Trametinib synergizes with S63845 in NALM-6 cells, increasing BIM and MCL-1 protein expression. A)** DBP results using sensitizer peptides to study antiapoptotic dependencies of BCL-2 and BCL-xL with BAD 0.1 µM, BCL-xL with HRK 100 µM and MCL-1 with MS1 10 µM after 16 h of incubation with trametinib 100 nM in the NALM-6 cell line. **B)** Cytotoxicity was assessed by Annexin V/DAPI staining after 96 h incubation with trametinib 100 nM, ABT-199 100 nM, A133 100 nM and S63845 1,000 nM in the NALM-6 cell line. BH3 mimetics were added 16 h after treatment initation. **C)** Western blot analysis for antiapoptotic and BIM proteins in NALM-6 cells after 16 h of treatment with trametinib 100 nM. Quantification of optical density for each protein was normalized to actin, and fold-change was calculated comparing to protein expression in the control condition. All results are expressed as the mean ± standard error of the mean (SEM) of at least three biologically independent replicates. Statistical significance was calculated using Student's t-test compared to control condition and considering *p < 0.05 and **p < 0.01. Significance was also calculated comparing combination conditions with both single agents and considering #p < 0.05 and ##p < 0.01. CI value is indicated on top of every combination where CI < 1 indicates synergy.

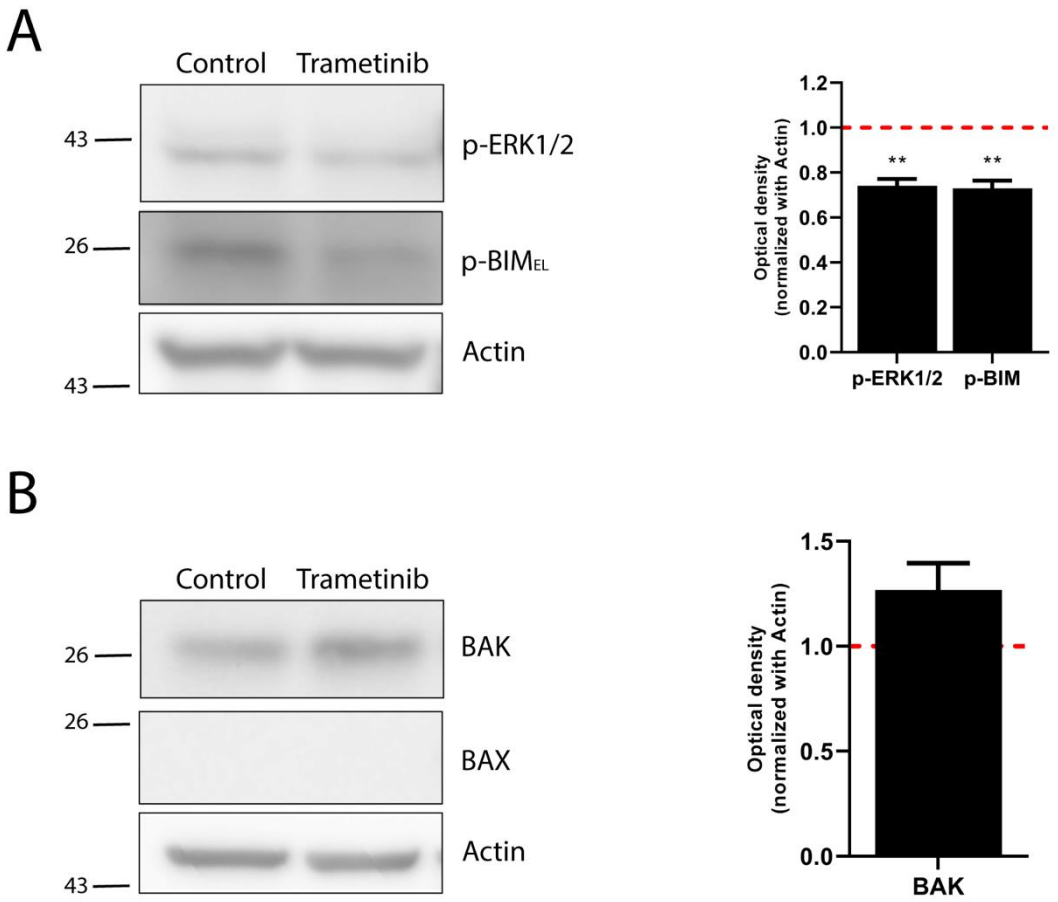


**Figure 17. Trametinib dephosphorylaze BIM protein and do not change effector protein levels. A)** Western blot analysis of phospho-ERK1/2 and phospho-BIM in NALM-6 cell line after 16 h of treatment with trametinib 100 nM. **B)** Western blot analysis of BAK and BAX in NALM-6 cell line after 16 h of treatment with trametinib 100 nM. Quantification of optical density for each protein was normalized to actin, and fold-change was calculated comparing to protein expression in the control condition. All results are expressed as the mean ± SEM of at least three biologically independent replicates. Statistical significance was calculated using Student's t-test compared to control condition and considering $*p < 0.05$ and $**p < 0.01$.

To demonstrate that MCL-1 mostly blocks the excess of BIM caused by trametinib treatment, we immunoprecipitated it and studied its interactions with other BCL-2 family members. We could efficiently pull down MCL-1 (Figure 18A) and studied the expression of these two proteins after trametinib, S63845 and the combination of both treatments. Not surprisingly, trametinib caused an increase in BIM, while the addition of S63845 caused the stabilization of MCL-1 (Figure 18B), as already described elsewhere[219,294]. When we studied their interaction, we could see a clear increase in the binding between these two proteins when cells were treated with trametinib. In contrast, when the MCL-1 specific inhibitor S63845 was added, the interaction with BIM was completely displaced (Figure 18C). This explains the synergy observed when combining trametinib and S63845, where the addition of the specific BH3 mimetic

displaces BIM to activate apoptosis, achieving over 80% of cell death (Figure 16B). Interestingly, when we combined trametinib with ABT-199 or A133 only a modest cytotoxic effect was observed (Figure 16B). Based on these findings, we conclude that MCL-1 is the main antiapoptotic protein that protects towards trametinib-induced apoptosis in NALM-6; and that BCL-2 and BCL-xL only play a minor role.

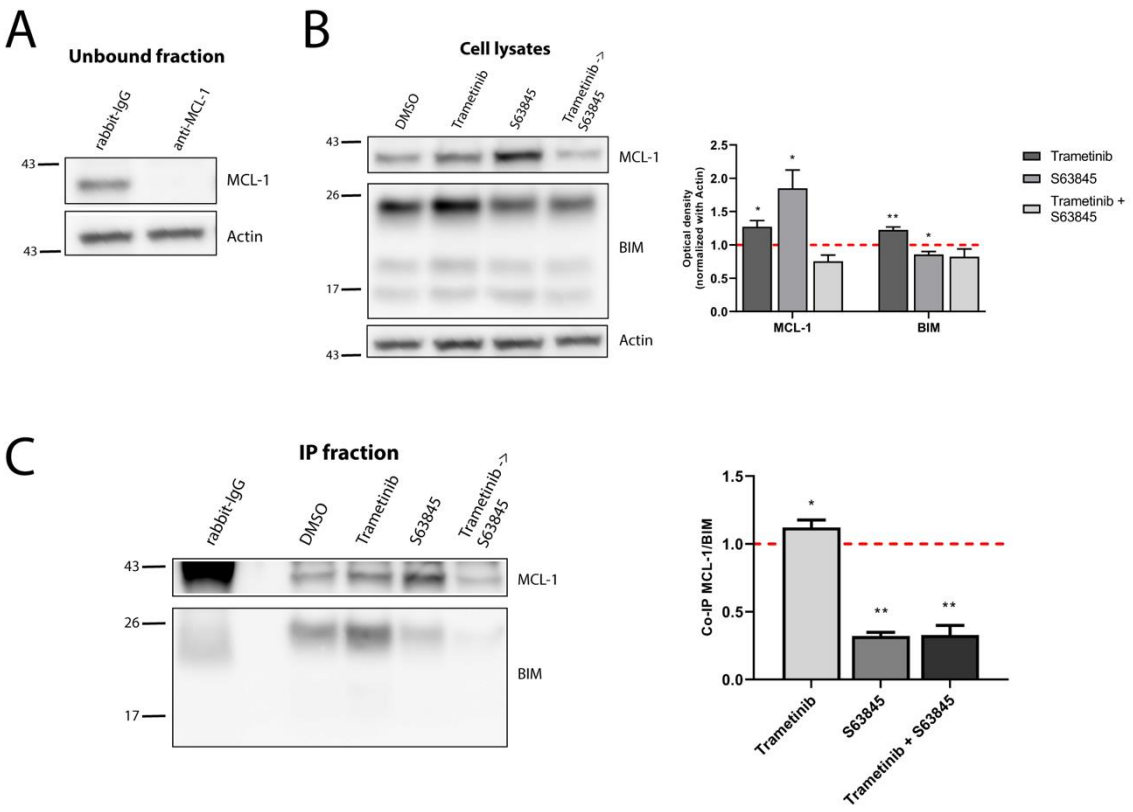


**Figure 18. Synergy of trametinib and S63845 in NALM-6 is explained by an increased interaction between MCL-1 and BIM. A)** Western blot analysis of the unbound fraction after MCL-1 immunoprecipitation. **B)** Immunodetection of MCL-1 and BIM initial expression in cell lysates after 16 h of incubation with trametinib 100 nM, and 2 h of incubation with S63845 1,000 nM in the specified conditions. Quantification of optical density for each protein was normalized to actin and fold-change was calculated comparing to protein expression in the control condition. **C)** Western blot of the immunoprecipitated fraction was used to study the interaction between MCL-1 and BIM after treatment with trametinib 100 nM and 2 h with S63845 1,000 nM. To quantify this binding, BIM optical density was normalized to MCL-1 optical density and fold-change was calculated comparing to protein expression in the control condition. All results are expressed as the mean ± SEM of at least three biologically independent replicates. Statistical significance was calculated using Student's t-test compared to control condition and considering *$p < 0.05$ and **$p < 0.01$.

### 4.2.3. BH3 mimetics can be used to reduce sunitinib dosing in the SEM cell line

Targeted therapies also have side effects in patients that worsen their quality of life. To reduce these risks, we aimed to decrease the concentration of sunitinib, which as

single agent produced around 60% of cell death in the SEM cell line at high concentrations (Figure 15C). By performing DBP, we found that sunitinib incubation enhanced BAD, HRK and MS1 sensitizer BH3 peptides priming, also suggesting a diversified antiapoptotic adaptation to this targeted therapy (Figure 19A). When we treated the cells with a 10-fold reduction in the concentration of sunitinib, aiming to diminish the potential secondary effects in the clinic, we observed that the efficacy of the treatment was also significantly reduced (Figure 19B). We also decreased the concentrations of the BH3 mimetics ABT-199 and S63845, as the concentrations normally used (100 nM and 1,000 nM respectively) also produced high cytotoxicity (data not shown). These drugs at lower concentrations killed less than 40% of the cells, but by combining sunitinib with the different BH3 mimetics we obtained a synergistic effect that boosted the efficacy of the low-dose treatment, especially when combining it with ABT-199 and S63845 (Figure 19B), as anticipated by DBP.

We studied the biological mechanism behind these combinations similarly as we did for the NALM-6 line and trametinib. Sunitinib treatment caused a significant increase in BIM protein expression (Figure 19C). But unlike the previous case, MCL-1 levels were significantly reduced, while BCL-2 slightly decreased, and BCL-xL remained unchanged (Figure 19C). Sunitinib produced a proapoptotic effect by increasing BIM, although the antiapoptotic protein expression could not explain why the increase in BIM did not cause an initiation of the apoptotic process. Sunitinib has been described as a treatment that affects the MAPK pathway in other types of cancer[295,296]. In fact, when we studied ERK1/2 and BIM phosphorylation in sunitinib-treated SEM cells we detected a significant reduction, explaining the accumulation of BIM by inhibiting its proteasomal degradation (Figure 20A). In contrast, BAK and BAX effector proteins remained constant after treatment (Figure 20B). These results showed a proapoptotic phenotype similar to the one described above, but a paradoxical adaptation is observed, since antiapoptotic proteins expression was reduced rather than increased.

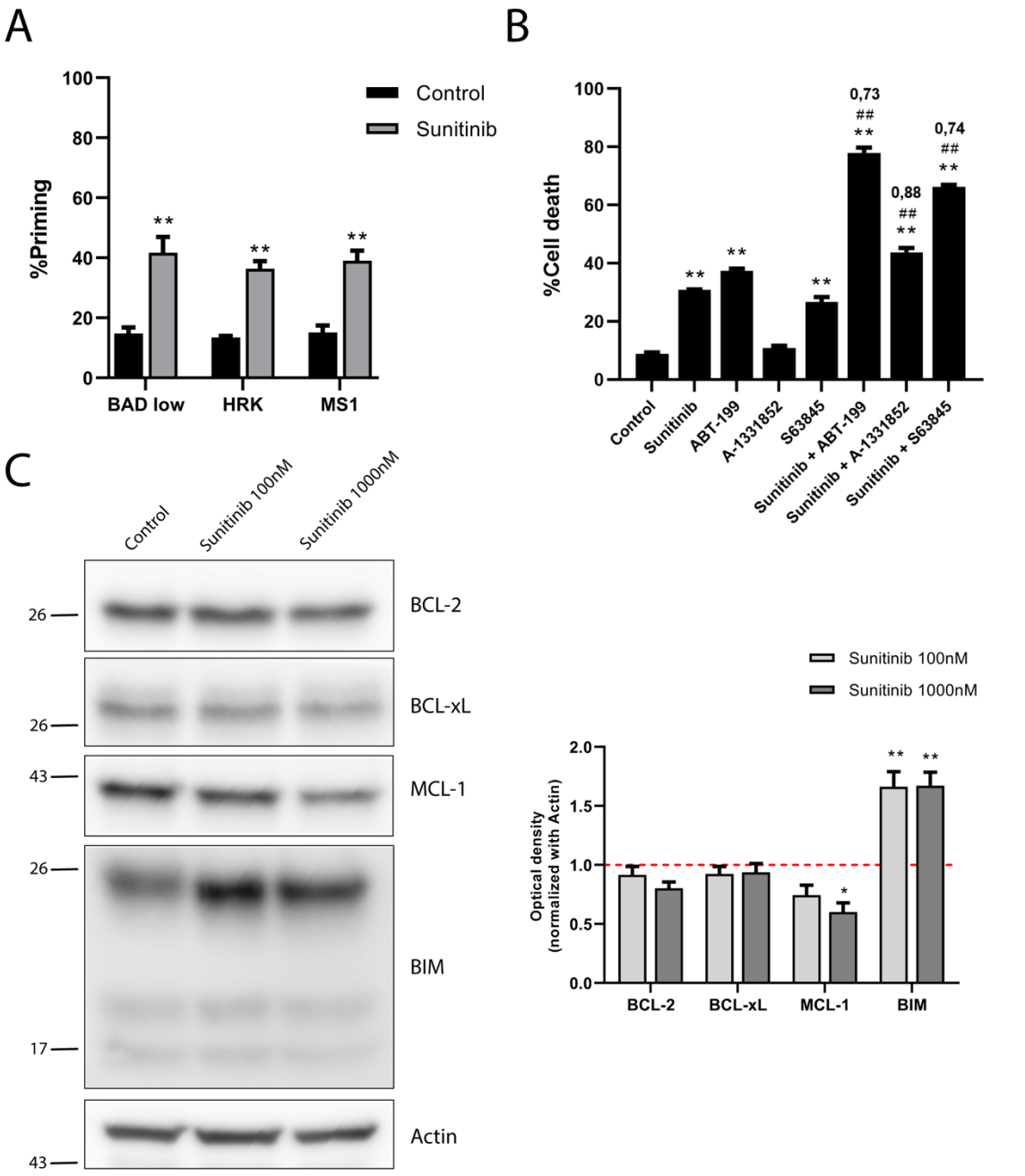


**Figure 19. Sunitinib synergizes with ABT-199 and S63845 in SEM cells but antiapoptotic proteins are downregulated. A)** DBP results using sensitizers peptides to study antiapoptotic dependencies of BCL-2 and BCL-xL with BAD 0.1 µM, BCL-xL with HRK 100 µM and MCL-1 with MS1 10 µM after 16 h of incubation with sunitinib 1,000 nM in the SEM cell line. **B)** Cytotoxicity assessed by Annexin V/DAPI staining after 96 h of sunitinib 100 nM, ABT-199 10 nM, A133 100 nM and S63845 100 nM exposure in SEM cells. BH3 mimetics were added 16 h after treatment initation. **C)** Western blot analysis for antiapoptotic and BIM proteins in SEM cells after 16 h of treatment with sunitinib 100 nM and sunitinib 1,000 nM. Quantification of optical density for each protein was normalized to actin, and fold-change was calculated comparing to protein expression in the control condition. All results are expressed as the mean ± SEM of at least three biologically independent replicates. Statistical significance was calculated using Student's t-test compared to control condition and considering *p < 0.05 and **p < 0.01. Significance was also calculated comparing combination conditions with both single agents and considering #p < 0.05 and ##p < 0.01. CI value is indicated on top of every combination where CI < 1 indicates a synergistic combination.

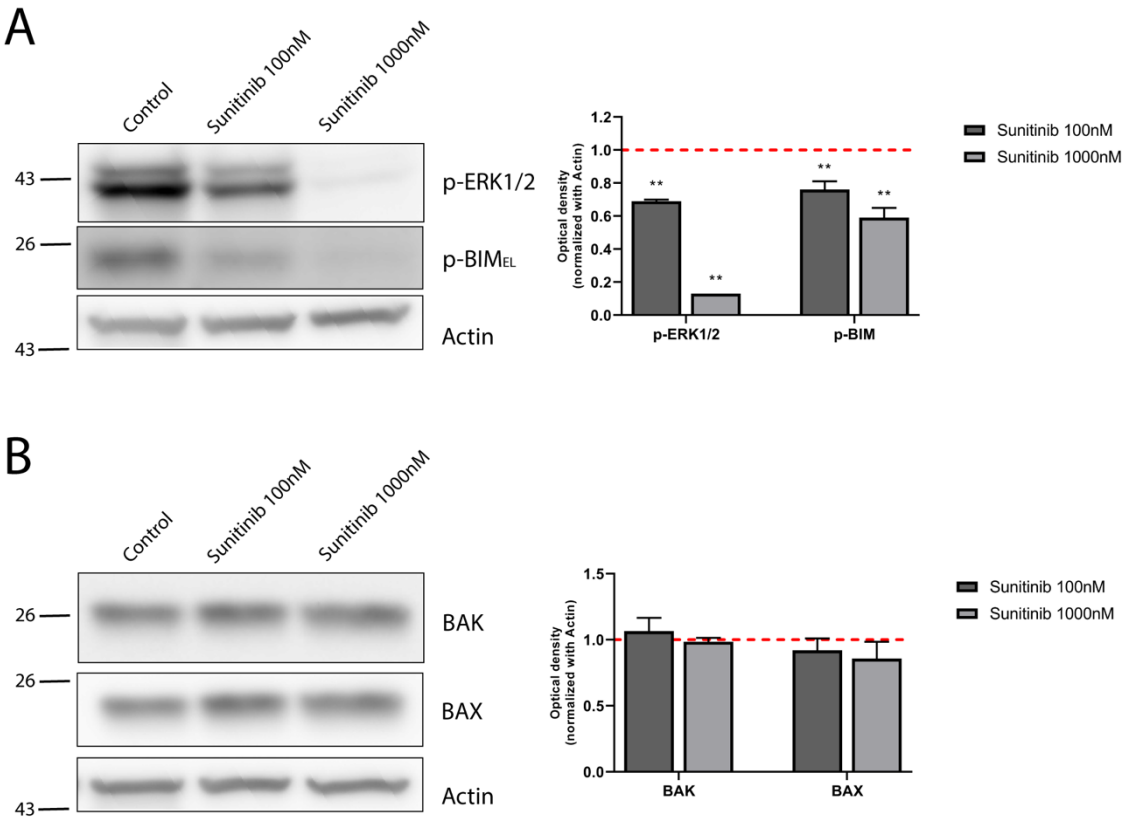


**Figure 20. Sunitinib induce dephosphorilation of ERK1/2 and BIM while not affecting effector BCL-2 proteins. A)** Western blot analysis of phospho-ERK1/2 and phospho-BIM in the SEM cell line after 16 h of treatment with sunitinib 100 nM and 1,000 nM. **B)** Western blot analysis of BAK and BAX in SEM cell line after 16 h of treatment with sunitinib 100 nM and 1,000 nM. Quantification of optical density for each protein was normalized to actin, and fold-change was calculated comparing to protein expression in the control condition. All results are expressed as the mean ± SEM of at least three biologically independent replicates. Statistical significance was calculated using Student's t-test compared to control condition and considering $*p < 0.05$ and $**p < 0.01$.

We then sought to study why these cells survive the increase in BIM, and we again immunoprecipitated MCL-1 to explore the combination of sunitinib and S63845 (Figure 21A). As we already observed in NALM-6 cells, treatment with S63845 caused a stabilization of MCL-1, while we still detected the increase in BIM caused by sunitinib (Figure 21B). When we studied the interaction between MCL-1 and BIM, we could observe that although total MCL-1 levels were reduced by the targeted agent, its binding to BIM increased to neutralize the excess of proapoptotic protein. Yet, when S63845 was added, the interaction between MCL-1 and BIM was disrupted and cell death restored (Figure 21C).

The combination of sunitinib and ABT-199 were also highly synergistic, so we studied the molecular mechanism underlying the effectiveness of this treatment combination by

immunoprecipitating BCL-2 (Figure 22A). Sunitinib treatment again slightly reduced BCL-2 levels and promoted BIM expression (Figure 22B). When we explored the interaction between BCL-2 and BIM, we observed a significant increase in their binding when the cells were treated with sunitinib. When ABT-199 was added, this interaction was blocked, and BIM was then released (Figure 22C). These results show that the increase in proapoptotic BIM caused by low-dose sunitinib is neutralized by BCL-2 and MCL-1. When either of these two proteins was inhibited with a specific BH3 mimetic, BIM was released to restore the apoptotic process because the remaining antiapoptotic proteins could not neutralize it.

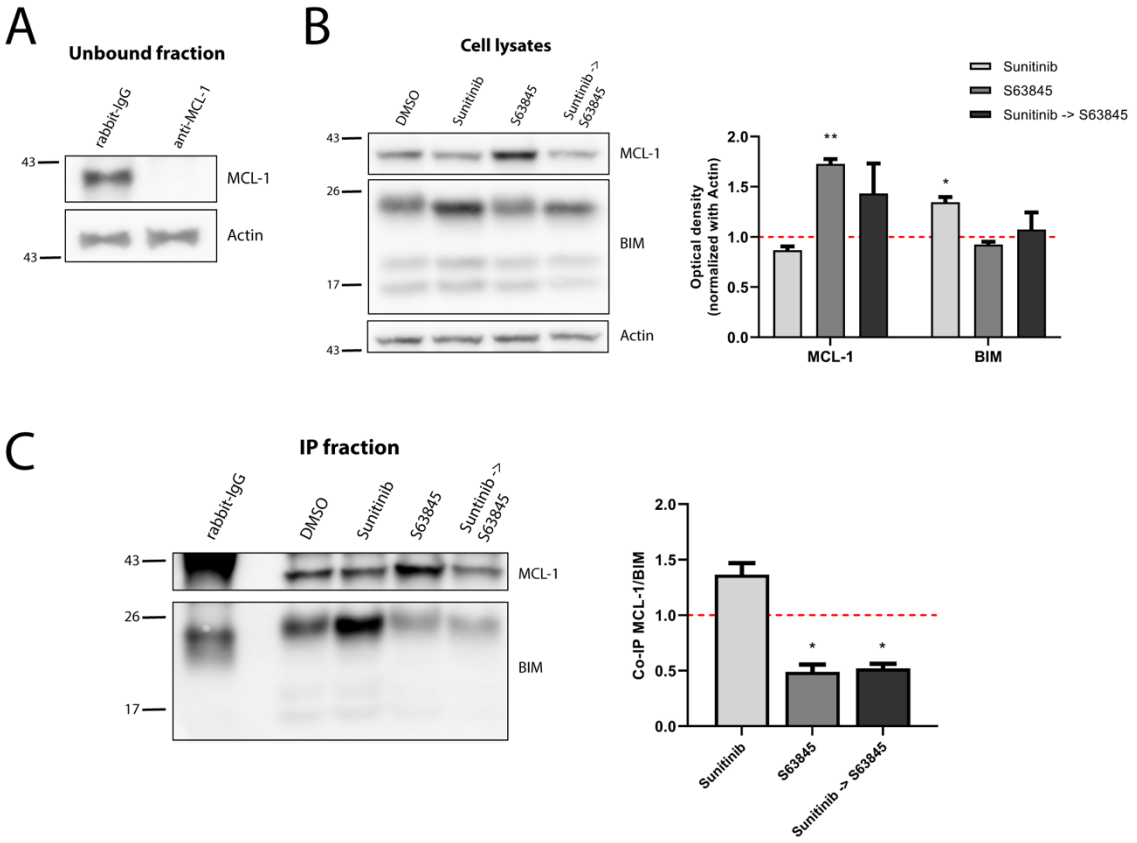


**Figure 21. Increased binding of BIM to MCL-1 causes sunitinib and S63845 synergism. A)** Western blot analysis of the unbound fraction after MCL-1 immunoprecipitation. **B)** Immunodetection of MCL-1 and BIM initial expression in cell lysates after 16 h of incubation with sunitinib 100 nM, and 2 h incubation with S63845 100 nM in the specified conditions. Quantification of optical density for each protein was normalized to actin and fold-change was calculated comparing to protein expression in the control condition. **C)** Western blot of the immunoprecipitated fraction was used to study the interaction between MCL-1 and BIM after treatment with sunitinib 100 nM and 2 h with S63845 100 nM. To quantify this binding, BIM optical density was normalized to MCL-1 optical density and fold-change was calculated comparing to protein expression in the control condition. All results are expressed as the mean ± SEM of at least three biologically independent replicates. Statistical significance was calculated using Student's t-test compared to control condition and considering *$p < 0.05$ and **$p < 0.01$.

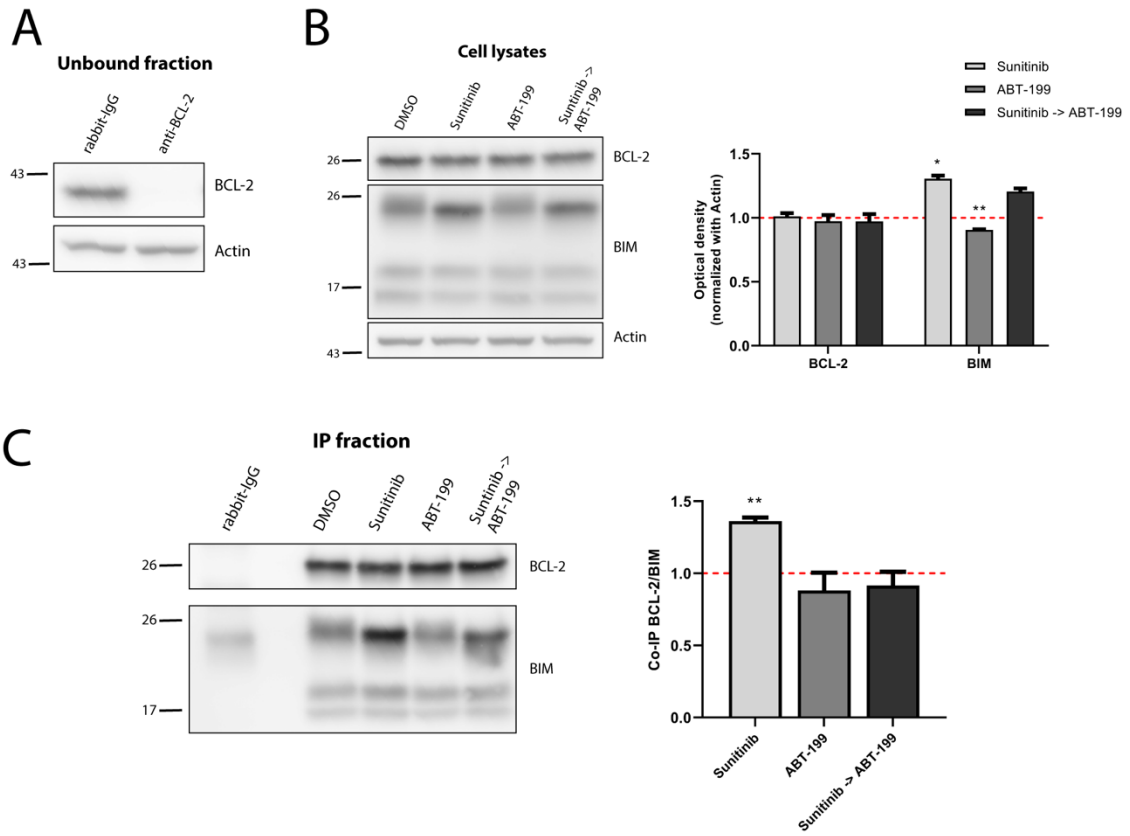


**Figure 22. BCL-2 binds to BIM after sunitinib treatment promoting synergy with ABT-199. A)** Western blot analysis of the unbound fraction after BCL-2 immunoprecipitation. **B)** Immunodetection of BCL-2 and BIM initial expression in cell lysates after 16 h of incubation with sunitinib 100 nM, and 4 h incubation with ABT-199 10 nM. Quantification of optical density for each protein was normalized to actin and fold-change was calculated comparing to protein expression in the control condition. **C)** Western blot of the immunoprecipitated fraction to study the interaction between BCL-2 and BIM after sunitinib 100 nM treatment, and 4 h with ABT-199 10 nM. To quantify this binding, BIM optical density was normalized to BCL-2 optical density and fold-change was calculated comparing to protein expression in the control condition. All results are expressed as the mean ± SEM of at least three biologically independent replicates. Statistical significance was calculated using Student's t-test compared to control condition and considering *$p < 0.05$ and **$p < 0.01$.

### 4.2.4. Pediatric BCP-ALL PDX recapitulates SEM antiapoptotic adaptations

In collaboration with the University of Ulm and the Dr. Seyfried, Prof. Debatin and Prof. Meyer we analyzed a PDX sample derived from a patient with the same genetic alteration as the SEM cell line (*KMT2A/AFF1*). We performed DBP analyses using the same targeted therapies tested in BCP-ALL *in vitro* models and we observed a similar response, with an increase in apoptotic priming with the BIM peptide after sunitinib treatment and, with a lesser extent, with trametinib (Figure 23). Interestingly, with

sensitizer peptides we detected similar antiapoptotic adaptations to those observed in the cell line, suggesting that the combination of sunitinib with ABT-199 or S63845 could be beneficial for this patient (Figure 23). We then analyzed by western blot the BCL-2 family proteins expression and observed a small reduction on MCL-1 and a clear increase of BIM (Figure 24). All these results demonstrate that the same effective combinations identified in cell lines could be applied to patients with a similar genetic background, as we obtained the same predictions with DBP in a PDX mouse model. Since we cannot perform cytotoxicity studies with PDX-isolated cells because of their *ex vivo* decay, DBP would allow the functional identification of potential treatments.

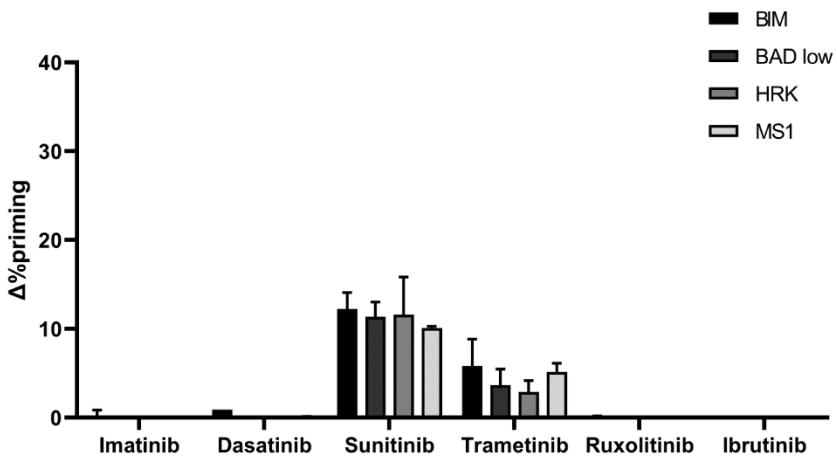


**Figure 23. PDX cells presenting KMT2A rearrangement show a similar DBP profile as the SEM cells.** DBP with BIM BH3, BAD BH3, HRK BH3, and NOXA BH3 peptides after 16 h of incubation with 1,000 nM imatinib, 100 nM dasatinib, 1,000 nM sunitinib, 100 nM trametinib, 100 nM ruxolitinib and 1,000 nM ibrutinib in PDX cells. Δ%priming stands for the difference in %priming between treatment and control condition. All results are expressed as the mean ± standard deviation of two technical replicates.

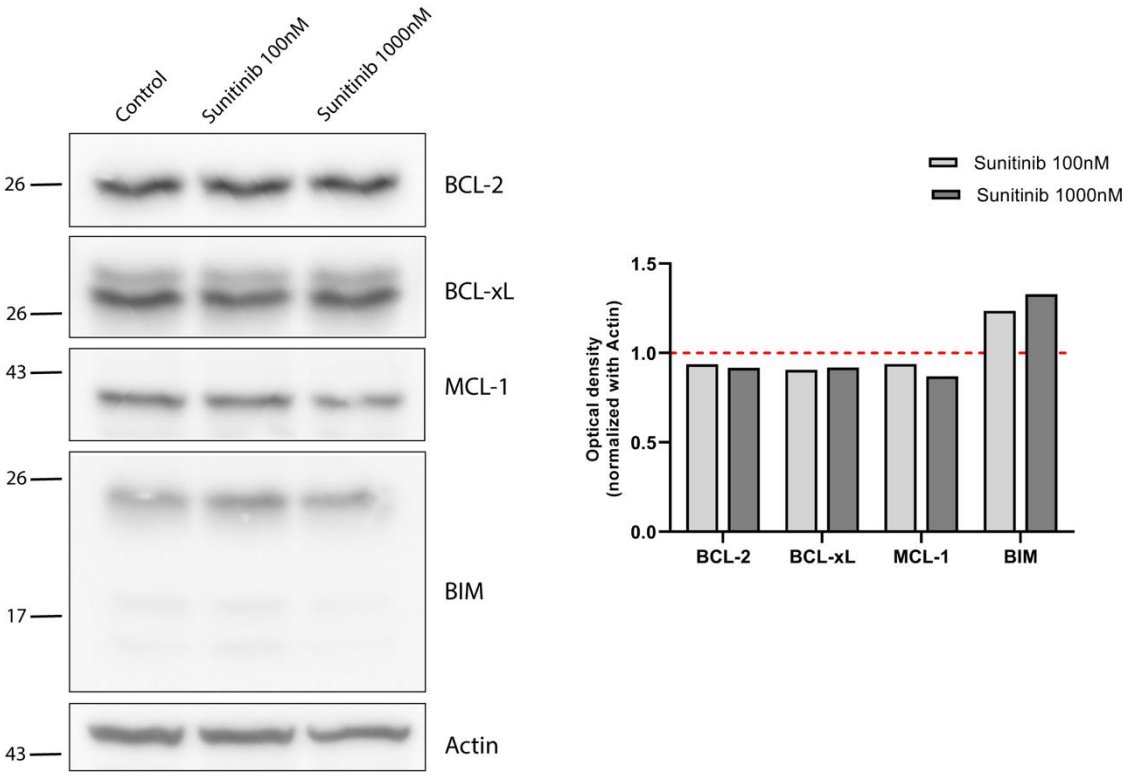


**Figure 24. BCL-2 family of proteins expression in BCP-ALL PDX cells after sunitinib treatment.** Western blot analysis for antiapoptotic and BIM proteins in BCP-ALL PDX cells after 16 h of treatment with sunitinib 100 nM and sunitinib 1,000 nM. Quantification of optical density for each protein was normalized to actin, and fold-change was calculated comparing to protein expression in the control condition.

## 4.3. Venetoclax is effective in refractory and relapsed primary samples

In collaboration with several pediatric oncologists, especially Dr. Manuel Ramirez from the Hospital Niño Jesús in Madrid, we analyzed several samples from relapsed patients that did respond to treatment. Several hospitals sent us cryopreserved mononuclear cells isolated from peripheral blood or bone marrow aspirates. We then thawed and exposed these primary cells for 16 hours to different treatments that clinicians could potentially administer as compassionate drug use. These samples were not from BCP-ALL patients, that typically present a good therapeutic response, but two T-cell ALL (patients 1 and 2), two undifferentiated leukemia (patients 3 and 5) and two AML (patients 4 and 6) cases.

In all cases, sufficient viable cells were obtained to perform the DBP assay without any major problems. Not surprisingly, most treatments did not show a great efficacy, as we were analyzing relapsed patient samples. However, bortezomib, a proteasome inhibitor, showed efficacy in patients 1, 3 and 5 (Figure 25A) at low concentrations. This treatment, although it has shown efficacy *in vitro* and *in vivo* in several types of hematological cancers[297], has been associated with high toxicity to healthy cells which hampers its use in the clinic. Patient 1 also showed sensitivity to idarubicin, while patient 6 responded to mitoxantrone (Figure 25A), two chemotherapeutics that are not usually used in the treatment of these type of tumors but could be included as compassionate drug use. Importantly, we observed a generalized response to venetoclax, which has been approved for treating pediatric AML patients and has demonstrated a great efficacy in other types of childhood leukemia. In all cases, venetoclax induced an increase in apoptotic priming, although the response varied among samples. For example, in patients 1 and 6 the increase was moderate, while in patients 2, 3 and 4 venetoclax was highly effective (Figure 25B). Other treatments were also tested following oncologists' suggestions. Overall, these results demonstrate that DBP could be used to identify which patients would benefit from experimental therapies, allowing a rapid turnover to inform clinicians who can then decide the best treatment.

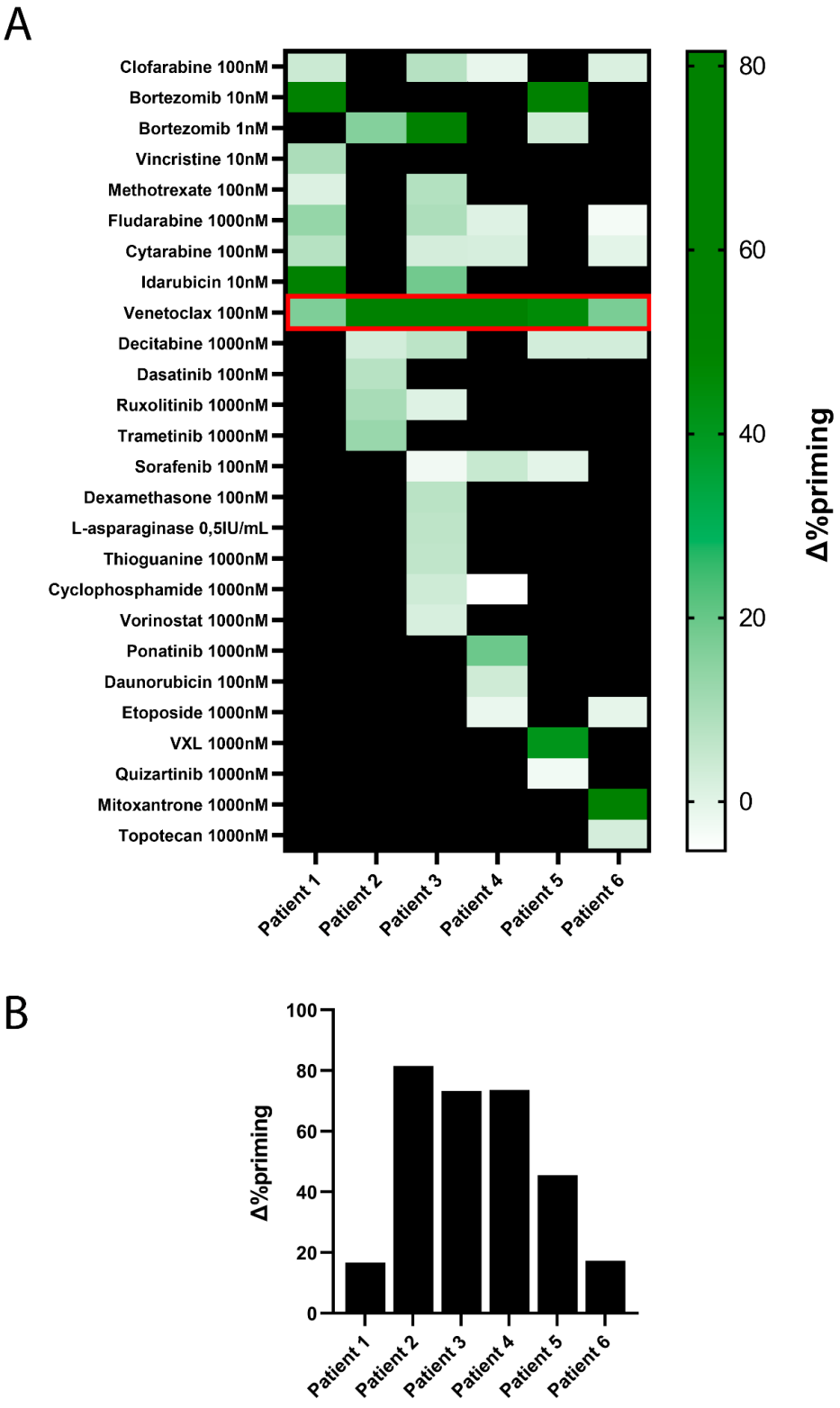


**Figure 25. Identification by DBP of last opportunity treatments in primary samples of pediatric leukemia patients. A)** Heatmap of the DBP results with BIM peptide after 16 hours of incubation with the different suggested treatments in 6 different primary samples from pediatric leukemia patients. **B)** Graph bar with the DBP results of the same samples after treatment with 100 nM of venetoclax for 16 hours. Δ%priming stands for the difference in %priming between treatment and control condition.

Since DBP is not yet approved as a companion diagnostic for childhood cancers, we could only inform pediatric oncologists that decided the treatment based on all the information that they had. Nonetheless, we followed the patients' progress to see if our predictions correlated with the clinical response, which we summarized in Table 5. In the case of patient 1, bortezomib was included in a chemotherapeutic combination, but the patient's disease was so advanced that did not survive these new rounds of treatment. Patient 2 suffered complications that prevented any further treatment strategy. But in patients 3 and 4 venetoclax was added to the treatment schedule following DBP predictions. Both patients reached full remission status one month after starting the treatment with venetoclax, proving that our functional predictions were correct. Patient 5 could not wait for the results of the functional assay and was treated with a combination of dexamethasone, cytarabine and vincristine. Although he managed to reach complete remission with this pulse of chemotherapy, within a few weeks he suffered a very aggressive relapse and did not survive. In this case we hypothesize that the inclusion of bortezomib or venetoclax, identified as effective treatments by DBP, could have helped to avoid the aggressive outcome. Finally, although the response to venetoclax in patient 6 was moderate, the clinicians decided to add it to gemtuzumab ozogamicin. The treatment started recently, so we do not have yet the results of the treatment outcome. Although we are currently limited by the number of patients analyzed, these results indicate that functional screenings, such as DBP, could help identify the best treatment and improve cancer treatment. In these initial assays, several patients have achieved a complete remission, pointing to the potential use of DBP to select compassionate drug use, like venetoclax.

| Patient | Treatment after DBP | Treatment outcome |
|---|---|---|
| Patient 1 | Dexamethasone, vincristine, mitoxantrone, intrathecal and bortezomib (28/07/2020) | Deceased (24/09/2020) |
| Patient 2 | Not applied | Deceased before treatment |
| Patient 3 | Venetoclax, fludarabine and cytarabine (13/12/2021) | Complete remission (04/01/2022) |
| Patient 4 | Venetoclax and FLAG-Ida (April 2022) | Complete remission (20/05/2022) |
| Patient 5 | Dexamethasone, vincristine and cytarabine | Complete remission but aggressive relapse and deceased (12/05/2022) |
| Patient 6 | Venetoclax and gemtuzumab ozogamicin | Not known |

**Table 5.** Summary of the treatments used after the functional assay and patients' outcome.

# Chapter V

## Development of a microfluidic-based dynamic BH3 profiling

This part of the thesis is based on a manuscript in revision: “Manzano-Muñoz A, Yeste J, A. Ortega M, Martín F, López A, Rosell J, Castro S, Serrano C, Samitier J, Ramón-Azcón J, Montero J. Microfluidic-based dynamic BH3 profiling predicts anticancer treatment efficacy for functional precision medicine. *Manuscript submitted.*”

As discussed above, one of the main limitations of DBP is the number of viable cells required to perform the assay, and simply many solid tumor biopsies cannot be analyzed. To solve this problem, we sought to develop a microfluidic-based DBP (µDBP) to decrease the number of cells needed to do the assay and to automate the process so that it can be easily implemented in the clinic. In this new protocol we replaced the cytochrome c antibody staining by fluorescent dyes to identify cell viability and mitochondrial permeabilization, which also reduced the time necessary to perform the assay and allowed continuous cell tracking by fluorescence microscopy (Figure 26).

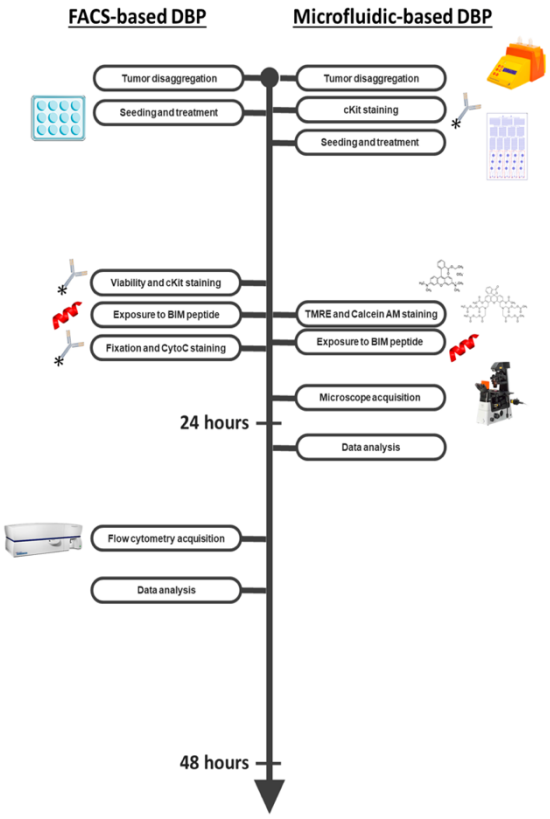


**Figure 26. The microfluidic-based protocol is faster than FACS-based DBP.** Side-by-side representation of all the steps in the FACS-based DBP (left) and the new microfluidic-based DBP (right).

## 5.1. FACS-based DBP identifies effective treatments in gastrointestinal cancer cell lines

To develop this new technology, we decided to use two GIST cell lines as our experimental models. GIST-T1 cells present a mutation in *KIT* and are sensitive to imatinib[298], while the GIST-T1/670 have a secondary mutation in *KIT* that confers resistance to this small molecule[299]. We first characterized the response of these two cell lines to imatinib and gefitinib, the latter was used as a negative control. As detailed in previous sections, we performed FACS-based DBP after 16 hours of treatment with these two inhibitors, then exposed them to increasing concentrations of BIM peptide and measured the induction of MOMP. GIST-T1 cells treated with imatinib had a different response to BIM peptide as cytochrome c was released at lower concentration of the peptide, indicating increased apoptotic priming caused by the treatment. In contrast, gefitinib, an EGFR inhibitor that has no effect on these cells, produced a similar curve as the control cells (Figure 27A). In contrast, the GIST-T1/670 cell line initially responded to lower concentrations of BIM. But none of the treatments shifted the BIM dose-response curve, indicating that they did not affect priming in this cell line (Figure 27B). In summary, FACS-based DBP identified an increase in apoptotic priming in imatinib-treated GIST-T1 cells, whereas no changes were observed in the other conditions (Figure 27C). We then tested these FACS-based DBP predictions performing a cell death assay, and we confirmed that the only treatment that induced apoptosis after 96 hours of incubation was imatinib in the GIST-T1 cell line (Figure 27D).

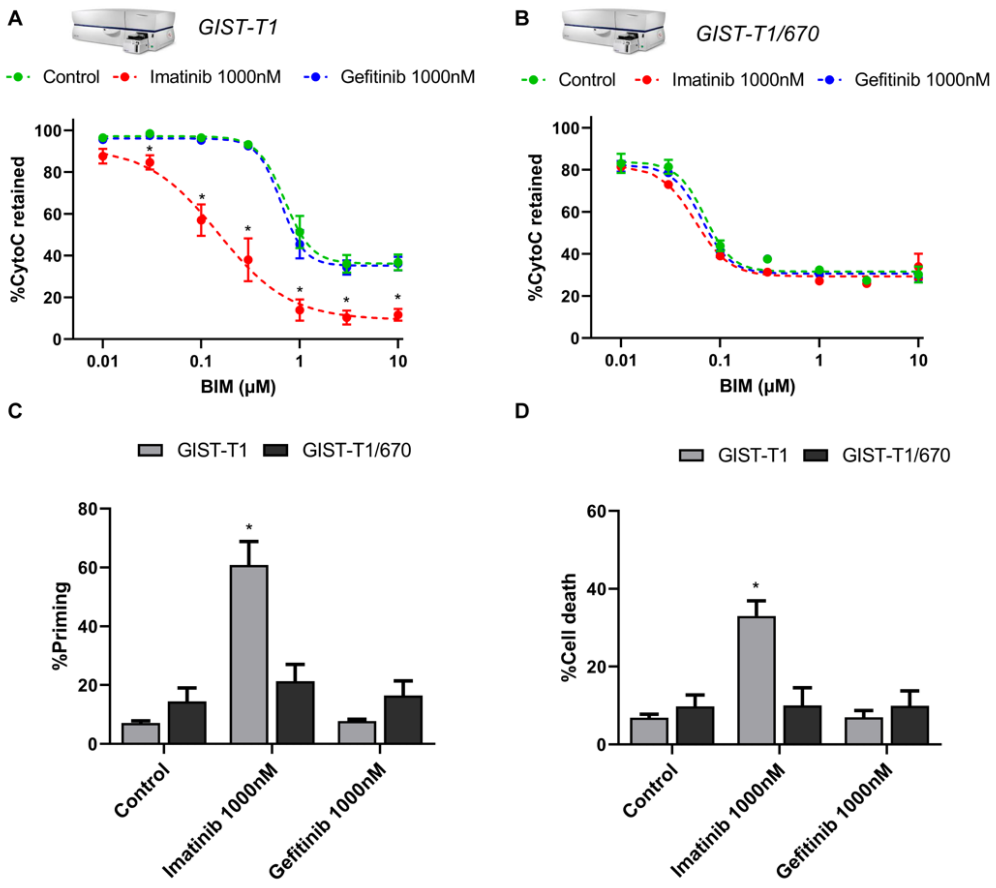


**Figure 27. FACS-based DBP identifies imatinib as an effective treatment in GIST-T1 cell line. A)** GIST-T1 and **B)** GIST-T1/670 FACS-based DBP curves after incubation for 16 hours with DMSO, imatinib and gefitinib. Results are represented as the percentage of cells with cytochrome c retained inside the mitochondria after incubation with increasing concentrations of BIM peptide. **C)** Quantification of % priming (percentage of cells with cytochrome c scape) in GIST-T1 and GIST-T1/670 cells. Values were chosen in the BIM peptide condition where the control cells started to engage MOMP and lose cytochrome c staining. **D)** Cytotoxicity was measured as % cell death using AnnexinV/PI staining. GIST-T1 and GIST-T1/670 cells were treated for 72 hours with DMSO, imatinib and gefitinib. All results are expressed as the mean ± S.E.M. of at least three biologically independent replicates. * indicates a p-value < 0.05.

## 5.2. Characterization of the microfluidic-based DBP

### 5.2.1. Development of the microfluidic device

In collaboration with Dr. Jose Yeste, Dr. Maria Alejandra Ortega and Prof. Javier Ramón from the Biosensors for Bioengineering group at the IBEC we developed a microfluidic chip with the aim to identify effective anticancer treatments with fewer cells. We hypothesized that this improvement would allow the use DBP on small solid tumor biopsies or even samples obtained from non-invasive techniques such as fine-needle aspirates or core-needle biopsies. In addition, the microfluidic device would allow to

automatically obtain the BIM peptide titration needed to perform the assay, automatizing the process, and avoiding the requirement for specialized personnel. The device consisted of a network of mixers formed by 100 um x 100 um microfluidic channels in serpentine with two inlets where the buffer and the peptide solution were introduced. The five different concentrations were dispensed into three independent wells of 4 mm diameter where the cancer cells were seeded. This design allowed the seeding of control cells and two different treatments that could be exposed to 5 different concentrations of BIM peptide (Figure 28A). Using finite elements method software, the distribution of the peptide along the chip was numerically calculated. Simulations showed that the microfluidic device generated a linear gradient with concentrations of 1, 0.75, 0.5, 0.25 and 0 relative to the concentration applied in one of the inlets (Figure 28B).

The proper generation of these dilutions depends on the mixers size, fluid velocity, and diffusion coefficient of the molecule. To verify that the microfluidic chip performed accordingly to the simulations and the network of mixers were properly fabricated, we perfused fluorescein through one of the inlets and transparent buffer through the other. Since the chip was made of glass and PDMS, which are transparent, we could take fluorescence images of the entire chip, identifying the concentration of fluorescein at each point of the microfluidic channels by measuring the intensity of the fluorescent dye (Figure 28C). When we focused in one of the T-junctions where two channels met, we could observe that the laminar flow caused a homogenization of the two fluids when entering the new channel (Figure 28D). Furthermore, by studying the performance of the fluids inside the new channel, we could observe that by diffusion the two solutions were fully mixed in less than 40 mm (Figure 28E), ensuring that in the new T-junction we had a perfect mixing of the two initial solutions since the serpentine was longer than 190 mm. To fully certify that the concentration generated by our device was correctly produced, we perfused a solution with blue dye and BSA through one inlet, and water through the other one. By collecting the solutions coming out of the wells and measuring the amount of blue dye and protein using colorimetric techniques, we could observe that the obtained gradient of concentrations correlated with the simulations, without variations among different chips, thus demonstrating the technical reproducibility between devices (Figure 28F).

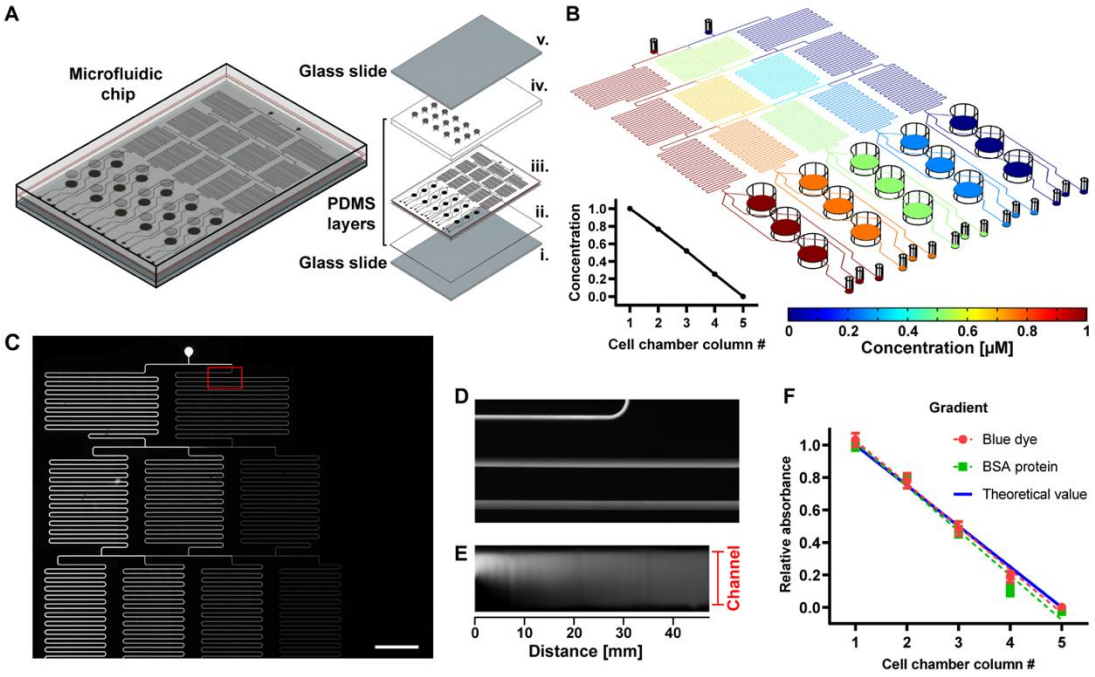


**Figure 28. Microfluidic dynamic BH3 profiling platform. A)** Schematic representation of the chip including exploded view of all the parts: i) lower glass slide, ii) thin PDMS layer, iii) channels & chambers PDMS layer (1 mm thick), iv), chambers PDMS layer (2 mm thick), and v) upper glass slide. **B)** Simulation of peptide concentration along with the whole microfluidic platform. The coordinate of the slice plot is selected at the middle of the microfluidic channels. Relative concentration as a function of the cell chamber (inset figure). **C)** Fluorescence image of the network of microfluidic channels after injecting fluorescein in the left inlet and distilled water in the right inlet at a pressure of 100 mbar. **D)** Zoomed view of the region where both solutions are mixed. **E)** Fluorescence intensity along with the first 47 mm of the mixer channel (total channel length is ~190 mm); Note that the image was processed in ImageJ to be plotted as a straight channel. **F)** Colorimetric detection of BSA protein and relative absorbance of blue dye at the outlets of the chip measured at 562 and 640 nm, respectively, on a plate reader. Together with the blue dye, BSA protein was injected through one of the inlets, while MiliQ water was injected in the other (inlet pressure of 200 mbar). Data represent 3 independent experiments using different chips.

Finally, we studied the inside the wells. Importantly, we needed the different peptide solutions to homogenously diffuse throughout each well, which was fully achieved after 19 minutes of perfusion (Figure 29A-D). Moreover, we had to avoid potential cell damage due to mechanical stress caused by the flow, so the microfluidic channels were placed 1 mm above the surface, preventing any unwanted pressure on the cells. Altogether, these results demonstrate that our microfluidic platform met the requirements for µDBP.

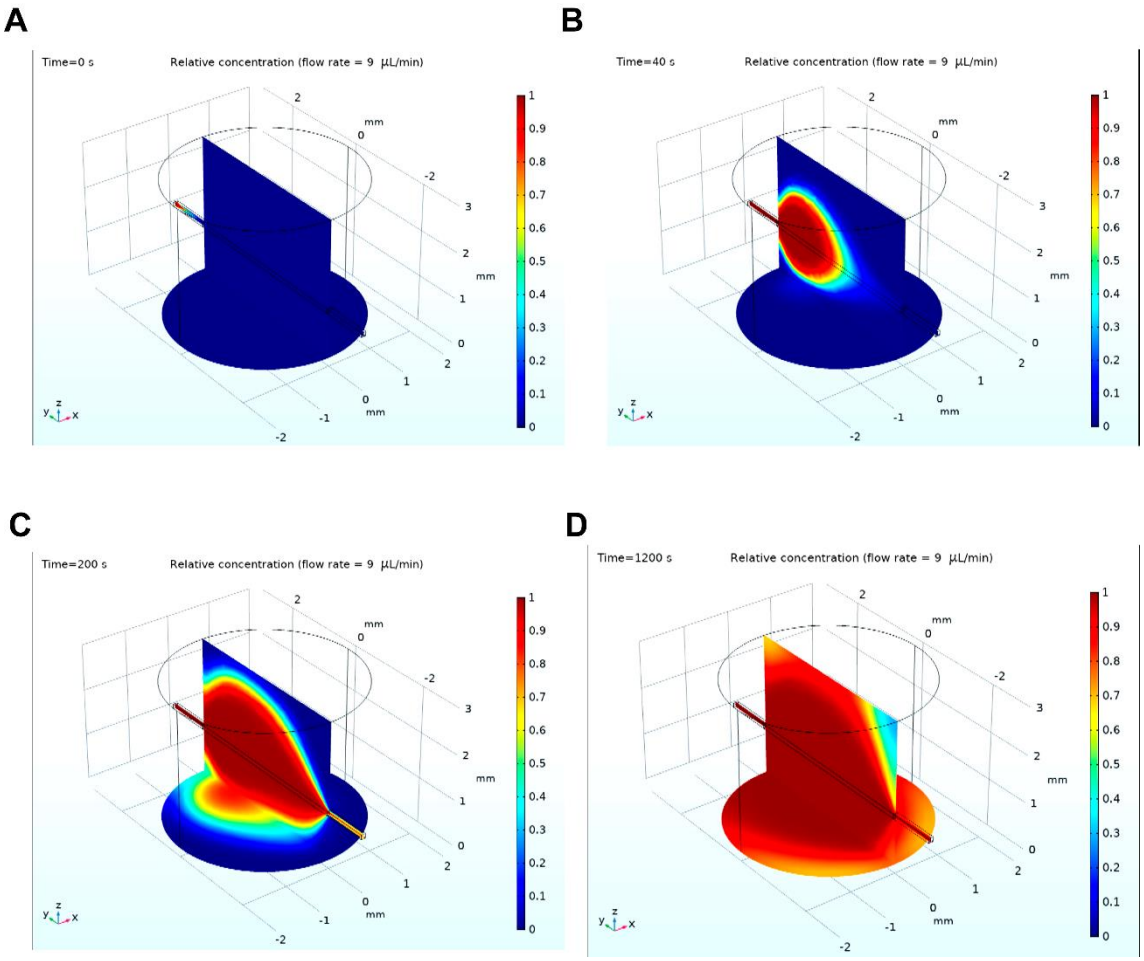


**Figure 29. Multiphysics simulations allow to study the distribution of liquid inside the cell chambers.** Theoretical estimation of the peptide distribution with the experimental conditions over time in the cell chamber using COMSOL after **A)** 0 seconds, **B)** 40 seconds, **C)** 200 seconds and **D)** 1200 seconds.

### 5.2.2. Fluorescent readout for DBP

FACS-based DBP uses cytochrome c immunostaining to identify apoptotic induction in cancer cells, which prolongs the time required to perform the assay. To avoid this limiting step and make the assay compatible with fluorescence microscopy, we used TMRE, a cationic dye that accumulates in healthy mitochondria and loses its fluorescence when MOMP is engaged. To further optimize this apoptotic marker for our device we used the two GIST cell models. We seeded the cancer cells on 96-well plates and treated them with imatinib and gefitinib for 16 hours. Before using the BIM peptide, we stained them with TMRE and calcein AM (a viability marker). The cells were then exposed to increasing concentrations of BIM peptide for two hours and we acquired fluorescence images in the green field (alive cells) and in the red field (apoptotic marker). In the GIST-T1 cell line we were able to identify alive cells thanks to

calcein AM staining. In the untreated condition we saw that the red TMRE signal decreased as the concentration of BIM peptide increased, indicating that we could potentially use it to identify apoptosis induction. Cells treated with imatinib lost TMRE intensity at a lower BIM peptide concentration, correlating with the increase in apoptotic priming previously observed with FACS-based DBP. However, cells treated with gefitinib showed a similar fluorescent pattern as the control cells (Figure 30A). In the GIST-T1/670 cell line we could also identify alive cells and induction of MOMP in response to BIM, but none of the treatments induced any significant shift, thus indicating unchanged apoptotic priming (Figure 30B).

To quantify these results, we used the viability marker field (calcein AM) to automatically identify all alive cells. For each cell, the mean intensity of TMRE was quantified, applying a threshold based on the untreated control condition to differentiate between cells with positive and negative signal (non- apoptotic and apoptotic cells, respectively). With this data we could construct BIM dose-response curves, similarly as we previously did using FACS-based DBP. In GIST-T1 cells we obtained an apoptosis induction curve in the control condition, which was shifted to the left (more responsive to BIM, increase in priming) when these cells were treated with imatinib, but not with gefitinib (Figure 30C). As expected, in GIST-T1/670 cells we also obtained a response curve to BIM, but in this case no treatment shifted it (Figure 30D). The amount of apoptotic priming was quantified as the difference of TMRE negative cells comparing treated and untreated cells. In summary, the only experimental condition that caused an increase in apoptotic priming was imatinib treatment in GIST-T1 cells (Figure 30E), correlating with FACS-based DBP. Therefore, these results demonstrate that TMRE can be used to generate a fluorescence microscopy dose-response curve, that could be applied in our DBP microfluidic device analyses.

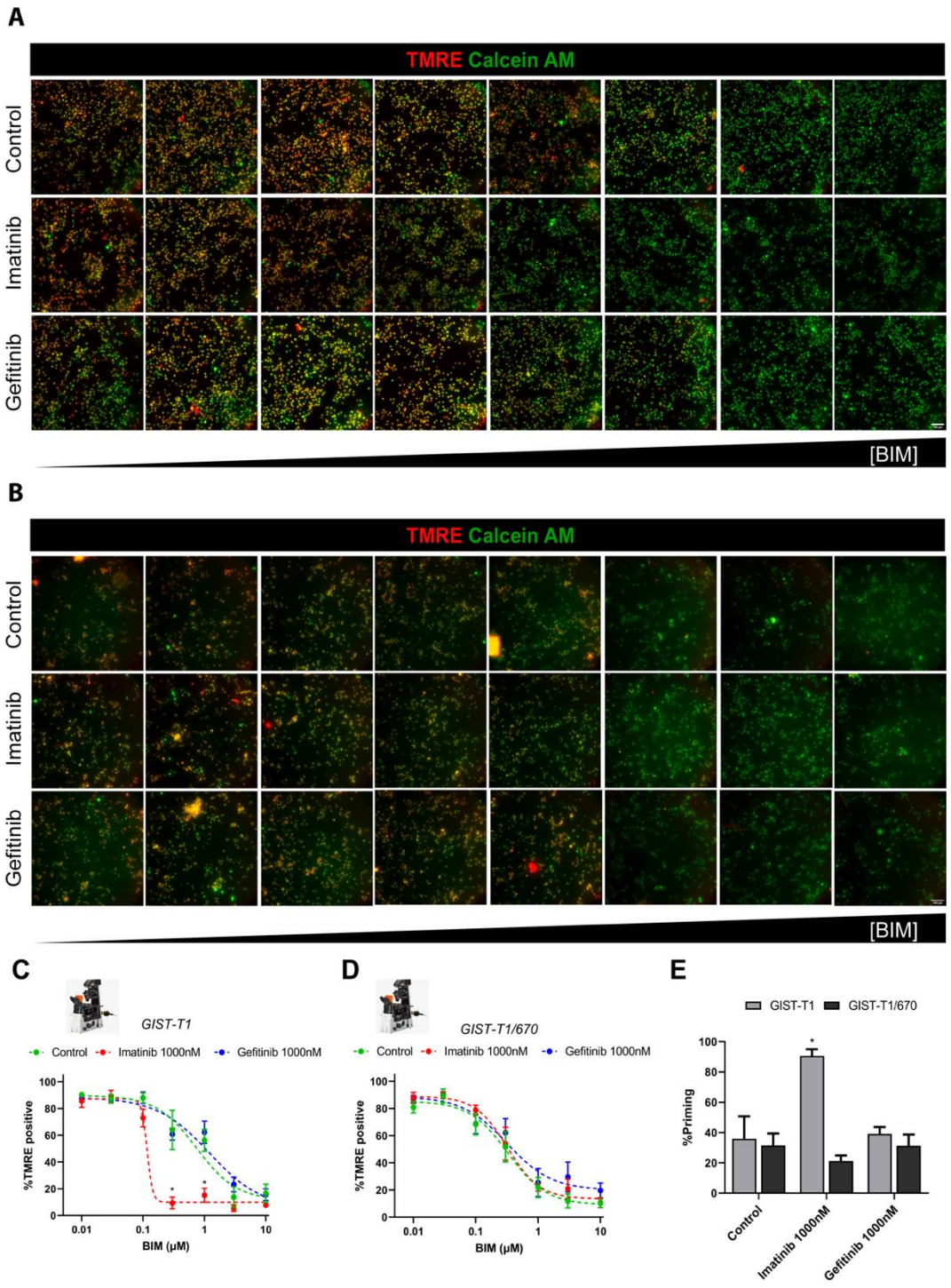


**Figure 30. TMRE can be used to generate the dose-response curves required to perform DBP.** Visualization of **A)** GIST-T1 cells and **B)** GIST-T1/670 cells seeded in a 96-well plate after treatment with DMSO, imatinib and gefitinib for 16 hours and exposure to increasing concentrations of BIM peptide. Alive cells are marked in green and TMRE (red field) is used to identify apoptotic from non-apoptotic cells. Scale bars, 100 μm. **C)** GIST-T1 and **D)** GIST-T1/670 microscopy-obtained curves after incubation for 16 hours with DMSO, imatinib and gefitinib. Results are represented as the percentage of cells with positive TMRE signal after incubation with increasing concentrations of BIM peptide. **E)** Quantification of %priming (percentage of cells with negative TMRE signal) in GIST-T1 and GIST-T1/670 cells. Values were chosen in the BIM peptide condition where the control cells started to engage MOMP and lose TMRE staining. All results are expressed as the mean ± S.E.M. of at least three biologically independent replicates. * indicates a p-value < 0.05.

## 5.3. Microfluidic-based DBP can identify effective treatments in different GIST models

### 5.3.1. Development of the microfluidic-based DBP using GIST cell lines

After characterizing the device performance and the readout method, we integrated the whole process to perform the complete assay inside the microfluidic chip. We seeded GIST cells in different cell chambers and treated them with imatinib and gefitinib for 16 hours. After the incubation, we labelled the cells with TMRE and calcein AM using the two inlets simultaneously to perfuse the staining solution. Then, we used the concentration gradient generator to expose the cells to a different concentration of BIM peptide in each column of wells. The gradient was generated by applying MEB buffer with digitonin through one inlet, while the same buffer with the maximum desired concentration of BIM peptide through the other inlet. After the required peptide incubation, fluorescence images were taken from all cell chambers. Similarly to the experiments performed in well plates, using the calcein AM green fluorescence we were able to identify alive cells and we observed that the intensity of TMRE decreased as the concentration of BIM increased. In imatinib-treated cells, the red signal decreased at a lower BIM concentrations compared to untreated cells, whereas in the case of gefitinib no significant changes were observed (Figure 31A). When we repeated the experiments with the resistant cell line GIST-T1/670, we detected a loss of TMRE intensity at the same BIM concentration in the three different conditions (Figure 31B). Thus, as expected, we conclude that none of the treatments primed the GIST-T1/670 cells for apoptosis.

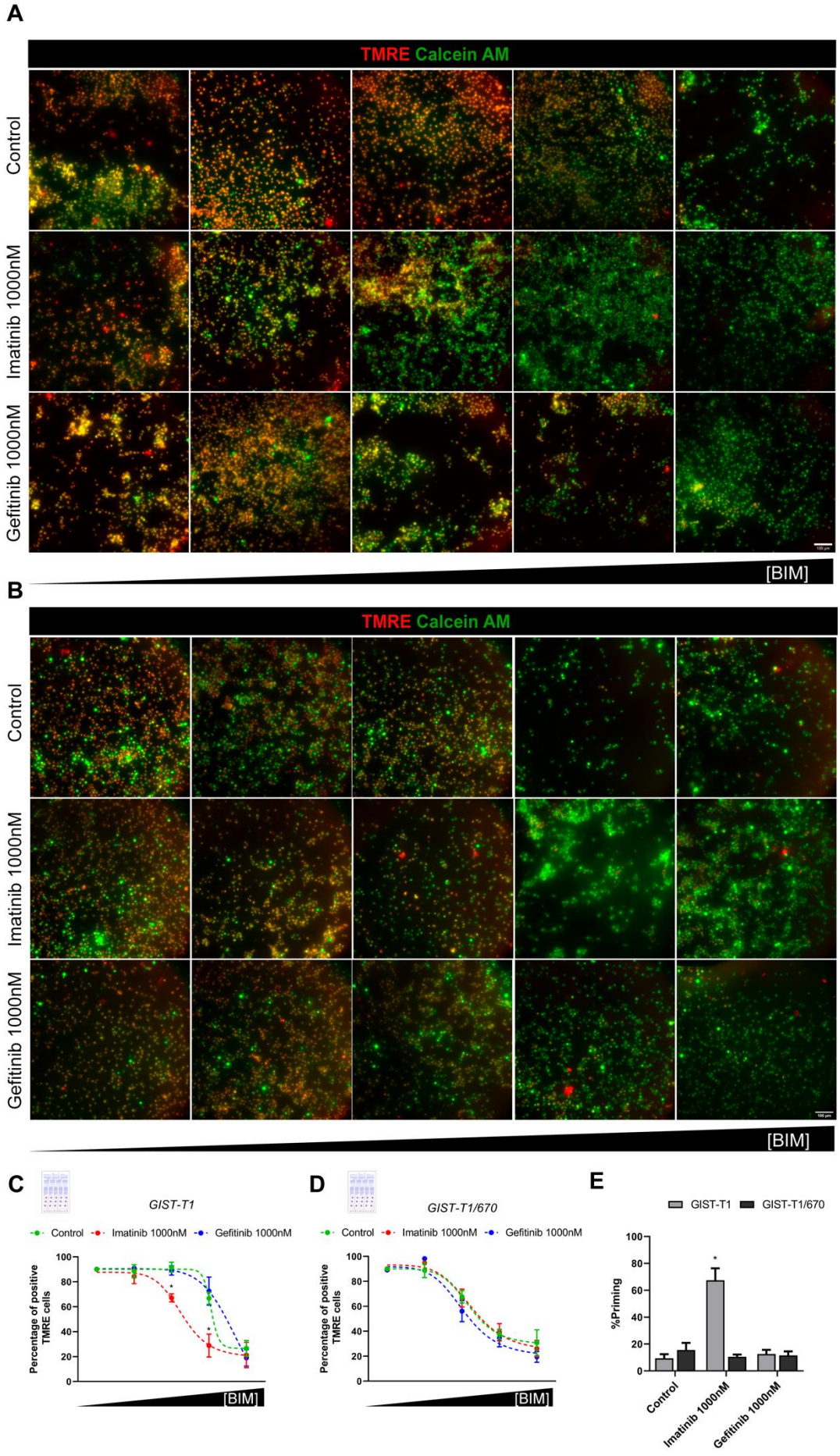
A
TMRE Calcein AM
Control
Imatinib 1000nM
Gefitinib 1000nM
[BIM]
B
TMRE Calcein AM
Control
Imatinib 1000nM
Gefitinib 1000nM
[BIM]
C
GIST-T1
Control
Imatinib 1000nM
Gefitinib 1000nM
Percentage of positive TMRE cells
[BIM]
D
GIST-T1/670
Control
Imatinib 1000nM
Gefitinib 1000nM
Percentage of positive TMRE cells
[BIM]
E
GIST-T1
GIST-T1/670
%Priming
Control
Imatinib 1000nM
Gefitinib 1000nM

**Figure 31. Microfluidic-based DBP obtains similar results as the FACS-based DBP.** Visualization of **A)** GIST-T1 and **B)** GIST-T1/670 cells seeded inside the cell chambers of the microfluidic chip after treatment with DMSO, imatinib and gefitinib for 16 hours and exposed to increasing concentrations of BIM peptide generated using microfluidics. Alive cells are stained in green and TMRE (red field) is used to identify apoptotic from non-apoptotic cells. Scale bars, 100 µm. **C)** GIST-T1 and **D)** GIST-T1/670 microfluidic-based DBP curves after incubation for 16 hours with DMSO, imatinib and gefitinib. Results are represented as the percentage of cells with positive TMRE signal after incubation with increasing concentrations of BIM peptide produced by the microfluidic gradient generator. **E)** Quantification of %priming (percentage of cells with negative TMRE signal) in GIST-T1 and GIST-T1/670 cells inside the microfluidic chip. Values were chosen in the BIM peptide condition where the control cells started to engage MOMP and lose TMRE staining. All results are expressed as the mean ± S.E.M. of at least three biologically independent replicates. * indicates a p-value < 0.05.

Using an automatic cell identification software over the image sets obtained after performing the assay inside the microfluidic chip, we identified all cells using the green field (viable cells) and quantified all fluorescence intensity values in the red field (TMRE). By applying a threshold in the untreated control condition, we differentiated between apoptotic and non-apoptotic cells and generated dose-response curves with BIM. In untreated GIST-T1 cells, increasing BIM peptide exposure caused an induction of apoptosis that generated the curve required for the assay. In the case of imatinib-treated cells we observed a shift of the curve to the left, indicating an increase in apoptotic priming. In contrast, gefitinib did not produce any apoptotic induction (Figure 31C). Similarly, with GIST-T1/670 cells we also obtained a dose-response curve, but neither imatinib nor gefitinib caused a significant shift in the curve, demonstrating that none of the treatments caused apoptotic priming (Figure 31D). With the number of TMRE-positive cells we quantified the amount of apoptotic priming for each cell line and therapy. As expected, we only found a statistically significant increase in priming in the GIST-T1 cell line treated with imatinib (Figure 31E). These results demonstrate that µDBP provides similar results as the standard FACS-based DBP in these cell lines but allowing the automatization of the process inside the microfluidic chip and reducing the number of cells needed 10-fold (from 300k to 30k per treatment).

### 5.3.2. Microfluidic-based DBP identifies effective treatments in a primary GIST patient biopsy

Our final goal is to use this platform to personalize cancer treatment. Therefore, we sought to assess its potential application in primary patient samples. In collaboration with Dr. César Serrano from the Vall d'Hebron Institute of Oncology, we analyzed a GIST patient sample, and we used it to compare the standard FACS-based DBP method with μDBP. The biopsy was obtained from a 69-year-old patient with a 7-year history of *KIT* exon 11-mutant GIST with peritoneal metastases. The patient had a good response to first-line treatment with imatinib, but subsequently suffered disease progression that was then treated with sunitinib, regorafenib and then an agent evaluated in clinical trials. The best response that was achieved with these treatments was a stabilization of the disease. At this point clinicians decided to perform debulking surgery of a 15-centimeter peritoneal mass and several adjacent nodules. The tumor showed classical fusiform features and intense CD117 (KIT) staining, the known mutation in exon 11 of *KIT* and a secondary mutation in exon 17 of the same gene (Y823D).

Clinicians suggested ripretinib (a c-KIT inhibitor effective against a large number of KIT mutations) and dactolisib (a dual PI3K/mTOR inhibitor) as potential therapeutic options for this patient. After disaggregating the tumor cells, we tested these agents, plus imatinib as a negative control, and performed FACS-based DBP. We obtained a dose-response curve with BIM, but none of the treatments caused a shift in the curve (Figure 32A), or change in apoptotic priming when we quantified it (Figure 32B). Then we analyzed more thoroughly the FACS-based DBP data focusing on sensitizer peptides to identify antiapoptotic adaptations that could be exploited with BH3 mimetics. We identified an increase in apoptotic priming with the BAD peptide, but not HRK, after dactolisib treatment (Figure 32B). These results suggest that dactolisib treatment induced a BCL-2 mediated adaptation and potential therapeutic use of venetoclax. We then repeated the FACS-based DBP analyzing dactolisib and its combination with venetoclax. Importantly, the latter caused a significant increase in apoptotic priming (Figure 32C), demonstrating that the combination of these two treatments was effective on this patient sample.

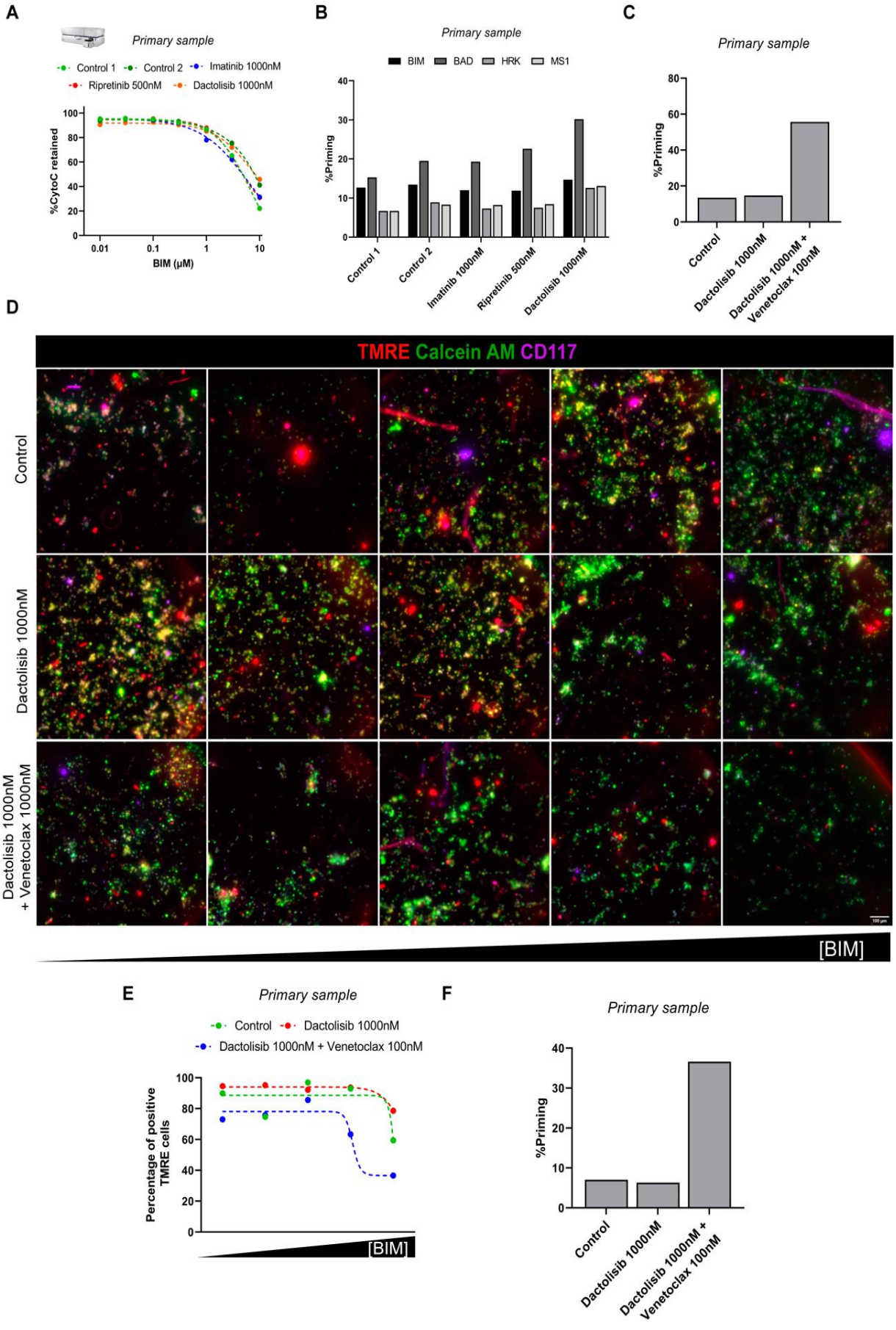
A
Primary sample
Control 1
Control 2
Imatinib 1000nM
Ripretinib 500nM
Dactolisib 1000nM
%CytoC retained
BIM (µM)
B
Primary sample
BIM
BAD
HRK
MS1
%Priming
Control 1
Control 2
Imatinib 1000nM
Ripretinib 500nM
Dactolisib 1000nM
C
Primary sample
%Priming
Control
Dactolisib 1000nM
Dactolisib 1000nM + Venetoclax 100nM
D
TMRE Calcein AM CD117
Control
Dactolisib 1000nM
Dactolisib 1000nM + Venetoclax 1000nM
[BIM]
E
Primary sample
Control
Dactolisib 1000nM
Dactolisib 1000nM + Venetoclax 100nM
Percentage of positive TMRE cells
[BIM]
F
Primary sample
%Priming
Control
Dactolisib 1000nM
Dactolisib 1000nM + Venetoclax 100nM

**Figure 32. Microfluidic-based DBP personalizes treatment directly in patient samples. A)** FACS-based DBP curves after incubation for 16 hours with DMSO, imatinib, ripretinib and dactolisib in primary cancer cells. Results are represented as the percentage of cells with cytochrome c retained inside the mitochondria after incubation with increasing concentrations of BIM peptide. **B)** Quantification of % priming (percentage of cells with cytochrome c scape) in primary cancer cells after incubation with BIM, BAD, HRK and MS1 peptides. **C)** Quantification of % priming after BIM peptide incubation in primary cancer cells incubated for 16 hours with DMSO, dactolisib and the combination of dactolisib and venetoclax. **D)** Visualization of primary cancer cells seeded inside the cell chambers of the microfluidic chip after treatment with DMSO, dactolisib and the combination of dactolisib and venetoclax for 16 hours and exposure to increasing concentrations of BIM peptide generated using microfluidics. Alive cells are marked in green, tumoral cells in violet and TMRE (red field) is used to identify apoptotic from non-apoptotic cells. Scale bars, 100 µm. **E)** Microfluidic-based DBP curves after incubation of the primary cancer cells for 16 hours with DMSO, dactolisib and the combination of dactolisib and venetoclax. Results are represented as the percentage of cells with positive TMRE signal after incubation with increasing concentrations of BIM peptide produced by the microfluidic gradient generator. **F)** Quantification of % priming (percentage of cells with negative TMRE signal) in primary cancer cells inside the microfluidic chip. Values were chosen in the BIM peptide condition where the control cells started to engage MOMP and lose TMRE staining.

We next tested whether our microfluidic platform could also detect this effective combination as a proof-of-concept. We seeded the patient-isolated tumor cells inside the microfluidic chip and treated them with dactolisib as single agent or in combination with venetoclax, in addition to the control condition. We conducted the µDBP protocol, staining with the corresponding markers and applying the different concentrations of BIM, and acquired fluorescence images of all conditions. We could observe a good viability (stained with calcein AM), good tumor cell identification (using an anti-CD117 fluorescent antibody) and TMRE staining that decreased its intensity with increasing concentrations of BIM (Figure 32D). Interestingly, the combination of dactolisib and venetoclax produced a decrease in TMRE intensity, indicating increased MOMP and apoptotic priming (Figure 32D). By identifying individual cells using the viability marker and quantifying the TMRE intensities, we could construct the dose-response curve as a function of BIM concentration. The curve of treated cells was identical to the untreated cells, but the combination of dactolisib and venetoclax induced a clear shift (Figure 32E). When we quantified this change, we observed a significant increase in priming caused by the combination, but not with dactolisib as single drug (Figure 32F), correlating with FACS-based DBP results. These findings demonstrate that the µDBP assay could identify anticancer therapies directly on patient samples. The great advantage over previous versions of this new technology is that the process can be automated and requires a much lower number of cells, which could be compatible with non-invasive primary sample collection methods and *in situ* determinations. This may help the clinical implementation of this functional assay to personalize the treatment of cancer patients.

# Chapter VI

Discussion

## 6.1. DBP is a functional assay that may help personalize BCP-ALL treatment

Pediatric patients with BCP-ALL often present a good response to chemotherapy and a low mortality[300]. However, the main problem for these patients are the secondary effects caused by the treatment, during therapy and in the long term. In contrast to adults, pediatric patients are in development, and several organs are more sensitive to apoptosis and severely affected by chemotherapy[113]. In addition, around 10% of cases are refractory or develop resistance to therapy, and they present a bad prognosis and high mortality rates. There is an unmet need to improve the treatment for these children while reducing side effects[20]. Every cancer is unique, but often patients are administered with the same chemotherapy cocktail following an established protocol[24]. Precision medicine aims to improve that and effectively identify the optimal treatment to achieve a therapeutic effect with minimal side effects[301].

Multiple ongoing precision medicine initiatives are based on molecular analyses such as immunohistochemistry, fluorescent *in situ* hybridization and next generation sequencing (NGS), among others, aiming to identify molecular alterations that can be pharmacologically exploited to eliminate tumor cells. Despite the good results achieved by some of these approaches, 80% of the clinical cases could not be treated with any targeted agent. Patients can be excluded for different reasons: their tumors do not present any alteration, lack of clinically approved inhibitors or because of a limited clinical efficacy[176,179]. To circumvent these limitations, functional assays directly expose primary cancer cells to different therapeutic options, including repurposed and experimental drugs, to evaluate cytotoxicity. This straightforward strategy allows to study dynamic adaptive processes and identify effective treatments for patients over time, in both solid and liquid tumors[196,197]. However, the main limitation for functional assays is the rapid deterioration of primary cells in *ex vivo* conditions, limiting the use of standard viability determinations. In this regard, DBP can identify apoptosis induction rapidly, in less than 24 hours, while primary cells remain viable. This technique has been extensively applied to liquid and solid tumors with good results identifying treatment efficacy on patient samples[208,210,211,216,220,222]. We used DBP on pediatric BCP-ALL models with two main objectives: 1) to identify effective chemotherapy in cell lines and 2) to find new experimental targeted therapies for R/R patients.

As expected, most chemotherapeutic agents tested in cell models caused cytotoxicity, and these were predicted by DBP. Treatments such as dexamethasone, doxorubicin, daunorubicin, methotrexate and cytarabine increased apoptotic priming and produced

cytotoxicity. Other treatments, such as vincristine, L-asparaginase and hydrocortisone, showed a weaker correlation between Δ%priming and %cell death. This discrepancy is due to the incubation time with each chemotherapeutic agent. Most of these drugs cause cell death by interfering with biological processes of the cell (e.g., DNA damage, inhibiting DNA synthesis or affecting microtubule formation). Because they affect various vital processes, each treatment presents different dynamics and causes apoptosis in cells at different time points. As some treatments interfere with DNA replication, and apoptosis starts after a mitotic catastrophe, the doubling time of each cell type may affect apoptosis engagement. Therefore, by performing the DBP assay at a given time we obtained a variable response in apoptotic priming. To get a full picture of the apoptotic response for each drug, a time course analysis had to be done to determine the response dynamics. Still, we could identify a time point where we could determine treatment effectiveness: 16 hours in NALM-6 and 40 hours in SEM. This was validated by ROC curve analyses, obtaining a good predictive capacity.

After the encouraging *in vitro* results, we analyzed several PDXs, a much closer biologically model to patients' tumors. We performed DBP on cells isolated from these animal models and obtained comparable results to cell lines. Interestingly, each sample presented a different treatment response profile, emphasizing the importance of functional assays to identify the best treatment for each patient. Overall, daunorubicin was so effective in all samples that most cells were killed within 16 hours of treatment (initial timepoint used to avoid *ex vivo* deterioration of the samples), but the rest of the drugs performed differently. For example, in the PDX X142 most treatments were not cytotoxic, except dexamethasone and hydrocortisone that promoted a significant increase in priming. Therefore, we hypothesized that this patient would have responded to a treatment scheme focused on these two drugs, while other agents would probably have caused toxic side effects with no clinical benefit. In contrast, PDX X133 did not present as much priming with any treatment, but a small change in Δ%priming with several of them (L-asparaginase, dexamethasone, doxorubicin, methotrexate, cytarabine and hydrocortisone). These results suggest that in this case, combining several chemotherapeutics would probably maximize the therapeutic effect. As next steps to validate our DBP determinations, we would like to treat these PDX models, comparing the standard-of-care therapy with treatments guided by our functional predictions. In brief, two fundamental aspects could be tested: 1) if treatments guided by DBP can achieve greater efficacy than standard-of-care therapy and 2) if the new guided regimens can eliminate ineffective treatments and therefore reduce side effects.

Despite the overall good response of pediatric BCP-ALL patients to treatment, there are some cases of patients that are refractory or relapse (R/R). Therefore, it is important to find new treatments that can be effective for R/R patients, so several targeted therapies have been explored for BCP-ALL patients presenting target alterations. This may represent new therapeutic opportunities for R/R cases that lack treatment options. In this sense, we generated a library of inhibitors that have been previously studied pre-clinically for BCP-ALL with specific alterations[302]. Typically, these inhibitors are guided by genetic determinations, which can be expensive, time-consuming and sometimes do not detect targetable alterations. Moreover, pediatric patients present a low frequency of somatic mutations compared to adults, thus reducing the number of novel targeted therapies and biomarkers that can be used to treat these patients[303]. An alternative to these molecular analyses are functional assays, like DBP, that can identify treatments that directly induce apoptosis in cancer cells regardless of their genetic background[304].

Using our BCP-ALL cell lines, we confirmed that DBP could perfectly predict targeted agents that increased cytotoxicity. Two of these agents seemed particularly promising: trametinib in both cell lines and sunitinib in the SEM line. Interestingly, DBP results correlated with the genetic information from these cell lines. NALM-6 cells only responded to trametinib inhibition of MEK, as these cells present a mutation of NRAS and downstream activation of the MAPK pathway, that explains the sensitivity to this inhibitor[305]. For the SEM cell line, we predicted sunitinib and trametinib effectiveness with DBP, that was later confirmed by cell death determinations. Sunitinib is a multi-kinase inhibitor that targets FLT3 and has been studied to treat multiple hematological diseases[306], and since this protein is highly expressed in this cell line correlated with the observed cytotoxicity[287,307]. Interestingly, when studying which pathways were affected by sunitinib in SEM cells, we observed a clear inhibition of the MAPK pathway, which explains why trametinib also eliminated these cells. Furthermore, when we tested the same treatments on a PDX model harboring the same genetic alteration as the SEM cell line, we detected a similar profile. In fact, we found that the only treatment that caused a change in apoptotic priming was sunitinib, demonstrating that DBP can also predict treatment efficacy in models closer to patients such as PDXs.

These results demonstrate that DBP could impact and help improve pediatric BCP-ALL patients treatment. One of the advantages of DBP in liquid tumors is that it is relative easy to use with patient-isolated cells (directly from blood or from bone marrow aspirates). Thus, this assay can be repeated multiple times to adapt the therapy

according to the evolution of the tumor. With this idea in mind, we can apply functional assays with different objectives, such as stratifying patients, to use milder regimens to reduce side effects, discard some of the drugs that would not be effective in a particular regimen, or especially discover new treatments for R/R patients.

## 6.2. The use of BH3 mimetics can be guided by DBP to identify and overcome antiapoptotic adaptations

The emergence of BH3 mimetics, specific inhibitors of antiapoptotic proteins, has undoubtfully improved cancer treatment since the first approval of venetoclax to treat chronic lymphocytic leukemia patients[308]. As single agents, these molecules have demonstrated efficacy in several types of cancer, mainly hematological, but many studies suggest that they have a great potential to enhance other anticancer treatments, both conventional chemotherapies and targeted agents[156,159,309–313]. Cancer cells often use antiapoptotic proteins to survive treatment and acquire resistance, which can be overcome by BH3 mimetics[142,314–316]. In treatments already approved for BCP-ALL, to combine BH3 mimetics with other drugs would demand a biomarker to guide their use in patients. Importantly, functional predictions made by DBP using sensitizer specific BH3 peptides can identify antiapoptotic adaptations[219,221,226,317], in a faster and cheaper way compared to more sophisticated molecular analyses. While DBP with the BIM peptide can detect effective chemotherapy or targeted agents for patients, using these sensitizer peptides we can track antiapoptotic adaptations that promote resistance to these compounds. Thus, adding a BH3 mimetic to the initial treatment scheme can boost the cytotoxic effect, maximizing the chances to fully eliminate cancer cells.

Using this strategy, we could observe that various chemotherapeutic treatments caused antiapoptotic adaptations. Once these adaptations were identified, we employed specific BH3 mimetics such as ABT-199/venetoclax (BCL-2 inhibitor), A133 (BCL-xL inhibitor) and S63845 (MCL-1 inhibitor) to determine if the combination was synergistic. In fact, this approach has been studied to potentially reduce chemotherapy dosing or improve the effectiveness of certain anticancer agents[159,313]. Adding the right BH3 mimetic a few hours after the initial treatment, when the antiapoptotic adaptation is detected, could enhance treatment effectiveness. We hypothesize that these metronomic combinations instead of directly administering both agents at the same time, could prevent undesired toxicities and side effects in patients, while sustaining or increasing their anticancer activity[318].

When we studied NALM-6 cells we observed different antiapoptotic responses. Dexamethasone and doxorubicin were highly effective as single agents and promoted an increase in apoptotic priming with all three sensitizer peptides, suggesting a combined BCL-2, BCL-xL and MCL-1 mediated resistance to treatment. We next sought to explore a dose reduction of these cytotoxic agents aiming to prevent potential secondary effects in the clinic, and we observed that by reducing 10-fold their concentration these treatments became ineffective in NALM-6 cells. However, the sequential addition of a BH3 mimetic in combination with low-dose chemotherapy produced a synergistic effect recovering the high-dose efficacy of both dexamethasone and doxorubicin. All three antiapoptotic inhibitors caused a synergistic effect, demonstrating that all three antiapoptotic proteins were important pro-survival elements for these cells, but combinations with S63845 were more effective than with the other two BH3 mimetics. In contrast, L-asparaginase and hydrocortisone treatment produced low cytotoxicity in NALM-6 cells. L-asparaginase promoted a clear increase in priming with the BAD peptide. Not suprisingly, L-asparaginase synergized with BCL-2 and BCL-xL inhibitors enhancing cell death. DBP predictions with the BAD peptide correlated with the observed combinations, but we were unable to identify a signal with HRK that would indicate BCL-xL adaptation, which could point to an unidentified contribution of BCL-w. This discrepancy might be caused by a cross compensation between antiapoptotic proteins and different temporal dynamics of the adaptations. Similarly, treatment for 16 hours with hydrocortisone alone produced a non-significant small increase with all three sensitizer peptides. However, when we combined this treatment with BH3 mimetics we could observe a clear synergistic effect with all three inhibitors, again demonstrating a combined antiapoptotic adaptation. In summary, our observations suggest that antiapoptotic adaptations are dynamic and it would be critical to identify the best timing to use BH3 mimetics in combination.

In the SEM cell line, ABT-199 and S63845 were highly cytotoxic as single agents, so we reduced 10-fold their concentration to explore potential synergies. We hypothesized that SEM cells, unlike NALM-6, strongly depended on one antiapoptotic protein and, when blocked, it could not be rescued by a second one. Similarly as in NALM-6 cells, dexamethasone caused an increase in priming with all the three sensitizer peptides; antiapoptotic adaptations that were later confirmed with cell death determinations. In particular, BCL-2 and MCL-1 inhibitors used in combination with a low dose of dexamethasone were strongly synergistic. Interestingly, treatment with L-asparaginase caused a different antiapoptotic response compared to the other cell line. In this case, we detected an increase in priming with all three sensitizer peptides and, as expected,

a clear synergy when combining this treatment with all BH3 mimetics tested (unlike NALM-6 cells line that did not show a MCL-1 adaptation). Although both cell lines are BCP-ALL, they present different genetic backgrounds and were obtained from patients of different ages and gender, which may explain the distinct responses to treatments. Finally, hydrocortisone also caused an increase in priming with the three sensitizer peptides. By combining this treatment with the different BH3 mimetics, we were able to move from the moderate cytotoxicity caused by hydrocortisone as single agent to a clear synergy, especially in combination with ABT-199 and S63845. Although in the SEM cell line we could see similar adaptations, there were important differences between the two that were identified with DBP, demonstrating the heterogeneity of the antiapoptotic adaptations. These observations again highlight the importance of functional determinations to guide therapy.

Targeted therapies also caused antiapoptotic adaptations that could be identified by DBP. Importantly, the most effective inhibitor for each cell line also produced the most remarkable antiapoptotic adaptations. For instance, in NALM-6 the treatment with trametinib induced a multiple increase in antiapoptotic priming which correlated with a synergy with all three BH3 mimetics. Particularly, the combination of trametinib with S63845 was especially effective, boosting cell death from 20% to almost a complete elimination of cancer cells. In the SEM cell line, sunitinib was highly cytotoxic as a single agent. However, we also detected a BCL-2, BCL-xL and MCL-1-mediated adaptation upon treatment. Aiming for efficient synergistic combination with lower dosing, we next combined a 10-fold lower concentration of sunitinib with BH3 mimetics, and obtained the same cytotoxicity as in high-dose when adding ABT-199 and S63845. These results demonstrate that antiapoptotic protein-mediated adaptations are widespread for both chemotherapy and targeted therapies. The inclusion of BH3 mimetics could enhance the treatment of many cancers, allowing to reduce therapeutic dosing and potential side effects, and boosting otherwise ineffective treatments.

To test if the antiapoptotic adaptations observed *in vitro* were also present in BCP-ALL patients, we next studied several PDX models. When using the same chemotherapeutics, we could observe that again each sample exerted different antiapoptotic adaptations, showing a completely variable DBP profile with the sensitizer peptides. Interestingly, one of the samples presented the same genetic background as the SEM cell line (*KMT2A* rearrangement), and it revealed the same antiapoptotic adaptations in response to sunitinib, indicating that the suggested combinations with SEM cells could also be effective in patients. The addition of any BH3 mimetic to

chemotherapy or targeted agent-based regimens for patients with BCP-ALL will require clinical validation to demonstrate that it improves current approved treatments. However, the response heterogeneity may difficult the implementation of these new therapeutic strategies. That is why novel biomarkers to guide their use are needed to identify the best combination for each patient. In this regard, our results demonstrate that DBP identifies antiapoptotic adaptations and could be used as a biomarker for BH3 mimetics in clinical trials.

These results will require further *in vivo* validation to demonstrate that the proposed combinations could truly improve the treatment of patients with BCP-ALL and reduce secondary effects. PDXs could be used to perform a comparative study of the standard-of-care treatments with a combination that includes a BH3 mimetic guided by DBP, as a preclinical study and validation for this functional assay.

## 6.3. Molecular analyses of the antiapoptotic adaptations

As we discussed, DBP could identify which treatment would be most effective to induce apoptosis regardless of how this occurs. Thus, we next sought to study which molecular mechanisms would explain the observed response to targeted inhibitors. The BCL-2 family of proteins is a complex interactome strongly regulated at several molecular levels. For instance, changes in protein expression do not always explain the pro-survival adaptations observed, so it is necessary to further study BCL-2 family protein interactions, such as the binding between antiapoptotic proteins and the other members: sensitizers, effectors, and activators.

When we studied NALM-6 response to trametinib, we observed an increase in the antiapoptotic protein MCL-1 and the proapoptotic protein BIM expression. The latter had been previously reported by protein stabilization due to ERK1/2 dephosphorylation[151,319–321]. These results suggested that the proapoptotic effect caused by the increase in BIM is at least partially neutralized by MCL-1, and explains the synergy between trametinib and S63845, as already seen in other tumors[322]. We then immunoprecipitated MCL-1 and studied its interaction with BIM, and we detected that trametinib caused an increase in MCL-1 and BIM binding, that was disrupted by the addition of S63845 (Figure 33).

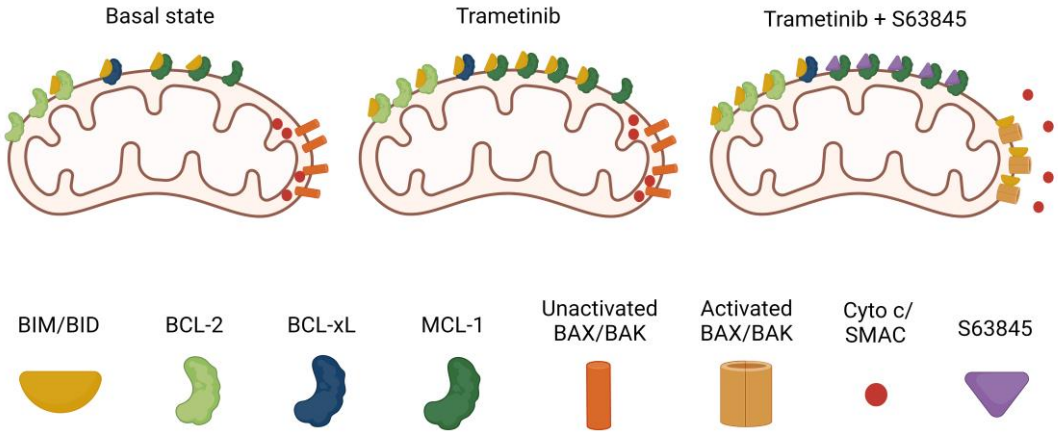


**Figure 33.** Representation of the mechanism of the synergy in the combination between trametinib and S63845 in NALM-6 cells. Created with BioRender.com.

In the SEM cell line, we could also observe an increase in BIM expression upon sunitinib treatment, also caused by loss of ERK1/2 phosphorylation, although other reports suggest that it may also be caused by the inhibition of STAT3 and AKT[323,324]. This proapoptotic protein increase suggested that sunitinib activated the apoptotic process but could not achieve a complete elimination of tumor cells, pointing to an antiapoptotic adaptation. Counterintuitively, when we analyzed MCL-1 expression, we observed that it is decreased upon treatment, similarly as for BCL-2. These results contrast with the synergistic combinations observed with sunitinib and MCL-1/BCL-2 inhibitors. We then studied the interaction between MCL-1 and BCL-2 with BIM, we detected an increment in their binding despite that the antiapoptotic protein expression was lower. This dual increase in binding clarifies the observed synergy between sunitinib and ABT-199/S63845 (Figure 34). Importantly, when we analyzed the BCL-2 family expression in a PDX sample carrying the *KMT2A* rearrangement, we could similarly identify an increase in BIM and a decrease in MCL-1 expression upon sunitinib treatment, correlating with the SEM cells.

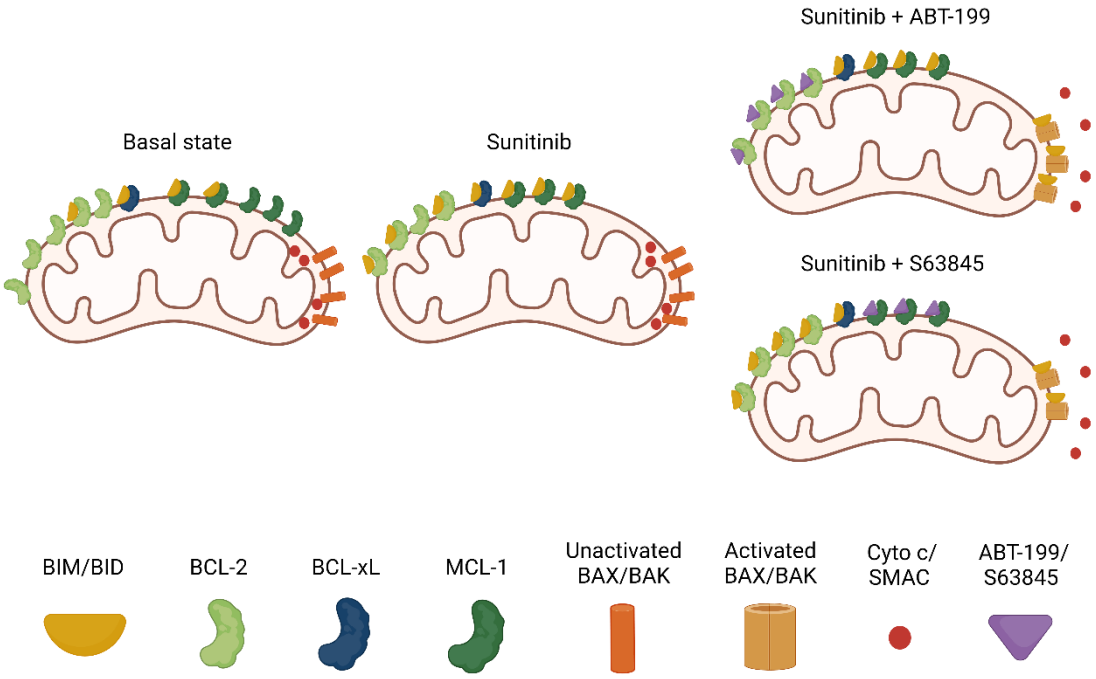


**Figure 34.** Representation of the mechanism of the synergy in the combination between sunitinib and ABT-199/S63845 in SEM cells. Created with BioRender.com.

Our results demonstrate that antiapoptotic adaptations are heterogeneous. For instance, in BCP-ALL we detected that MCL-1 expression could increase to inhibit BIM-mediated activation of apoptosis or decrease but exerting a higher binding affinity to this activator. Other researchers have determined that cancer treatments can affect sensitizer proteins such as NOXA or BAD[152,219], increase the interaction of antiapoptotic proteins with other activators such as tBID or effectors such as BAK[221] or upregulate of other antiapoptotic proteins such as BCL-2[325], among others. Therefore, characterizing each patient cancer cells' resistance may point to an effective use of BH3 mimetics. Interestingly, DBP can anticipate these antiapoptotic adaptations upon treatment, regardless of the underlying molecular mechanism, to identify effective combinations with BH3 mimetics.

## 6.4. DBP may identify effective treatments for different types of pediatric leukemia

Functional assays could help personalize medicine at hospitals, but first we would need to clinically validate them to demonstrate their efficacy. Overall, this is the main difficulty for functional assays implementation in the clinic. Recently, especially after the

success of pharmacoscopy in EXALT I[201], some functional platforms are being tested in the clinic, like FORESEE or EXALT II clinical trials (currently recruiting), paving the way for other technologies such as DBP. For instance, the clinical study by Garcia and colleagues used DBP to predict the efficacy of lenalidomide in R/R AML patients, correlating the increase in apoptotic priming with this treatment efficacy in patients[222]. In our laboratory we also analyzed several R/R pediatric patient samples presenting various hematologic diseases (AML, T-ALL and undifferentiated leukemia) and used DBP to test different treatments suggested by clinicians for potential compassionate drug use. In several cases, the drug identified by DBP was included in the patient's treatment schedule and we tracked the clinical response. In two patients we identified that venetoclax increased apoptotic priming, and when they were treated with this approved BH3 mimetic they achieved a complete remission. These results highlight the great potential of DBP to predict the efficacy of BH3 mimetics in patients, otherwise difficult to identify by standard molecular techniques such as mRNA or protein expression determinations[326].

Although our cohort is small at the moment, based on our preliminary results, we believe that DBP could improve the treatment of pediatric patients with hematologic diseases that do not respond to the standard-of-care treatments. We aim to get involved in a clinical trial to fully demonstrate the therapeutic advantage of performing a DBP to guide treatment, especially in pediatric hematologic R/R cases.

## 6.5. Microfluidic-based DBP can be used to find effective treatments directly on patient cancer cells

DBP analyses on primary samples obtained from hematological diseases is feasible because of the accessibility to cancer cells, that are easy to isolate. In contrast, solid tumor biopsies are difficult to process and not always provide enough cells to perform the assay. To solve this problem, several approaches have been developed to increase the availability of cells for functional assays, including the generation of cell lines, 3D culture methods, and generation of organoids or PDXs, among others, as summarized in the introduction. A disadvantage in these techniques is the time and infrastructure required to obtain the necessary number of cells, and the preservation of tumors' native characteristics. Even more importantly, the major limiting factor for most approaches is the viability of these cells in *ex vivo* conditions. In this regard, DBP is a rapid assay that avoids the deterioration of primary samples, but still has the drawback of requiring a high number of viable cells. Some alternatives have been developed to overcome this limitation, for example HT-DBP that uses 384 well plates, multi-well dispensers and

automated high-content fluorescence microscopy to reduce the required cells to 5,000 per treatment. This new technique has been validated in primary colon and non-small lung cancer cells with excellent results[230,231]. However, HT-DBP requires prior optimization to determine the optimal concentration of BIM peptide, the use of specialized equipment and trained personnel. Thus it must be centralized in a specialized laboratory complicating its widespread application at hospitals.

We explored a different alternative by developing a microfluidic chip to reduce the number of cells and automatize the assay. To validate this new platform, we directly compared it with the standard FACS-based DBP in GIST, both *in vitro* and directly on primary patient samples, but reducing 10-fold the number of cells required. Our experimental results demonstrated that the μDBP platform could identify increased apoptotic priming in GIST-T1 cells after treatment with imatinib, but not gefitinib that we used as a negative control or in the resistant GIST-T1/670 cell line. Once tested *in vitro*, we next performed μDBP and FACS-based DBP on a GIST patient biopsy as a proof of concept; and in both platforms we detected that the combination of dactolisib and venetoclax was effective and increased priming, validating the microfluidic prototype's predictive capacity. This new platform may represent a great advantage to make personalized medicine more accessible by directly testing therapies on cancer patient-isolated cells, as we could drastically reduce the number of cells needed (from 300,000 per treatment in the FACS-based DBP to 30,000 in the μDBP). This reduction would allow the use of non-surgically obtained biopsies, for example core-needle biopsies or fine-needle aspirates and will enable the continuous functional monitoring of the tumor, anticipate adaptations and adjust treatment over time. Although the prototype has been developed using PDMS, an accessible material that allows fast fabrication, once the final prototype is obtained, could be massively produced using materials such as PMMA, which would help its *in situ* implementation at hospitals[327–329]. Moreover, the substitution of the cytochrome c antibody for TMRE to identify apoptotic engagement, diminishes the time needed to perform the protocol to just a few hours, Importantly, thanks to the automatic gradient generator, the DBP experimental procedure can be greatly simplified, reducing the possibility of human errors and the need for qualified personnel.

This is just a first prototype, and several improvements should be made on μDBP. For instance, we are currently working on a new logarithmic gradient generator, which would allow a wider range of BIM concentrations to correctly identify changes in apoptotic priming. Moreover, with the current design we are limited to test only two

treatments (and a control) for each microfluidic chip, so we are now exploring two new versions of the microfluidic platform aiming for a potential commercialization: one with more rows to quickly test 8-10 treatments and a larger one for screening purposes. In both cases, it would only be necessary to have an unsophisticated microfluidic pump and a fluorescent read-out for a ready-to-use medical device to perform *in situ* analyses at hospitals.

# Chapter VII

## Conclusions

1. DBP predicts the efficacy of chemotherapy and targeted agents in BCP-ALL models, which correlates with cell death determinations.
2. DBP identifies antiapoptotic adaptations that confer resistance after treatment. DBP guided use of BH3 mimetics, specific inhibitors of antiapoptotic proteins, improves the therapeutic efficacy in various models.
3. Antiapoptotic adaptations are heterogeneous and vary depending on the treatment and the cell model analyzed. The increased interaction between activator and antiapoptotic proteins protects cells against cancer treatment, by different mechanisms, an interaction that is overcome employing BH3 mimetics.
4. DBP predicted several effective treatments in primary samples of pediatric leukemia patients lacking therapeutic options, achieving a complete remission in some cases where venetoclax was administered.
5. The new microfluidic version of DBP identifies effective treatments in *in vitro* models and a GIST patient sample, automatizing the process and reducing the number of cells needed to perform the assay.

# References

1. Hanahan, D. & Weinberg, R. A. The hallmarks of cancer. *Cell* **100**, 57–70 (2000).

2. Ferlay, J. *et al.* Global cancer observatory: cancer today. *International Agency for Research on Cancer* Available from https://gco.iarc.fr/today (2020). Available at: https://gco.iarc.fr/today. (Accessed: 5th February 2022)

3. Siegel, R. L., Miller, K. D. & Jemal, A. Cancer statistics, 2020. *CA. Cancer J. Clin.* **70**, 7–30 (2020).

4. Bhakta, N. *et al.* Childhood cancer burden: a review of global estimates. *Lancet Oncol.* **20**, e42–e53 (2019).

5. Dickerman, J. D. The late effects of childhood cancer therapy. *Pediatrics* **119**, 554–568 (2007).

6. Ross, J. A., Spector, L. G., Robison, L. L. & Olshan, A. F. Epidemiology of leukemia in children with down syndrome. *Pediatr. Blood Cancer* **44**, 8–12 (2005).

7. Greaves, M. Infection, immune responses and the aetiology of childhood leukaemia. *Nat. Rev. Cancer* **6**, 193–203 (2006).

8. Clarke, R. T. *et al.* Clinical presentation of childhood leukaemia: A systematic review and meta-analysis. *Arch. Dis. Child.* **101**, 894–901 (2016).

9. Van Dongen, J. J. M. *et al.* Prognostic value of minimal residual disease in acute lymphoblastic leukaemia in childhood. *Lancet* **352**, 1731–1738 (1998).

10. Starza, I. Della *et al.* Minimal residual disease in acute lymphoblastic leukemia: Technical and clinical advances. *Front. Oncol.* **9**, (2019).

11. Schultz, K. R. *et al.* Long-term follow-up of imatinib in pediatric Philadelphia chromosome-positive acute lymphoblastic leukemia: Children's oncology group study AALL0031. *Leukemia* **28**, 1467–1471 (2014).

12. Appelbaum, F. R. & Bernstein, I. D. Gemtuzumab ozogamicin for acute myeloid leukemia. *Blood* **130**, 2373–2376 (2017).

13. Pollyea, D. A., Amaya, M., Strati, P. & Konopleva, M. Y. Venetoclax for AML: Changing the treatment paradigm. *Blood Adv.* **3**, 4326–4335 (2019).

14. Foster, J. B. & Maude, S. L. New developments in immunotherapy for pediatric leukemia. *Curr. Opin. Pediatr.* **30**, 25–29 (2018).

15. Bhojwani, D., Yang, J. J. & Pui, C. H. Biology of childhood acute lymphoblastic leukemia. *Pediatr. Clin. North Am.* **62**, 47–60 (2015).

16. Arber, D. A. *et al.* The 2016 revision to the World Health Organization classification of myeloid neoplasms and acute leukemia. *Blood* **127**, 2391–2405 (2016).

17. Roberts, K. G. & Mullighan, C. G. The biology of B-progenitor acute lymphoblastic leukemia. *Cold Spring Harb. Perspect. Med.* **10**, 1–22 (2020).

18. Pui, C. H., Nichols, K. E. & Yang, J. J. Somatic and germline genomics in paediatric acute lymphoblastic leukaemia. *Nat. Rev. Clin. Oncol.* **16**, 227–240 (2019).

19. Ma, X. *et al.* Rise and fall of subclones from diagnosis to relapse in pediatric B-acute lymphoblastic leukaemia. *Nat. Commun.* **6**, 6604 (2015).

20. Pui, C. H. Precision medicine in acute lymphoblastic leukemia. *Front. Med.* **14**, 689–700 (2020).

21. Vrooman, L. M. & Silverman, L. B. Childhood acute lymphoblastic leukemia: Update on prognostic factors. *Curr. Opin. Pediatr.* **21**, 1–8 (2009).

22. Borowitz, M. J. *et al.* Clinical significance of minimal residual disease in childhood acute lymphoblastic leukemia and its

relationship to other prognostic factors: A Children's Oncology Group study. *Blood* **111**, 5477–5485 (2008).

23. Prucker, C. *et al.* Induction death and treatment-related mortality in first remission of children with acute lymphoblastic leukemia: A population-based analysis of the Austrian Berlin-Frankfurt-Münster study group. *Leukemia* **23**, 1264–1269 (2009).

24. Möricke, A. *et al.* Long-term results of five consecutive trials in childhood acute lymphoblastic leukemia performed by the ALL-BFM study group from 1981 to 2000. *Leukemia* **24**, 265–284 (2010).

25. Pullen, J. *et al.* Extended triple intrathecal chemotherapy trial for prevention of CNS relapse in good-risk and poor-risk patients with B-progenitor acute lymphoblastic leukemia: A Pediatric Oncology Group Study. *J. Clin. Oncol.* **11**, 839–849 (1993).

26. Algeri, M., Merli, P., Locatelli, F. & Pagliara, D. The role of allogeneic hematopoietic stem cell transplantation in pediatric leukemia. *J. Clin. Med.* **10**, 3790 (2021).

27. Slayton, W. B. *et al.* Dasatinib plus intensive chemotherapy in children, adolescents, and young adults with philadelphia chromosome–positive acute lymphoblastic leukemia: Results of children's oncology group trial AALL0622. *J. Clin. Oncol.* **36**, 2306–2313 (2018).

28. Von Stackelberg, A. *et al.* Phase I/Phase II study of blinatumomab in pediatric patients with relapsed/refractory acute lymphoblastic leukemia. *J. Clin. Oncol.* **34**, 4381–4389 (2016).

29. Bhojwani, D. *et al.* Inotuzumab ozogamicin in pediatric patients with relapsed/refractory acute lymphoblastic leukemia. *Leukemia* **33**, 884–892 (2019).

30. Maude, S. L. *et al.* Tisagenlecleucel in Children and Young Adults with B-Cell Lymphoblastic Leukemia. *N. Engl. J. Med.* **378**, 439–448 (2018).

31. Fry, T. J. *et al.* CD22-targeted CAR T cells induce remission in B-ALL that is naive or resistant to CD19-targeted CAR immunotherapy. *Nat. Med.* **24**, 20–28 (2018).

32. Qin, H. *et al.* Preclinical Development of Bivalent Chimeric Antigen Receptors Targeting Both CD19 and CD22. *Mol. Ther. - Oncolytics* **11**, 127–137 (2018).

33. Maude, S. L. *et al.* Targeting JAK1/2 and mTOR in murine xenograft models of Ph-like acute lymphoblastic leukemia. *Blood* **120**, 3510–3518 (2012).

34. Khaw, S. L. *et al.* Venetoclax responses of pediatric ALL xenografts reveal sensitivity of MLL-rearranged leukemia. *Blood* **128**, 1382–1395 (2016).

35. Leonard, J. T. *et al.* Targeting BCL-2 and ABL/LYN in Philadelphia chromosome-positive acute lymphoblastic leukemia. *Sci. Transl. Med.* **8**, 9540–9548 (2016).

36. Fischer, U. *et al.* Genomics and drug profiling of fatal TCF3-HLFâ 'positive acute lymphoblastic leukemia identifies recurrent mutation patterns and therapeutic options. *Nat. Genet.* **47**, 1020–1029 (2015).

37. Tallen, G. *et al.* Long-term outcome in children with relapsed acute lymphoblastic leukemia after time-point and site-of-relapse stratification and intensified short-course multidrug chemotherapy: Results of trial ALL-REZ BFM 90. *J. Clin. Oncol.* **28**, 2339–2347 (2010).

38. Meier, P., Finch, A. & Evan, G. Apoptosis in development. *Nature* **407**, 796–801 (2000).

39. Norbury, C. J. & Hickson, I. D. Cellular responses to DNA damage. *Annu. Rev. Pharmacol. Toxicol.* **41**, 367–401 (2001).

40. Kerr, J. F. R., Wyllie, A. H. & Currie, A. R. Apoptosis: A basic biological phenomenon with wide-ranging implications in tissue kinetics. *Br. J. Cancer* **26**, 239–257 (1972).

41. Kerr, J. F. A histochemical study of hypertrophy and ischaemic injury of rat liver with special reference to changes in lysosomes. *J. Pathol. Bacteriol.* **90**, 419–435 (1965).

42. Kerr, J. F. Lysosome changes in acute liver injury due to heliotrine. *J. Pathol. Bacteriol.* **93**, 167–174 (1967).

43. Kerr, J. F. R. An electron-microscope study of liver cell necrosis due to heliotrine. *J. Pathol.* **97**, 557–562 (1969).

44. Kerr, J. F. R. Shrinkage necrosis: A distinct mode of cellular death. *J. Pathol.* **105**, 13–20 (1971).

45. Elmore, S. Apoptosis: A Review of Programmed Cell Death. *Toxicol. Pathol.* **35**, 495–516 (2007).

46. Savill, J. & Fadok, V. Corpse clearance defines the meaning of cell death. *Nature* **407**, 784–788 (2000).

47. Szondy, Z., Sarang, Z., Kiss, B., Garabuczi, É. & Köröskényi, K. Anti-inflammatory mechanisms triggered by apoptotic cells during their clearance. *Front. Immunol.* **8**, (2017).

48. Majno, G. & Joris, I. Apoptosis, oncosis, and necrosis: An overview of cell death. *Am. J. Pathol.* **146**, 3–15 (1995).

49. Zeiss, C. J. The apoptosis-necrosis continuum: Insights from genetically altered mice. *Vet. Pathol.* **40**, 481–495 (2003).

50. Yamazaki, T. *et al.* Mitochondrial DNA drives abscopal responses to radiation that are inhibited by autophagy. *Nat. Immunol.* **21**, 1160–1171 (2020).

51. Ellis, H. M. & Horvitz, H. R. Genetic control of programmed cell death in the nematode C. elegans. *Cell* **44**, 817–829 (1986).

52. D'Arcy, M. S. Cell death: a review of the major forms of apoptosis, necrosis and autophagy. *Cell Biol. Int.* **43**, 582–592 (2019).

53. Thornberry, N. A. *et al.* A combinatorial approach defines specificities of members of the caspase family and granzyme B: Functional relationships established for key mediators of apoptosis. *J. Biol. Chem.* **272**, 17907–17911 (1997).

54. Salvesen, G. S. & Riedl, S. J. Caspase mechanisms. in *Advances in Experimental Medicine and Biology* **615**, 13–23 (2008).

55. Earnshaw, W. C., Martins, L. M. & Kaufmann, S. H. Mammalian caspases: Structure, activation, substrates, and functions during apoptosis. *Annu. Rev. Biochem.* **68**, 383–424 (1999).

56. Hengartner, M. O. The biochemistry of apoptosis. *Nature* **407**, 770–776 (2000).

57. Locksley, R. M., Killeen, N. & Lenardo, M. J. The TNF and TNF receptor superfamilies: Integrating mammalian biology. *Cell* **104**, 487–501 (2001).

58. Ashkenazi, A. & Dixit, V. M. Death receptors: Signaling and modulation. *Science (80-. ).* **281**, 1305–1308 (1998).

59. Eck, M. J. & Sprang, S. R. The structure of tumor necrosis factor-α at 2.6 Å resolution. Implications for receptor binding. *J. Biol. Chem.* **264**, 17595–17605 (1989).

60. Kischkel, F. C. *et al.* Cytotoxicity-dependent APO-1 (Fas/CD95)-associated proteins form a death-inducing signaling complex (DISC) with the receptor. *EMBO J.* **14**, 5579–5588 (1995).

61. Tartaglia, L. A., Rothe, M., Hu, Y. F. & Goeddel, D. V. Tumor necrosis factor's cytotoxic activity is signaled by the p55 TNF receptor. *Cell* **73**, 213–216 (1993).

62. Dhein, J., Walczak, H., Bäumlert, C., Debatint, K. M. & Krammer, P. H. Autocrine T-cell suicide mediated by APO-1/(Fas/CD95). *Nature* **373**, 438–441 (1995).

63. Yonehara, S., Ishii, A. & Yonehara, M.

A cell-killing monoclonal antibody (anti-Fas) to a cell surface antigen co-downregulated with the receptor of tumor necrosis factor. *J. Exp. Med.* **169**, 1747–1756 (1989).

64. Kitson, J. *et al.* A death-domain-containing receptor that mediates apoptosis. *Nature* **384**, 372–375 (1996).

65. Migone, T. S. *et al.* TL1A is a TNF-like ligand for DR3 and TR6/DcR3 and functions as a T cell costimulator. *Immunity* **16**, 479–492 (2002).

66. Pan, G. *et al.* The receptor for the cytotoxic ligand TRAIL. *Science (80-. ).* **276**, 111–113 (1997).

67. MacFarlane, M. *et al.* Identification and molecular cloning of two novel receptors for the cytotoxic ligand TRAIL. *J. Biol. Chem.* **272**, 25417–25420 (1997).

68. Wajant, H. The Fas signaling pathway: More than a paradigm. *Science (80-. ).* **296**, 1635–1636 (2002).

69. Kim, S. G. *et al.* Transforming Growth Factor-β1 Induces Apoptosis through Fas Ligand-independent Activation of the Fas Death Pathway in Human Gastric SNU-620 Carcinoma Cells. *Mol. Biol. Cell* **15**, 420–434 (2004).

70. Hsu, H., Xiong, J. & Goeddel, D. V. The TNF receptor 1-associated protein TRADD signals cell death and NF-κB activation. *Cell* **81**, 495–504 (1995).

71. Micheau, O. & Tschopp, J. Induction of TNF receptor I-mediated apoptosis via two sequential signaling complexes. *Cell* **114**, 181–190 (2003).

72. Schug, Z. T., Gonzalvez, F., Houtkooper, R. H., Vaz, F. M. & Gottlieb, E. BID is cleaved by caspase-8 within a native complex on the mitochondrial membrane. *Cell Death Differ.* **18**, 538–548 (2011).

73. Scaffidi, C., Schmitz, I., Krammer, P. H. & Peter, M. E. The role of c-FLIP in modulation of CD95-induced apoptosis. *J. Biol. Chem.* **274**, 1541–1548 (1999).

74. Hitoshi, Y. *et al.* Toso, a cell surface, specific regulator of Fas-induced apoptosis in T cells. *Immunity* **8**, 461–471 (1998).

75. Voskoboinik, I., Whisstock, J. C. & Trapani, J. A. Perforin and granzymes: Function, dysfunction and human pathology. *Nat. Rev. Immunol.* **15**, 388–400 (2015).

76. De Saint Basile, G., Ménasché, G. & Fischer, A. Molecular mechanisms of biogenesis and exocytosis of cytotoxic granules. *Nat. Rev. Immunol.* **10**, 568–579 (2010).

77. Leung, C. *et al.* Stepwise visualization of membrane pore formation by suilysin, a bacterial cholesterol-dependent cytolysin. *Elife* **3**, e04247 (2014).

78. Metkar, S. S. *et al.* Granzyme B activates procaspase-3 which signals a mitochondrial amplification loop for maximal apoptosis. *J. Cell Biol.* **160**, 875–885 (2003).

79. Alimonti, J. B., Shi, L., Baijal, P. K. & Greenberg, A. H. Granzyme B Induces BID-mediated Cytochrome c Release and Mitochondrial Permeability Transition. *J. Biol. Chem.* **276**, 6974–6982 (2001).

80. Martinvalet, D., Dykxhoorn, D. M., Ferrini, R. & Lieberman, J. Granzyme A Cleaves a Mitochondrial Complex I Protein to Initiate Caspase-Independent Cell Death. *Cell* **133**, 681–692 (2008).

81. Lieberman, J. Granzyme A activates another way to die. *Immunol. Rev.* **235**, 93–104 (2010).

82. Kupfer, A., Singer, S. J. & Dennert, G. On the mechanism of unidirectional killing in mixtures of two cytotoxic T lymphocytes: Unidirectional polarization of cytoplasmic organelles and the membrane-associated cytoskeleton in the effector cell. *J. Exp. Med.* **163**, 489–498 (1986).

83. Wei, M. C. *et al.* Proapoptotic BAX and BAK: A requisite gateway to

mitochondrial dysfunction and death. *Science (80-. ).* **292**, 727–730 (2001).

84. Galluzzi, L. *et al.* Molecular mechanisms of cell death: Recommendations of the Nomenclature Committee on Cell Death 2018. *Cell Death Differ.* **25**, 486–541 (2018).

85. Tait, S. W. G. & Green, D. R. Mitochondria and cell death: Outer membrane permeabilization and beyond. *Nat. Rev. Mol. Cell Biol.* **11**, 621–632 (2010).

86. Saelens, X. *et al.* Toxic proteins released from mitochondria in cell death. *Oncogene* **23**, 2861–2874 (2004).

87. Chinnaiyan, A. M. The apoptosome: heart and soul of the cell death machine. *Neoplasia* **1**, 5–15 (1999).

88. Li, Y. *et al.* Mechanistic insights into caspase-9 activation by the structure of the apoptosome holoenzyme. *Proc. Natl. Acad. Sci. U. S. A.* **114**, 1542–1547 (2017).

89. Malladi, S., Challa-Malladi, M., Fearnhead, H. O. & Bratton, S. B. The Apaf-1procaspase-9 apoptosome complex functions as a proteolytic-based molecular timer. *EMBO J.* **28**, 1916–1925 (2009).

90. Eckelman, B. P., Salvesen, G. S. & Scott, F. L. Human inhibitor of apoptosis proteins: Why XIAP is the black sheep of the family. *EMBO Rep.* **7**, 988–994 (2006).

91. Joza, N. *et al.* Essential role of the mitochondrial apoptosis-inducing factor in programmed cell death. *Nature* **410**, 549–554 (2001).

92. Li, L. Y., Luo, X. & Wang, X. Endonuclease G is an apoptotic DNase when released from mitochondria. *Nature* **412**, 95–99 (2001).

93. Sakahira, H., Enari, M. & Nagata, S. Cleavage of CAD inhibitor in CAD activation and DNA degradation during apoptosis. *Nature* **391**, 96–99 (1998).

94. Tait, S. W. G. & Green, D. R. Mitochondrial regulation of cell death. *Cold Spring Harb. Perspect. Biol.* **5**, a008706–a008706 (2013).

95. Tait, S. W. G. *et al.* Resistance to caspase-independent cell death requires persistence of intact mitochondria. *Dev. Cell* **18**, 802–813 (2010).

96. Ichim, G. *et al.* Limited Mitochondrial Permeabilization Causes DNA Damage and Genomic Instability in the Absence of Cell Death. *Mol. Cell* **57**, 860–872 (2015).

97. Singh, R., Letai, A. & Sarosiek, K. Regulation of apoptosis in health and disease: the balancing act of BCL-2 family proteins. *Nat. Rev. Mol. Cell Biol.* **20**, 175–193 (2019).

98. Dewson, G. *et al.* To Trigger Apoptosis, Bak Exposes Its BH3 Domain and Homodimerizes via BH3:Groove Interactions. *Mol. Cell* **30**, 369–380 (2008).

99. Korsmeyer, S. J. *et al.* Pro-apoptotic cascade activates BID, which oligomerizes BAK or BAX into pores that result in the release of cytochrome c. *Cell Death Differ.* **7**, 1166–1173 (2000).

100. Salvador-Gallego, R. *et al.* Bax assembly into rings and arcs in apoptotic mitochondria is linked to membrane pores. *EMBO J.* **35**, 389–401 (2016).

101. Muñoz-Pinedo, C. *et al.* Different mitochondrial intermembrane space proteins are released during apoptosis in a manner that is coordinately initiated but can vary in duration. *Proc. Natl. Acad. Sci. U. S. A.* **103**, 11573–11578 (2006).

102. Ke, F. F. S. *et al.* Embryogenesis and Adult Life in the Absence of Intrinsic Apoptosis Effectors BAX, BAK, and BOK. *Cell* **173**, 1217-1230.e17 (2018).

103. Llambi, F. *et al.* BOK Is a Non-canonical BCL-2 Family Effector of Apoptosis Regulated by ER-Associated Degradation. *Cell* **165**,

421–433 (2016).

104. Letai, A. *et al.* Distinct BH3 domains either sensitize or activate mitochondrial apoptosis, serving as prototype cancer therapeutics. *Cancer Cell* **2**, 183–192 (2002).

105. Sarosiek, K. A. *et al.* BID Preferentially Activates BAK while BIM Preferentially Activates BAX, Affecting Chemotherapy Response. *Mol. Cell* **51**, 751–765 (2013).

106. Dai, H., Pang, Y. P., Ramirez-Alvarado, M. & Kaufmann, S. H. Evaluation of the BH3-only protein Puma as a direct Bak activator. *J. Biol. Chem.* **289**, 89–99 (2014).

107. Gallenne, T. *et al.* Bax activation by the BH3-only protein Puma promotes cell dependence on antiapoptotic Bcl-2 family members. *J. Cell Biol.* **185**, 279–290 (2009).

108. Petros, A. M., Olejniczak, E. T. & Fesik, S. W. Structural biology of the Bcl-2 family of proteins. *Biochim. Biophys. Acta - Mol. Cell Res.* **1644**, 83–94 (2004).

109. Todt, F. *et al.* Differential retrotranslocation of mitochondrial Bax and Bak. *EMBO J.* **34**, 67–80 (2015).

110. Chen, H. C. *et al.* An interconnected hierarchical model of cell death regulation by the BCL-2 family. *Nat. Cell Biol.* **17**, 1270–1281 (2015).

111. Shamas-Din, A., Kale, J., Leber, B. & Andrews, D. W. Mechanisms of action of Bcl-2 family proteins. *Cold Spring Harb. Perspect. Biol.* **5**, 1–21 (2013).

112. Potter, D. S. & Letai, A. To prime, or not to prime: That is the question. *Cold Spring Harb. Symp. Quant. Biol.* **81**, 131–140 (2016).

113. Sarosiek, K. A. *et al.* Developmental Regulation of Mitochondrial Apoptosis by c-Myc Governs Age- and Tissue-Specific Sensitivity to Cancer Therapeutics. *Cancer Cell* **31**, 142–156 (2017).

114. Lakin, N. D. & Jackson, S. P. Regulation of p53 in response to DNA damage. *Oncogene* **18**, 7644–7655 (1999).

115. Zhang, L. N., Li, J. Y. & Xu, W. A review of the role of Puma, Noxa and Bim in the tumorigenesis, therapy and drug resistance of chronic lymphocytic leukemia. *Cancer Gene Ther.* **20**, 1–7 (2013).

116. Costa, D. B. *et al.* BIM mediates EGFR tyrosine kinase inhibitor-induced apoptosis in lung cancers with oncogenic EGFR mutations. *PLoS Med.* **4**, 1669–1680 (2007).

117. Hayakawa, J. *et al.* Inhibition of BAD phosphorylation either at serine 112 via extracellular signal-regulated protein kinase cascade or at serine 136 via Akt cascade sensitizes human ovarian cancer cells to cisplatin. *Cancer Res.* **60**, 5988–5994 (2000).

118. Crawford, E. D. & Wells, J. A. Caspase substrates and cellular remodeling. *Annu. Rev. Biochem.* **80**, 1055–1087 (2011).

119. Green, D. R. *Means to an end: apoptosis and other cell death mechanisms*. *Choice Reviews Online* **48**, (CSH Press, 2011).

120. Kivinen, K., Kallajoki, M. & Taimen, P. Caspase-3 is required in the apoptotic disintegration of the nuclear matrix. *Exp. Cell Res.* **311**, 62–73 (2005).

121. Sahara, S. *et al.* Acinus is a caspase-3-activated protein required for apoptotic chromatin condensation. *Nature* **401**, 168–173 (1999).

122. Levkau, B., Herren, B., Koyama, H., Ross, R. & Raines, E. W. Caspase-mediated cleavage of focal adhesion kinase pp125(FAK) and disassembly of focal adhesions in human endothelial cell apoptosis. *J. Exp. Med.* **187**, 579–586 (1998).

123. Communal, C. *et al.* Functional consequences of caspase activation in cardiac myocytes. *Proc. Natl. Acad. Sci. U. S. A.* **99**, 6252–6256 (2002).

124. Iwasaki, T., Katayama, T., Kohama, K., Endo, Y. & Sawasaki, T. Myosin

phosphatase is inactivated by caspase-3 cleavage and phosphorylation of myosin phosphatase targeting subunit 1 during apoptosis. *Mol. Biol. Cell* **24**, 748–756 (2013).

125. Vilas, G. L. *et al.* Posttranslational myristoylation of caspase-activated p21-activated protein kinase 2 (PAK2) potentiates late apoptotic events. *Proc. Natl. Acad. Sci. U. S. A.* **103**, 6542–6547 (2006).

126. Sebbagh, M. *et al.* Caspase-3-mediated cleavage of ROCK I induces MLC phosphorylation and apoptotic membrane blebbing. *Nat. Cell Biol.* **3**, 346–352 (2001).

127. Ricci, J. E. *et al.* Disruption of mitochondrial function during apoptosis is mediated by caspase cleavage of the p75 subunit of complex I of the electron transport chain. *Cell* **117**, 773–786 (2004).

128. Ravichandran, K. S. 'Recruitment signals' from apoptotic cells: Invitation to a quiet meal. *Cell* **113**, 817–820 (2003).

129. Segawa, K. *et al.* Caspase-mediated cleavage of phospholipid flippase for apoptotic phosphatidylserine exposure. *Science (80-. ).* **344**, 1164–1168 (2014).

130. Segawa, K., Kurata, S. & Nagata, S. Human type IV P-type ATPases that work as plasma membrane phospholipid flippases and their regulation by caspase and calcium. *J. Biol. Chem.* **291**, 762–772 (2016).

131. Suzuki, J., Imanishi, E. & Nagata, S. Xkr8 phospholipid scrambling complex in apoptotic phosphatidylserine exposure. *Proc. Natl. Acad. Sci. U. S. A.* **113**, 9509–9514 (2016).

132. Lamkanfi, M. & Kanneganti, T. D. Caspase-7: A protease involved in apoptosis and inflammation. *Int. J. Biochem. Cell Biol.* **42**, 21–24 (2010).

133. Cowling, V. & Downward, J. Caspase-6 is the direct activator of caspase-8 in the cytochrome c-induced apoptosis pathway: Absolute requirement for removal of caspase-6 prodomain. *Cell Death Differ.* **9**, 1046–1056 (2002).

134. Orth, K., Chinnaiyan, A. M., Garg, M., Froelich, C. J. & Dixit, V. M. The CED-3/ICE-like protease Mch2 is activated during apoptosis and cleaves the death substrate lamin A. *J. Biol. Chem.* **271**, 16443–16446 (1996).

135. Takahashi, A. *et al.* CrmA/SPI-2 inhibition of an endogenous ICE-related protease responsible for lamin a cleavage and apoptotic nuclear fragmentation. *J. Biol. Chem.* **271**, 32487–32490 (1996).

136. Galande, S., Dickinson, L. A., Mian, I. S., Sikorska, M. & Kohwi-Shigematsu, T. SATB1 Cleavage by Caspase 6 Disrupts PDZ Domain-Mediated Dimerization, Causing Detachment from Chromatin Early in T-Cell Apoptosis. *Mol. Cell. Biol.* **21**, 5591–5604 (2001).

137. Ruchaud, S. *et al.* Caspase-6 gene disruption reveals a requirement for lamin A cleavage in apoptotic chromatin condensation. *EMBO J.* **21**, 1967–1977 (2002).

138. Hanahan, D. & Weinberg, R. A. Hallmarks of cancer: The next generation. *Cell* **144**, 646–674 (2011).

139. Tsujimoto, Y. *et al.* Molecular cloning of the chromosomal breakpoint of B-Cell lymphomas and leukemias with the t(11;14) chromosome translocation. *Science (80-. ).* **224**, 1403–1406 (1984).

140. Hemann, M. T. & Lowe, S. W. The p53-Bcl-2 connection. *Cell Death Differ.* **13**, 1256–1259 (2006).

141. Eischen, C. M., Woo, D., Roussel, M. F. & Cleveland, J. L. Apoptosis Triggered by Myc-Induced Suppression of Bcl-X L or Bcl-2 Is Bypassed during Lymphomagenesis . *Mol. Cell. Biol.* **21**, 5063–5070 (2001).

142. Hata, A. N., Engelman, J. A. & Faber, A. C. The BCL2 family: Key mediators of the apoptotic response to targeted anticancer therapeutics. *Cancer*

*Discov.* **5**, 475–487 (2015).

143. Kapoor, I., Bodo, J., Hill, B. T., Hsi, E. D. & Almasan, A. Targeting BCL-2 in B-cell malignancies and overcoming therapeutic resistance. *Cell Death Dis.* **11**, 941 (2020).

144. Sartorius, U. A. & Krammer, P. H. Upregulation of Bcl-2 is involved in the mediation of chemotherapy resistance in human small cell lung cancer cell lines. *Int. J. Cancer* **97**, 584–592 (2002).

145. Tabuchi, Y. *et al.* Resistance to paclitaxel therapy is related with Bcl-2 expression through an estrogen receptor mediated pathway in breast cancer. *Int. J. Oncol.* **34**, 313–319 (2009).

146. Michels, J. *et al.* MCL-1 dependency of cisplatin-resistant cancer cells. *Biochem. Pharmacol.* **92**, 55–61 (2014).

147. Williams, J. *et al.* Expression of Bcl-xL in ovarian carcinoma is associated with chemoresistance and recurrent disease. *Gynecol. Oncol.* **96**, 287–295 (2005).

148. Rampino, N. *et al.* Somatic frameshift mutations in the BAX gene in colon cancers of the microsatellite mutator phenotype. *Science (80-. ).* **275**, 967–969 (1997).

149. Beroukhim, R. *et al.* The landscape of somatic copy-number alteration across human cancers. *Nature* **463**, 899–905 (2010).

150. Tagawa, H. *et al.* Genome-wide array-based CGH for mantle cell lymphoma: Identification of homozygous deletions of the proapoptotic gene BIM. *Oncogene* **24**, 1348–1358 (2005).

151. Cragg, M. S. *et al.* Treatment of B-RAF mutant human tumor cells with a MEK inhibitor requires Bim and is enhanced by a BH3 mimetic. *J. Clin. Invest.* **118**, 3651–3659 (2008).

152. Winter, P. S. *et al.* RAS signaling promotes resistance to JAK inhibitors by suppressing BAD-mediated apoptosis. *Sci. Signal.* **7**, (2014).

153. Faber, A. C. *et al.* mTOR inhibition specifically sensitizes colorectal cancers with KRAS or BRAF mutations to BCL-2/BCL-XL inhibition by suppressing MCL-1. *Cancer Discov.* **4**, 42–52 (2014).

154. Gregory, G. P. *et al.* CDK9 inhibition by dinaciclib potently suppresses Mcl-1 to induce durable apoptotic responses in aggressive MYC-driven B-cell lymphoma in vivo. *Leukemia* **29**, 1437–1441 (2015).

155. Vaillant, F. *et al.* Targeting BCL-2 with the BH3 Mimetic ABT-199 in Estrogen Receptor-Positive Breast Cancer. *Cancer Cell* **24**, 120–129 (2013).

156. Montero, J. & Haq, R. Adapted to Survive: Targeting Cancer Cells with BH3 Mimetics. *Cancer Discov.* **12**, 1217–1232 (2022).

157. Chin, J. W. & Schepartz, A. Design and evolution of a miniature Bcl-2 binding protein. *Angew. Chemie - Int. Ed.* **40**, 3806–3809 (2001).

158. Baell, J. B. & Huang, D. C. S. Prospects for targeting the Bcl-2 family of proteins to develop novel cytotoxic drugs. *Biochem. Pharmacol.* **64**, 851–863 (2002).

159. Townsend, P. A., Kozhevnikova, M. V., Cexus, O. N. F., Zamyatnin, A. A. & Soond, S. M. BH3-mimetics: recent developments in cancer therapy. *J. Exp. Clin. Cancer Res.* **40**, 355 (2021).

160. Rudin, C. M. *et al.* Phase II study of single-agent navitoclax (ABT-263) and biomarker correlates in patients with relapsed small cell lung cancer. *Clin. Cancer Res.* **18**, 3163–3169 (2012).

161. Balachander, S. B. *et al.* AZD4320, a dual inhibitor of bcl-2 and bcl-xl, induces tumor regression in hematologic cancer models without dose-limiting thrombocytopenia. *Clin. Cancer Res.* **26**, 6535–6549 (2020).

162. Roberts, A. W. *et al.* Targeting BCL2 with Venetoclax in Relapsed Chronic Lymphocytic Leukemia. *N. Engl. J. Med.* **374**, 311–322 (2016).

163. DiNardo, C. D. *et al.* Azacitidine and Venetoclax in Previously Untreated Acute Myeloid Leukemia. *N. Engl. J. Med.* **383**, 617–629 (2020).

164. Weeden, C. E. *et al.* Dual inhibition of BCL-XL and MCL-1 is required to induce tumour regression in lung squamous cell carcinomas sensitive to FGFR inhibition. *Oncogene* **37**, 4475–4488 (2018).

165. Seyfried, F. *et al.* Synergistic activity of combined inhibition of anti-apoptotic molecules in B-cell precursor ALL. *Leukemia* **36**, 901–912 (2022).

166. Faqar-Uz-Zaman, S. F., Heinicke, U., Meister, M. T., Vogler, M. & Fulda, S. BCL-xL-selective BH3 mimetic sensitizes rhabdomyosarcoma cells to chemotherapeutics by activation of the mitochondrial pathway of apoptosis. *Cancer Lett.* **412**, 131–142 (2018).

167. Sejic, N. *et al.* BCL-XL inhibition by BH3-mimetic drugs induces apoptosis in models of Epstein-Barr virus-associated T/NK-cell lymphoma. *Blood Adv.* **4**, 4775–4787 (2020).

168. Zhang, X. *et al.* Utilizing PROTAC technology to address the on-target platelet toxicity associated with inhibition of BCL-X. *Chem. Commun.* **55**, 14765–14768 (2019).

169. Reyna, D. E. *et al.* Direct Activation of BAX by BTSA1 Overcomes Apoptosis Resistance in Acute Myeloid Leukemia. *Cancer Cell* **32**, 490-505.e10 (2017).

170. Lopez, A. *et al.* Co-targeting of BAX and BCL-XL proteins broadly overcomes resistance to apoptosis in cancer. *Nat. Commun.* **13**, 1–18 (2022).

171. National Cancer Institute at the National Institutes of Health. NCI Dictionary of Cancer Terms. *National Cancer Institute* 3–5 (2021). Available at: https://www.cancer.gov/publications/dictionaries/cancer-terms/def/tumor.

172. Fisher, B. *et al.* Treatment of Primary Breast Cancer with Chemotherapy and Tamoxifen. *N. Engl. J. Med.* **305**, 1–6 (1981).

173. O'Brien, S. G. *et al.* Imatinib Compared with Interferon and Low-Dose Cytarabine for Newly Diagnosed Chronic-Phase Chronic Myeloid Leukemia. *N. Engl. J. Med.* **348**, 994–1004 (2003).

174. Mok, T. S. *et al.* Gefitinib or Carboplatin–Paclitaxel in Pulmonary Adenocarcinoma. *N. Engl. J. Med.* **361**, 947–957 (2009).

175. Bell, C. C. & Gilan, O. Principles and mechanisms of non-genetic resistance in cancer. *Br. J. Cancer* **122**, 465–472 (2020).

176. Flaherty, K. T. *et al.* Molecular landscape and actionable alterations in a genomically guided cancer clinical trial: National cancer institute molecular analysis for therapy choice (NCI-MATCH). *J. Clin. Oncol.* **38**, 3883–3894 (2020).

177. Le Tourneau, C. *et al.* Molecularly targeted therapy based on tumour molecular profiling versus conventional therapy for advanced cancer (SHIVA): A multicentre, open-label, proof-of-concept, randomised, controlled phase 2 trial. *Lancet Oncol.* **16**, 1324–1334 (2015).

178. Dienstmann, R., Jang, I. S., Bot, B., Friend, S. & Guinney, J. Database of genomic biomarkers for cancer drugs and clinical targetability in solid tumors. *Cancer Discov.* **5**, 118–123 (2015).

179. NCI-MATCH Sets 'Benchmark of Actionability'. *Cancer Discov.* **11**, 6–7 (2021).

180. Jorgensen, J. H. & Ferraro, M. J. Antimicrobial susceptibility testing: A review of general principles and contemporary practices. *Clin. Infect. Dis.* **49**, 1749–1755 (2009).

181. Meijer, T. G., Naipal, K. A., Jager, A. & Van Gent, D. C. Ex vivo tumor culture systems for functional drug testing and therapy response prediction. *Futur. Sci. OA* **3**, FSO190

(2017).

182. Sandberg, R. & Ernberg, I. The molecular portrait of in vitro growth by meta-analysis of gene-expression profiles. *Genome Biol.* **6**, R65 (2005).

183. Crystal, A. S. *et al.* Patient-derived models of acquired resistance can identify effective drug combinations for cancer. *Science (80-. ).* **346**, 1480–1486 (2014).

184. Van De Wetering, M. *et al.* Prospective derivation of a living organoid biobank of colorectal cancer patients. *Cell* **161**, 933–945 (2015).

185. Veninga, V. & Voest, E. E. Tumor organoids: Opportunities and challenges to guide precision medicine. *Cancer Cell* **39**, 1190–1201 (2021).

186. Woo, X. Y. *et al.* Conservation of copy number profiles during engraftment and passaging of patient-derived cancer xenografts. *Nat. Genet.* **53**, 86–99 (2021).

187. Byrne, A. T. *et al.* Interrogating open issues in cancer precision medicine with patient-derived xenografts. *Nat. Rev. Cancer* **17**, 254–268 (2017).

188. Stebbing, J. *et al.* Patient-derived xenografts for individualized care in advanced sarcoma. *Cancer* **120**, 2006–2015 (2014).

189. Guillen, K. P. *et al.* A human breast cancer-derived xenograft and organoid platform for drug discovery and precision oncology. *Nat. Cancer* **3**, 232–250 (2022).

190. Majumder, B. *et al.* Predicting clinical response to anticancer drugs using an ex vivo platform that captures tumour heterogeneity. *Nat. Commun.* **6**, 6169 (2015).

191. Klinghoffer, R. A. *et al.* A technology platform to assess multiple cancer agents simultaneously within a patient's tumor. *Sci. Transl. Med.* **7**, 284ra56 (2015).

192. Gundle, K. R. *et al.* Multiplexed Evaluation of Microdosed Antineoplastic Agents in Situ in the Tumor Microenvironment of Patients with Soft Tissue Sarcoma. *Clin. Cancer Res.* **26**, 3958–3968 (2020).

193. Jonas, O. *et al.* An implantable microdevice to perform high-throughput in vivo drug sensitivity testing in tumors. *Sci. Transl. Med.* **7**, 284ps10 (2015).

194. Tyner, J. W. *et al.* Kinase pathway dependence in primary human leukemias determined by rapid inhibitor screening. *Cancer Res.* **73**, 285–296 (2013).

195. Pemovska, T. *et al.* Individualized systems medicine strategy to tailor treatments for patients with chemorefractory acute myeloid leukemia. *Cancer Discov.* **3**, 1416–1429 (2013).

196. Malani, D. *et al.* Implementing a Functional Precision Medicine Tumor Board for Acute Myeloid Leukemia. *Cancer Discov.* **12**, 388–401 (2022).

197. Frismantas, V. *et al.* Ex vivo drug response profiling detects recurrent sensitivity patterns in drug-resistant acute lymphoblastic leukemia. *Blood* **129**, e26–e37 (2017).

198. Yu, M. *et al.* Ex vivo culture of circulating breast tumor cells for individualized testing of drug susceptibility. *Science (80-. ).* **345**, 216–220 (2014).

199. Lacayo, N. J. *et al.* Development and validation of a single-cell network profiling assay-based classifier to predict response to induction therapy in paediatric patients with de novo acute myeloid leukaemia: A report from the children's oncology group. *Br. J. Haematol.* **162**, 250–262 (2013).

200. Snijder, B. *et al.* Image-based ex-vivo drug screening for patients with aggressive haematological malignancies: interim results from a single-arm, open-label, pilot study. *Lancet Haematol.* **4**, e595–e606 (2017).

201. Kornauth, C. *et al.* Functional

Precision Medicine Provides Clinical Benefit in Advanced Aggressive Hematologic Cancers and Identifies Exceptional Responders. *Cancer Discov.* **12**, 372–387 (2022).

202. Chonghaile, T. N. *et al.* Pretreatment mitochondrial priming correlates with clinical response to cytotoxic chemotherapy. *Science (80-. ).* **334**, 1129–1133 (2011).

203. Vo, T. T. *et al.* Relative mitochondrial priming of myeloblasts and normal HSCs determines chemotherapeutic success in AML. *Cell* **151**, 344–355 (2012).

204. Davids, M. S. *et al.* Decreased mitochondrial apoptotic priming underlies stroma-mediated treatment resistance in chronic lymphocytic leukemia. *Blood* **120**, 3501–3509 (2012).

205. Goldsmith, K. C. *et al.* Mitochondrial Bcl-2 family dynamics define therapy response and resistance in neuroblastoma. *Cancer Res.* **72**, 2565–2577 (2012).

206. Brunelle, J. K., Ryan, J., Yecies, D., Opferman, J. T. & Letai, A. MCL-1-dependent leukemia cells are more sensitive to chemotherapy than BCL-2-dependent counterparts. *J. Cell Biol.* **187**, 429–442 (2009).

207. Deng, J. *et al.* BH3 Profiling Identifies Three Distinct Classes of Apoptotic Blocks to Predict Response to ABT-737 and Conventional Chemotherapeutic Agents. *Cancer Cell* **12**, 171–185 (2007).

208. Montero, J. *et al.* Drug-Induced death signaling strategy rapidly predicts cancer response to chemotherapy. *Cell* **160**, 977–989 (2015).

209. Brasó-Maristany, F. *et al.* PIM1 kinase regulates cell death, tumor growth and chemotherapy response in triple-negative breast cancer. *Nat. Med.* **22**, 1303–1313 (2016).

210. Pallis, M. *et al.* Complementary dynamic BH3 profiles predict co-operativity between the multi-kinase inhibitor TG02 and the BH3 mimetic ABT-199 in acute myeloid leukaemia cells. *Oncotarget* **8**, 16220–16232 (2017).

211. Montero, J. *et al.* Blastic plasmacytoid dendritic cell neoplasm is dependent on BCL2 and sensitive to venetoclax. *Cancer Discov.* **7**, 156–164 (2017).

212. Deng, J. *et al.* Bruton's tyrosine kinase inhibition increases BCL-2 dependence and enhances sensitivity to venetoclax in chronic lymphocytic leukemia. *Leukemia* **31**, 2075–2084 (2017).

213. Grundy, M. *et al.* Predicting effective pro-apoptotic anti-leukaemic drug combinations using cooperative dynamic BH3 profiling. *PLoS One* **13**, e0190682 (2018).

214. Grundy, M. *et al.* Early changes in rpS6 phosphorylation and BH3 profiling predict response to chemotherapy in AML cells. *PLoS One* **13**, e0196805 (2018).

215. Lee, J. S. *et al.* Statins enhance efficacy of venetoclax in blood cancers. *Sci. Transl. Med.* **10**, eaaq1240 (2018).

216. Garcia, J. S. *et al.* Dynamic BH3 Profiling Predicts for Clinical Response to Lenalidomide Plus Chemotherapy in Relapsed Acute Myeloid Leukemia. *Blood* **132**, 4058–4058 (2018).

217. de Jong, M. R. W. *et al.* Heterogeneous pattern of dependence on anti-apoptotic BCL-2 family proteins upon CHOP treatment in diffuse large b-cell lymphoma. *Int. J. Mol. Sci.* **20**, 6036 (2019).

218. Walsh, L. *et al.* BET Inhibition as a Rational Therapeutic Strategy for Invasive Lobular Breast Cancer. *Clin. Cancer Res.* **25**, 7139–7150 (2019).

219. Montero, J. *et al.* Destabilization of NOXA mRNA as a common resistance mechanism to targeted therapies. *Nat. Commun.* **10**, 5157 (2019).

220. Bhatt, S. *et al.* Reduced Mitochondrial Apoptotic Priming Drives Resistance

to BH3 Mimetics in Acute Myeloid Leukemia. *Cancer Cell* **38**, 872-890.e6 (2020).

221. Alcon, C. *et al.* Sequential combinations of chemotherapeutic agents with BH3 mimetics to treat rhabdomyosarcoma and avoid resistance. *Cell Death Dis.* **11**, 634 (2020).

222. Garcia, J. S. *et al.* Increased mitochondrial apoptotic priming with targeted therapy predicts clinical response to re-induction chemotherapy. *Am. J. Hematol.* **95**, 245–250 (2020).

223. Zoeller, J. J. *et al.* Navitoclax enhances the effectiveness of EGFR-targeted antibody-drug conjugates in PDX models of EGFR-expressing triple-negative breast cancer. *Breast Cancer Res.* **22**, 132 (2020).

224. Surman, D. R. *et al.* Therapeutic synergy in esophageal cancer and mesothelioma is predicted by dynamic BH3 profiling. *Mol. Cancer Ther.* **20**, 1469–1481 (2021).

225. Müller, D. *et al.* Functional apoptosis profiling identifies MCL-1 and BCL-xL as prognostic markers and therapeutic targets in advanced thymomas and thymic carcinomas. *BMC Med.* **19**, 300 (2021).

226. Alcon, C. *et al.* Er+ breast cancer strongly depends on mcl-1 and bcl-xl anti-apoptotic proteins. *Cells* **10**, (2021).

227. Karakas, B. *et al.* Mitochondrial estrogen receptors alter mitochondrial priming and response to endocrine therapy in breast cancer cells. *Cell Death Discov.* **7**, 189 (2021).

228. Rys, R. N. *et al.* Apoptotic blocks in primary non-hodgkin b cell lymphomas identified by bh3 profiling. *Cancers (Basel).* **13**, 1–22 (2021).

229. Montinaro, A. *et al.* Potent pro-apoptotic combination therapy is highly effective in a broad range of cancers. *Cell Death Differ.* **29**, 492–503 (2022).

230. Bhola, P. D. *et al.* High-throughput dynamic BH3 profiling may quickly and accurately predict effective therapies in solid tumors. *Sci. Signal.* **13**, (2020).

231. Potter, D. S., Du, R., Bhola, P., Bueno, R. & Letai, A. Dynamic BH3 profiling identifies active BH3 mimetic combinations in non-small cell lung cancer. *Cell Death Dis.* **12**, 741 (2021).

232. Daniels, V. W. *et al.* Metabolic perturbations sensitize triple-negative breast cancers to apoptosis induced by BH3 mimetics. *Sci. Signal.* **14**, (2021).

233. Bragheri, F., Vázquez, R. M. & Osellame, R. Microfluidics. in *Three-Dimensional Microfabrication Using Two-Photon Polymerization* 493–526 (Elsevier, 2019). doi:10.1016/B978-0-12-817827-0.00057-6

234. Halldorsson, S., Lucumi, E., Gómez-Sjöberg, R. & Fleming, R. M. T. Advantages and challenges of microfluidic cell culture in polydimethylsiloxane devices. *Biosens. Bioelectron.* **63**, 218–231 (2015).

235. Castiaux, A. D., Spence, D. M. & Martin, R. S. Review of 3D cell culture with analysis in microfluidic systems. *Anal. Methods* **11**, 4220–4232 (2019).

236. Duzagac, F., Saorin, G., Memeo, L., Canzonieri, V. & Rizzolio, F. Microfluidic organoids-on-a-chip: Quantum leap in cancer research. *Cancers (Basel).* **13**, 1–35 (2021).

237. Lim, J., Ching, H., Yoon, J. K., Jeon, N. L. & Kim, Y. T. Microvascularized tumor organoids-on-chips: advancing preclinical drug screening with pathophysiological relevance. *Nano Converg.* **8**, 12 (2021).

238. Yuki, K., Cheng, N., Nakano, M. & Kuo, C. J. Organoid Models of Tumor Immunology. *Trends Immunol.* **41**, 652–664 (2020).

239. Montanez-Sauri, S. I., Sung, K. E., Berthier, E. & Beebe, D. J. Enabling screening in 3D microenvironments:

Probing matrix and stromal effects on the morphology and proliferation of T47D breast carcinoma cells. *Integr. Biol. (United Kingdom)* **5**, 631–640 (2013).

240. Hassell, B. A. *et al.* Human Organ Chip Models Recapitulate Orthotopic Lung Cancer Growth, Therapeutic Responses, and Tumor Dormancy In Vitro. *Cell Rep.* **21**, 508–516 (2017).

241. Miller, C. P., Tsuchida, C., Zheng, Y., Himmelfarb, J. & Akilesh, S. A 3D Human Renal Cell Carcinoma-on-a-Chip for the Study of Tumor Angiogenesis. *Neoplasia (United States)* **20**, 610–620 (2018).

242. Lee, J. H. *et al.* Microfluidic co-culture of pancreatic tumor spheroids with stellate cells as a novel 3D model for investigation of stroma-mediated cell motility and drug resistance. *J. Exp. Clin. Cancer Res.* **37**, 4 (2018).

243. Rizvi, I. *et al.* Flow induces epithelial-mesenchymal transition, cellular heterogeneity and biomarker modulation in 3D ovarian cancer nodules. *Proc. Natl. Acad. Sci. U. S. A.* **110**, (2013).

244. Erdogan, B. *et al.* Cancer-associated fibroblasts promote directional cancer cell migration by aligning fibronectin. *J. Cell Biol.* **216**, 3799–3816 (2017).

245. Li, R. *et al.* Macrophage-secreted TNFα and TGFβ1 influence migration speed and persistence of cancer cells in 3D tissue culture via independent pathways. *Cancer Res.* **77**, 279–290 (2017).

246. Tang, Y. *et al.* A Biomimetic Microfluidic Tumor Microenvironment Platform Mimicking the EPR Effect for Rapid Screening of Drug Delivery Systems. *Sci. Rep.* **7**, 1–14 (2017).

247. Chen, M. B., Lamar, J. M., Li, R., Hynes, R. O. & Kamm, R. D. Elucidation of the roles of tumor integrin β1 in the extravasation stage of the metastasis cascade. *Cancer Res.* **76**, 2513–2524 (2016).

248. Nagrath, S. *et al.* Isolation of rare circulating tumour cells in cancer patients by microchip technology. *Nature* **450**, 1235–1239 (2007).

249. Stott, S. L. *et al.* Isolation of circulating tumor cells using a microvortex-generating herringbone-chip. *Proc. Natl. Acad. Sci. U. S. A.* **107**, 18392–18397 (2010).

250. Ribeiro-Samy, S. *et al.* Fast and efficient microfluidic cell filter for isolation of circulating tumor cells from unprocessed whole blood of colorectal cancer patients. *Sci. Rep.* **9**, 1–12 (2019).

251. Au, S. H. *et al.* Microfluidic isolation of circulating tumor cell clusters by size and asymmetry. *Sci. Rep.* **7**, 1–10 (2017).

252. Choi, H. *et al.* A label-free DC impedance-based microcytometer for circulating rare cancer cell counting. *Lab Chip* **13**, 970–977 (2013).

253. Mani, G. K. *et al.* ZnO-Based Microfluidic pH Sensor: A Versatile Approach for Quick Recognition of Circulating Tumor Cells in Blood. *ACS Appl. Mater. Interfaces* **9**, 5193–5203 (2017).

254. Yang, F., Liao, X., Tian, Y. & Li, G. Exosome separation using microfluidic systems: size-based, immunoaffinity-based and dynamic methodologies. *Biotechnol. J.* **12**, (2017).

255. Balakrishnan, S. G., Ahmad, M. R., Koloor, S. S. R. & Petrů, M. Separation of ctDNA by superparamagnetic bead particles in microfluidic platform for early cancer detection. *J. Adv. Res.* **33**, 109–116 (2021).

256. Lee, H., Park, C., Na, W., Park, K. H. & Shin, S. Precision cell-free DNA extraction for liquid biopsy by integrated microfluidics. *npj Precis. Oncol.* **4**, 1–10 (2020).

257. Xu, Z. *et al.* Application of a microfluidic chip-based 3D co-culture to test drug sensitivity for individualized treatment of lung cancer. *Biomaterials* **34**, 4109–4117 (2013).

258. Ying, L. *et al.* Cancer associated fibroblast-derived hepatocyte growth factor inhibits the paclitaxel-induced apoptosis of lung cancer A549 cells by up-regulating the PI3K/Akt and GRP78 signaling on a microfluidic platform. *PLoS One* **10**, (2015).

259. Terrell-Hall, T. B., Nounou, M. I., El-Amrawy, F., Griffith, J. I. G. & Lockman, P. R. Trastuzumab distribution in an in-vivo and in-vitro model of brain metastases of breast cancer. *Oncotarget* **8**, 83734–83744 (2017).

260. Bai, J., Tu, T. Y., Kim, C., Thiery, J. P. & Kamm, R. D. Identification of drugs as single agents or in combination to prevent carcinoma dissemination in a microfluidic 3D environment. *Oncotarget* **6**, 36603–36614 (2015).

261. Pavesi, A. *et al.* A 3D microfluidic model for preclinical evaluation of TCR-engineered T cells against solid tumors. *JCI Insight* **2**, (2017).

262. Kim, C., Bang, J. H., Kim, Y. E., Lee, S. H. & Kang, J. Y. On-chip anticancer drug test of regular tumor spheroids formed in microwells by a distributive microchannel network. *Lab Chip* **12**, 4135–4142 (2012).

263. Khot, M. I. *et al.* Characterising a PDMS based 3D cell culturing microfluidic platform for screening chemotherapeutic drug cytotoxic activity. *Sci. Rep.* **10**, 1–13 (2020).

264. Ruppen, J. *et al.* Towards personalized medicine: Chemosensitivity assays of patient lung cancer cell spheroids in a perfused microfluidic platform. *Lab Chip* **15**, 3076–3085 (2015).

265. Lim, W. *et al.* Formation of size-controllable tumour spheroids using a microfluidic pillar array (μFPA) device. *Analyst* **143**, 5841–5848 (2018).

266. Lee, J. M. *et al.* Generation of tumor spheroids using a droplet-based microfluidic device for photothermal therapy. *Microsystems Nanoeng.* **6**, 1–10 (2020).

267. Horowitz, L. F. *et al.* Microdissected ‘cuboids’ for microfluidic drug testing of intact tissues. *Lab Chip* **21**, 122–142 (2021).

268. Astolfi, M. *et al.* Micro-dissected tumor tissues on chip: An ex vivo method for drug testing and personalized therapy. *Lab Chip* **16**, 312–325 (2016).

269. Chakrabarty, S. *et al.* A Microfluidic Cancer-on-Chip Platform Predicts Drug Response Using Organotypic Tumor Slice Culture. *Cancer Res.* **82**, 510–520 (2022).

270. Rodriguez, A. D. *et al.* A microfluidic platform for functional testing of cancer drugs on intact tumor slices. *Lab Chip* **20**, 1658–1675 (2020).

271. Horowitz, L. F. *et al.* Multiplexed drug testing of tumor slices using a microfluidic platform. *npj Precis. Oncol.* **4**, 12 (2020).

272. Lee, D. W. *et al.* High-throughput screening (HTS) of anticancer drug efficacy on a micropillar/microwell chip platform. *Anal. Chem.* **86**, 535–542 (2014).

273. Wong, A. H. H. *et al.* Drug screening of cancer cell lines and human primary tumors using droplet microfluidics. *Sci. Rep.* **7**, 9109 (2017).

274. Popova, A. A. *et al.* Miniaturized Drug Sensitivity and Resistance Test on Patient-Derived Cells Using Droplet-Microarray. *SLAS Technol.* **26**, 274–286 (2021).

275. Eduati, F. *et al.* A microfluidics platform for combinatorial drug screening on cancer biopsies. *Nat. Commun.* **9**, 2434 (2018).

276. Burg, T. P. *et al.* Weighing of biomolecules, single cells and single nanoparticles in fluid. *Nature* **446**, 1066–1069 (2007).

277. Cermak, N. *et al.* High-throughput measurement of single-cell growth rates using serial microfluidic mass sensor arrays. *Nat. Biotechnol.* **34**, 1052–1059 (2016).

278. Stevens, M. M. *et al.* Drug sensitivity of single cancer cells is predicted by changes in mass accumulation rate. *Nat. Biotechnol.* **34**, 1161–1167 (2016).

279. Cetin, A. E. *et al.* Determining therapeutic susceptibility in multiple myeloma by single-cell mass accumulation. *Nat. Commun.* **8**, (2017).

280. Stockslager, M. A. *et al.* Functional drug susceptibility testing using single-cell mass predicts treatment outcome in patient-derived cancer neurosphere models. *Cell Rep.* **37**, 109788 (2021).

281. Ryan, J., Montero, J., Rocco, J. & Letai, A. IBH3: Simple, fixable BH3 profiling to determine apoptotic priming in primary tissue by flow cytometry. *Biol. Chem.* **397**, 671–678 (2016).

282. Seyfried, F. *et al.* Prediction of venetoclax activity in precursor B-ALL by functional assessment of apoptosis signaling. *Cell Death Dis.* **10**, 571 (2019).

283. Wang, X., Liu, Z. & Pang, Y. Concentration gradient generation methods based on microfluidic systems. *RSC Adv.* **7**, 29966–29984 (2017).

284. Satti, J. The Emerging Low-dose Therapy for Advanced Cancers. *Dose-Response* **7**, dose-response.0 (2009).

285. Foucquier, J. & Guedj, M. Analysis of drug combinations: current methodological landscape. *Pharmacol. Res. Perspect.* **3**, e00149 (2015).

286. Jerchel, I. S. *et al.* RAS pathway mutations as a predictive biomarker for treatment adaptation in pediatric B-cell precursor acute lymphoblastic leukemia. *Leukemia* **32**, 931–940 (2018).

287. Brown, P. *et al.* FLT3 inhibition selectively kills childhood acute lymphoblastic leukemia cells with high levels of FLT3 expression. *Blood* **105**, 812–820 (2005).

288. Ding, Y. Y. *et al.* Clinical efficacy of ruxolitinib and chemotherapy in a child with philadelphia chromosome-like acute lymphoblastic leukemia with GOLGA5-JAK2 fusion and induction failure. *Haematologica* **103**, e427–e431 (2018).

289. Kim, E. *et al.* Ibrutinib inhibits pre-BCR+ B-cell acute lymphoblastic leukemia progression by targeting BTK and BLK. *Blood* **129**, 1155–1165 (2017).

290. Joshi, M., Rice, S. J., Liu, X., Miller, B. & Belani, C. P. Trametinib with or without Vemurafenib in braf mutated non-small cell lung cancer. *PLoS One* **10**, e0118210 (2015).

291. Fofaria, N. M., Frederick, D. T., Sullivan, R. J., Flaherty, K. T. & Srivastava, S. K. Overexpression of Mcl-1 confers resistance to BRAFV600E inhibitors alone and in combination with MEK1/2 inhibitors in melanoma. *Oncotarget* **6**, 40535–40556 (2015).

292. Tada, M. *et al.* MCL1 inhibition enhances the therapeutic effect of MEK inhibitors in KRAS-mutant lung adenocarcinoma cells. *Lung Cancer* **133**, 88–95 (2019).

293. O'Reilly, L. A. *et al.* MEK/ERK-Mediated Phosphorylation of Bim Is Required to Ensure Survival of T and B Lymphocytes during Mitogenic Stimulation. *J. Immunol.* **183**, 261–269 (2009).

294. Li, Z., He, S. & Look, A. T. The MCL1-specific inhibitor S63845 acts synergistically with venetoclax/ABT-199 to induce apoptosis in T-cell acute lymphoblastic leukemia cells. *Leukemia* **33**, 262–266 (2019).

295. Chahal, M. *et al.* MGMT modulates glioblastoma angiogenesis and response to the tyrosine kinase inhibitor sunitinib. *Neuro. Oncol.* **12**, 822–833 (2010).

296. Fenton, M. S. *et al.* Sunitinib inhibits MEK/ERK and SAPK/JNK pathways and increases sodium/iodide

symporter expression in papillary thyroid cancer. *Thyroid* **20**, 965–974 (2010).

297. Robak, P. & Robak, T. Bortezomib for the Treatment of Hematologic Malignancies: 15 Years Later. *Drugs R D* **19**, 73–92 (2019).

298. Taguchi, T. *et al.* Conventional and molecular cytogenetic characterization of a new human cell line, GIST-T1, established from gastrointestinal stromal tumor. *Lab. Investig.* **82**, 663–665 (2002).

299. Gupta, A., Ma, S., Che, K., Pobbati, A. V. & Rubin, B. P. Inhibition of PI3K and MAPK pathways along with KIT inhibitors as a strategy to overcome drug resistance in gastrointestinal stromal tumors. *PLoS One* **16**, e0252689 (2021).

300. Inaba, H. & Mullighan, C. G. Pediatric acute lymphoblastic leukemia. *Haematologica* **105**, 2524–2539 (2020).

301. Letai, A., Bhola, P. & Welm, A. L. Functional precision oncology: Testing tumors with drugs to identify vulnerabilities and novel combinations. *Cancer Cell* **40**, 26–35 (2022).

302. Kuhlen, M., Klusmann, J. H. & Hoell, J. I. Molecular Approaches to Treating Pediatric Leukemias. *Front. Pediatr.* **7**, (2019).

303. Gröbner, S. N. *et al.* The landscape of genomic alterations across childhood cancers. *Nature* **555**, 321–327 (2018).

304. Ginsburg, G. S. & Phillips, K. A. Precision medicine: From science to value. *Health Aff.* **37**, 694–701 (2018).

305. Irving, J. *et al.* Ras pathway mutations are prevalent in relapsed childhood acute lymphoblastic leukemia and confer sensitivity to MEK inhibition. *Blood* **124**, 3420–3430 (2014).

306. Ikezoe, T. *et al.* The antitumor effects of sunitinib (formerly SU11248) against a variety of human hematologic malignancies: Enhancement of growth inhibition via inhibition of mammalian target of rapamcycin signaling. *Mol. Cancer Ther.* **5**, 2522–2530 (2006).

307. Gu, T. lei *et al.* Survey of activated FLT3 signaling in leukemia. *PLoS One* **6**, e19169 (2011).

308. Valentin, R., Grabow, S. & Davids, M. S. The rise of apoptosis: Targeting apoptosis in hematologic malignancies. *Blood* **132**, 1248–1264 (2018).

309. Montero, J. & Letai, A. Why do BCL-2 inhibitorswork and where should we use them in the clinic? *Cell Death Differ.* **25**, 56–64 (2018).

310. Oudenaarden, C. R. L., van de Ven, R. A. H. & Derksen, P. W. B. Re-inforcing the cell death army in the fight against breast cancer. *J. Cell Sci.* **131**, jcs212563 (2018).

311. Savona, M. R. & Wei, A. H. Incorporating precision BH3 warheads into the offensive against acute myeloid leukemia. *J. Clin. Oncol.* **37**, 1785–1789 (2019).

312. Lin, V. S., Xu, Z. F., Huang, D. C. S. & Thijssen, R. Bh3 mimetics for the treatment of b-cell malignancies—insights and lessons from the clinic. *Cancers (Basel).* **12**, 1–24 (2020).

313. Klener, P., Sovilj, D., Renesova, N. & Andera, L. Bh3 mimetics in hematologic malignancies. *Int. J. Mol. Sci.* **22**, (2021).

314. Maji, S. *et al.* Bcl-2 Antiapoptotic Family Proteins and Chemoresistance in Cancer. in *Advances in Cancer Research* **137**, 37–75 (2018).

315. Mansoori, B., Mohammadi, A., Davudian, S., Shirjang, S. & Baradaran, B. The different mechanisms of cancer drug resistance: A brief review. *Adv. Pharm. Bull.* **7**, 339–348 (2017).

316. Diepstraten, S. T. *et al.* The manipulation of apoptosis for cancer therapy using BH3-mimetic drugs. *Nat. Rev. Cancer* **22**, 45–64 (2022).

317. Manzano-Muñoz, A. *et al.* MCL-1

Inhibition Overcomes Anti-apoptotic Adaptation to Targeted Therapies in B-Cell Precursor Acute Lymphoblastic Leukemia. *Front. Cell Dev. Biol.* **9**, (2021).

318. Simsek, C., Esin, E. & Yalcin, S. Metronomic Chemotherapy: A Systematic Review of the Literature and Clinical Experience. *J. Oncol.* **2019**, (2019).

319. Korfi, K. *et al.* BIM mediates synergistic killing of B-cell acute lymphoblastic leukemia cells by BCL-2 and MEK inhibitors. *Cell Death Dis.* **7**, e2177–e2177 (2016).

320. Tan, N. *et al.* Bcl-2/Bcl-xL inhibition increases the efficacy of MEK inhibition alone and in combination with PI3 kinase inhibition in lung and pancreatic tumor models. *Mol. Cancer Ther.* **12**, 853–864 (2013).

321. Elgendy, M. *et al.* Dual modulation of MCL-1 and mTOR determines the response to sunitinib. *J. Clin. Invest.* **127**, 153–168 (2017).

322. Sale, M. J. *et al.* Targeting melanoma's MCL1 bias unleashes the apoptotic potential of BRAF and ERK1/2 pathway inhibitors. *Nat. Commun.* **10**, 1–19 (2019).

323. Xin, H. *et al.* Sunitinib inhibition of Stat3 induces renal cell carcinoma tumor cell apoptosis and reduces immunosuppressive cells. *Cancer Res.* **69**, 2506–2513 (2009).

324. Yang, F. *et al.* Sunitinib induces apoptosis and growth arrest of medulloblastoma tumor cells by inhibiting STAT3 and AKT signaling pathways. *Mol. Cancer Res.* **8**, 35–45 (2010).

325. Osada, N. *et al.* mTOR inhibitors sensitize multiple myeloma cells to venetoclax via IKZF3- And Blimp-1-mediated BCL-2 upregulation. *Haematologica* **106**, 3008–3013 (2021).

326. Konopleva, M. & Letai, A. BCL-2 inhibition in AML: An unexpected bonus? *Blood* **132**, 1007–1012 (2018).

327. Trinh, K. T. L., Thai, D. A., Chae, W. R. & Lee, N. Y. Rapid Fabrication of Poly(methyl methacrylate) Devices for Lab-ona-Chip Applications Using Acetic Acid and UV Treatment. *ACS Omega* **5**, 17396–17404 (2020).

328. Matellan, C. & Del Río Hernández, A. E. Cost-effective rapid prototyping and assembly of poly(methyl methacrylate) microfluidic devices. *Sci. Rep.* **8**, 1–13 (2018).

329. Sözmen, A. B. & Arslan Yildiz, A. Cost-effective and rapid prototyping of PMMA microfluidic device via polymer-assisted bonding. *Microfluid. Nanofluidics* **25**, 1–11 (2021).

Tesi doctoral

# Advancing cancer precision medicine through cell-based functional assays and microfluidics

Finding the needle in a haystack to improve pediàtric leukemia treatment

Albert Manzano Muñoz

Dirigit per Joan Montero Boronat


UNIVERSITAT DE BARCELONA